

Development and Dynamics of Microfabricated Enzymatic Biosensors

Thesis by
Dvin Adalian

In Partial Fulfillment of the Requirements for
the degree of
Doctor of Philosophy

The logo for the California Institute of Technology (Caltech), featuring the word "Caltech" in a bold, orange, sans-serif font.

CALIFORNIA INSTITUTE OF TECHNOLOGY
Pasadena, California

2019
(Defended June 5, 2019)

© 2019

Dvin Adalian

All Rights Reserved

To the memory of Professor Tom Tombrello,
whose passion is sorely missed.

Acknowledgements

I would like to first and foremost acknowledge and thank my parents, my brother, and the rest of the extended clan. I would be nowhere without your support.

This work would not at all have been possible without a dedicated team driving its many components and pursuing these dreams of a better world. Samson Chen, Musab Jilani, Steven Li, Xio Madero, Richard Smith, Abhinav Agarwal, Christin Ahlbrecht, and Juan Cardenas, I will remain indebted to you all.

Thank you to fellow researchers who have made my time at the Institute enjoyable and productive: Max Jones, Lucia De Rose, Kelly Mauser, Ari Weinstein, Brett Babin, Vanessa Heckman, and those whose wisdom I have benefitted from: Muhammad Mujeeb-U-Rahman, and Sameer Walavalkar, you have my gratitude. The research itself could not have happened without the amazing Kavli Nanoscience Institute on campus and its staff, so Guy DeRose, Alex Wertheim, Nathan Lee, Bert Mendoza, Melissa Melendes, and Matt Hunt, thank you for your numerous efforts as well.

It has taken the time of many professors and advisors to reach the end (almost) of this effort. Many thanks to Prof. Arti Gaur for her research support, Prof. Chiara Daraio and Prof. Rob Phillips for their committee service, and Prof. Azita Emami and Dr. Pete Petillo for both. And of course Professor Scherer, thank you for your belief in me and the opportunities you have provided.

And lastly I would like to give thanks to friends that have kept me sane through this process: Anton, Sean, Stephen, Lily, Loren, Zac, Ronan, Áine, Yvonne, and Georg, you will surely see more of me soon, and for the ones I see at home, Kee, Jamie, Pallavi, Bergen, Erik, Travis, and Elana, you have been the most invaluable support base one could have.

Abstract

This work focuses on extending the use of microfabrication techniques to all parts of enzymatic sensors, evaluating their performance, and understanding the behavior of the resulting devices. These results may enable novel sensor construction approaches and integration of enzymatic functionalization with CMOS wafer-scale fabrication. We apply these approaches to glucose oxidase enzyme layers and evaluate novel amperometric enzymatic glucose sensor designs. Improved enzyme immobilization techniques using spin coating and vapor stabilization are implemented on platinum electrodes built on silicon wafer substrates as well as on wireless CMOS potentiostats. Enzyme layers were patterned via photolithography and subsequently sputter coated with porous platinum which may act as a protective diffusion barrier and serves as a microfabricated reaction cavity with high product capture efficiency. Functional biosensor K_M and sensitivities were observed with multi-month lifetimes demonstrating tolerance of enzymatic layers to semiconductor microfabrication processes. We observed consistently reproducible and uniform sensor performance between devices on single substrates and between substrates, suggesting that enzyme chemistry is compatible with the precision of mass parallel CMOS fabrication, enabling low cost sensor fabrication and functionalization. Mathematical descriptions and simulations of such sensors were developed and are presented, providing insight into the electrochemical and biochemical dynamics. Microfabricated CMOS-scale sensors enable the development of low tissue-impact biosensors for in vivo implant purposes for many chronic diseases requiring continual analyte measurements, such as for glucose monitoring in diabetes management. This thesis describes the fabrication processes, modelling of the device behavior, and analysis of in vitro performance data.

Table of Contents

Acknowledgements	iv
Abstract.....	v
Table of Contents	vi
List of Figures	viii
List of Tables.....	x
Nomenclature	xi
Chapter 1 Introduction, Background, and Motivation.....	1
1.1 Biosensing Technology:	1
1.2 Biomedical Needs	2
1.3 Amperometric Enzyme Biosensors	3
1.4 Existing Technologies.....	6
1.5 Continuous Glucose Monitoring	7
1.6 Sensor Performance Criteria	8
1.7 Potentiostatic Sensors	9
1.8 Microfabrication	11
1.9 Wireless Implants.....	12
1.10 Goals	12
Chapter 2 Discussion on Device Electrochemistry	17
2.1 Redox Reaction Expectations	17
2.2 Electrode Behavior	19
2.3 Implemented Electrodes	21
Chapter 3 Sensor Chemical Environment and Reactions	30
3.1 Enzymatics.....	30
3.2 Analyte Ranges:.....	35
3.3 Tissue Response Concerns	37
3.4 Sensor Fouling and Immobilizations.....	38
3.5 Sensor Coatings	39
3.6 Interference Concerns	40
Chapter 4 Modeling Sensor Behavior.....	45
Chapter 5 Wafer Spincoated GOx Sensors.....	56
5.1 Overview	56
5.2 Platinum Fabrication	56
5.3 Considerations for Seeking Spincoating:	62
5.4. Reagents and Materials.....	65
5.5. Instrumentation.....	65
5.6. Experimental Methods.....	66
5.7. Characterization.....	70
5.8. Concluding Observations.....	76

Chapter 6 Sputtered Layers on Immobilized Enzyme	79
6.1 Overview:	79
6.2. Considerations for Barrier Layers:	79
6.3. Reagents and Materials.....	82
6.4. Instrumentation.....	82
6.5. Experimental Methods.....	82
6.6. Characterization.....	85
6.7 Discussion	91
6.8 Concluding Observations.....	94
Chapter 7 CMOS Sensor Fabrication.....	97
7.1 Overview	97
7.2 CMOS Design.....	98
7.3 Electrode Fabrication	99
7.4 In Vitro Evaluation	107
7.5 In Vivo Considerations and Future Work.....	110
Chapter 8 Concluding Remarks.....	113
Appendix A: Fabrication Recipes	116

List of Figures

Figure 1.1 Schematic of a three-electrode potentiostat system	10
Figure 1.2 Example microfabricated 3-electrode set.	11
Figure 2.1 Platinum CV in deoxygenated PBS.	22
Figure 2.2 CV of platinum electrodes in PBS.	23
Figure 2.3 Visualization of voltage behavior of three platinum electrode system. ...	26
Figure 2.4 H ₂ O ₂ oxidation current vs. concentration on Pt electrodes.	27
Figure 4.1 1D simulation cell schematic.	47
Figure 4.2 Current response to enzyme layer thickness.	49
Figure 4.3 [G] vs. layer thickness.	50
Figure 4.4 [H ₂ O ₂] vs. layer thickness.	51
Figure 4.5 [O ₂] vs. layer thickness.	52
Figure 4.6 Current produced per mole of H ₂ O ₂ generated in film.	53
Figure 5.1 AFM of electrode surfaces	58
Figure 5.2 TEM diffraction patterns of.....	59
Figure 5.3 Pt-coated silicon dioxide nanopillars	60
Figure 5.4 Reference electrode built with Ag/AgCl.....	61
Figure 5.5 SEM image of Ag/AgCl electrode surface.	61
Figure 5.6 Three-electrode platinum GOx-coated sensor.	67
Figure 5.7 Spincoat wafer fabrication sequence.....	68
Figure 5.8 Wafer measurement station.....	69
Figure 5.9 100mm wafer electrode layout.	70
Figure 5.10 Surface profilometry of the enzyme spincoat post liftoff.	71
Figure 5.11 Current-concentration data from 7 electrodes.....	72
Figure 5.12 Sensor stabilization comparison.	72
Figure 5.13 Sensitivity and exponential knee over 35 days	74
Figure 5.14 I _{max} and K _M over 35 days.....	75
Figure 5.15 Settling times for dropcoat-type and spincoat-type wafers.....	76
Figure 6.1 Visualization of signal linearity control	81
Figure 6.2 Sputter coated sensor fabrication sequence.....	84
Figure 6.3 Electrode coating comparisons.....	85
Figure 6.4 Comparison of sensor fabrication methods.....	86
Figure 6.5 200nm platinum coated and uncoated sensors, wide range	88
Figure 6.6 200nm platinum coated and uncoated sensors, narrow range	89
Figure 6.7 Example data for single electrode over 3 months	90
Figure 6.8 Sensitivity and exponential knee over 95 days.....	90
Figure 6.9 I _{max} and K _M over 95 days	91
Figure 6.10 SEM images of a platinum sputter coat on top of an enzyme layer.	94
Figure 7.1 CMOS wafer containing approximately 120 dies.	97
Figure 7.2 Individual CMOS potentiostat device.	99
Figure 7.3 CMOS device post-processing recipe summary.	101

Figure 7.4 Cross-section view of aluminum bond pad.....	102
Figure 7.5 A cross-section FIB cut of 1 of the 3 aluminum pads.	103
Figure 7.6 Cross-section FIB cut after etching with Aluminum Etch Type A.....	104
Figure 7.7 Completed CMOS device with Pt electrodes and GOx layer.....	105
Figure 7.8 Cross-section diagram of the bond pad structure.....	106
Figure 7.9 CMOS contact pad chemically etched down to passivation structures.	107
Figure 7.10 CMOS glucose measurement with K_M fit curves.	108
Figure 7.11 Examination of tissue response.....	111

List of Tables

Table 1.1 Enzymatic glucose sensor generations.....	5
Table 4.1 Summary of COMSOL diffusion and enzyme simulation parameters....	54
Table 7.1 CMOS in vitro measurement parameters.....	109
Table 7.2 Spincoat wafer to CMOS device comparison.....	110

Nomenclature

CA. Cellulose Acetate.

CE. Counter Electrode.

BSA. Bovine Serum Albumin.

CGM. Continuous Glucose Monitor.

CMOS. Complementary Metal–Oxide–Semiconductor integrated circuit construction technology.

CV. Cyclic Voltammetry.

FBR/FBC. Foreign Body Response/Capsule.

G. Glucose.

GA. Glutaraldehyde.

FAD. Flavin Adenine Dinucleotide.

FIB. Focused Ion Beam.

GOx. Glucose Oxidase.

ISF. Interstitial Fluid.

LoD. Limit of Detection.

M-M. Michaelis–Menten kinetics.

PBS. Phosphate Buffered Saline.

PC. Polycarbonate.

PECVD. Plasma-enhanced chemical vapor deposition

RE. Reference Electrode.

WE. Working Electrode.

Chapter 1 Introduction, Background, and Motivation

1.1 Biosensing Technology:

With the advent of both physical understanding and physical engineering of electrical systems, over a century ago now, came the opportunity to interface biological systems as an environment with which to interact and to measure in new ways. In the past decades since Leland Clark's [1] pivotal ambient oxygen sensor, the field of biosensing has expanded to many analytes and into many different measurement strategies, with designs for both environmental and medical applications. Modern biosensors exist today in both clinical and residential settings due to their high level of functionality and manufacturability.

Biosensors are traditionally defined as “a self-contained analytical device that combines a biological component with a physicochemical device for the detection of an analyte of biological importance [2].” As such, the two fundamental aspects of all biosensors are the biological recognition element which interacts with a target molecule with specificity, and the transducer element, that converts a property of this interaction into a measurable signal. Numerous biological recognition strategies have been employed over the years utilizing many molecules such as nucleic acids [3], antibodies [4], receptors [5], and, most specific to this work, enzymes [6]. A desirable feature of biosensors is a live interface between the *in vivo* analytes, the bio-recognition element, and the transducer, so that it is possible to have a real-time measurement describing the current state of a biological system.

Many transduction options have been explored, including optical methods [7], calorimetric methods [8], acoustic methods [9] and, as studied in this work, electrochemical methods which have become one of the most common biochemical measurements performed today [9]. Clark's subsequent glucose oxidase sensor [10] began a long and wide path of study into electrochemical biosensors still highly active today and has led to the successful development of sensors for real-world clinical impact as commercially available medical technology. Electrochemical sensors may rely on impedimetric, potentiometric, or amperometric signals to collect their data and the theory of operation of amperometric devices will be explained below as they are the chosen format for the devices fabricated in this work. The use of enzymes provides molecular specificity and long term reusability to such sensors, since the chosen enzyme element is a protein precisely intended as a reusable catalyst for particular biological chemical reactions. Amperometric enzymatic biosensors of

the form fabricated in this work function by monitoring a current when a fixed potential is applied between two electrodes with at least one electrode immersed in analyte solution with enzyme present. The operation of these devices has been previously demonstrated to function at the miniature scales sought in this work [11].

Designing biosensors requires careful consideration of both the dynamics of the target analyte and the complexity of the environment in which the measurement will operate. Interaction between the electrode material properties, analyte chemistry, and any ancillary environmental chemistry must be well understood to guarantee functionality and reproducibility of an electrochemical measurement. Carbon has long been favored as an electrode material, more recently in CNT and graphene forms [12], but common alternatives are the noble metals such as gold, platinum, and palladium [13]. Platinum may act as a transduction surface for oxidants such as hydrogen peroxide (H_2O_2) since a continual redox reaction and an electrical current may be formed at its surface without causing permanent changes to the platinum electrode surface.

Today's biosensors can be both simple to manufacture and cost-effective, and serve as tools for patient monitoring. There are a few forms they are currently deployed in depending on the analyte sampling method. The data measurement procedure can be performed by drawing analyte out of the body and feeding it to the sensor or, as in the goal of this work's devices, sensors may be implanted into the body to continuously measure changes in concentrations of the analyte of interest. It should be noted that the physical invasiveness of current implantable devices, due to their size, limits their application and functional lifetimes [14].

A host of impediments face *in vivo* amperometric sensors, including interference by non-target electroactive molecules, immune response molecules/cells that interrupt the enzyme layer or the transduction layer, fluctuations in delivery of analyte, fluctuations in the electrochemical/ionic environment, and device encapsulation. These concerns will be discussed further in this chapter and Chapter 3.

1.2 Biomedical Needs

Human health and disease management drives the needs for improved biosensor technology. The determination of glucose concentration in blood continues to be the most frequent application of electrochemical biosensors with 6 billion assays performed per day [15]. As of 2014, an estimated 422 million individuals are affected by diabetes mellitus worldwide [16], and optimal

management of this disease requires consistent monitoring of metabolic glucose concentrations in the body. Diabetes is a currently incurable disease resulting from an insufficiency or inaccurate utilization of insulin hormone in the body. This results in elevated or reduced blood-glucose concentration excursions from safe metabolic levels [17]. Long term effects can include blindness, renal failure, peripheral nerve damage, cardiovascular diseases, and other life threatening conditions. Since the disease's discovery, great efforts have gone into finding new ways to diagnose, monitor and treat the disease. A yet unsolved challenge that would benefit all affected patients is the creation of long term biosensors with simplified, inexpensive, pain-free, multiple-data-points-per-hour measurement capabilities that would enable efficient health management.

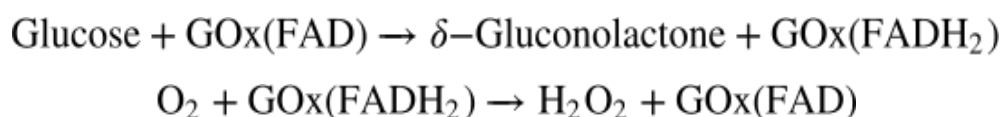
Monitoring blood glucose levels prolongs life expectancy by enabling diabetes patients to manage episodes of hypo- or hyperglycemia, hence reducing the amount of damage caused by the disease. This data may also be used to optimize patient treatment strategies and gain insight to the effects of diet, exercise and medication for the patient and for the population as a whole. Long-term glucose monitoring could also provide important clues into potential triggers for this disease, which are presently not understood. While direct blood monitoring is the ideal approach to diabetes management, as the circulatory system is the medium that delivers glucose to the various organs, this approach is inherently invasive to the body and glucose is often measured instead in the subdermal space.

1.3 Amperometric Enzyme Biosensors

Clark's first glucose sensors relied on the flavoprotein glucose oxidase (GOx) enzyme, which enabled high sensitivity measurements in the μM to mM concentration range and sufficient selectivity for glucose over other molecules present in complex biological samples. Although many alternative enzymes have been studied and optimized, GOx has endured as the most common platform because it can tolerate extreme changes in pH, temperature and ionic strength in comparison to other options, thus easing fabrication of sensors and providing environmental stability [18]. After first observations in the 1930s, Franke and Defner isolated GOx protein from *Aspergillus niger* in 1939 and determined that it contained flavin adenine dinucleotide (FAD) within its reaction center [19]. Maintaining the FAD binding has since become a consideration in enzyme lifetime. This co-factor molecule is essential to the electron mediation process of the enzyme and permits the

bond-breaking chemistry to occur outside of the enzyme structure itself, thus lowering the risk of denaturation.

GOx molecules catalyze the oxidation of glucose molecules into δ -gluconolactone while producing H_2O_2 as a product. In performing this oxidation, GOx enzyme utilizes its cofactor and reduces it to FADH_2 . A subsequent reaction with local O_2 produces the desired H_2O_2 molecules, and resets the FAD^+ cofactor. The H_2O_2 produced is then, depending on diffusion behavior, measured at the anode of the electrochemical device, in a reaction that produces 2 electrons per molecule. An alternative approach is to monitor with a cathodic potential, the decreasing concentration of O_2 reflecting the reaction progress.



Clark's 'first generation' glucose sensor physical design is still adapted for use today. In this format, a thin layer of the GOx enzyme is embedded in a semi-permeable membrane attached to an electrode surface which in his device observed the local O_2 concentration. For first generation sensors that oxidize H_2O_2 or reduce O_2 , a significant voltage is required which can drive side reactions with other biological electroactive species that 'interfere' with the reaction current signal. This issue has led to the development of sensors relying on mediator molecules, which react at lower oxidation bias potentials, to ferry electrons instead of H_2O_2 and O_2 . This generation is well known in non-laboratory settings in the form of "finger-pricking" ex-vivo glucose sensors that are commonly utilized by most type 2 diabetes patients. However, the effectiveness of the method is limited by the necessity to devote time, energy and experience discomfort during the process. Methodologies that eliminate the time gaps between measurements provide health benefits by not missing periods of hypo or hyperglycemia which often occur outside the manual sampling frequency that would be expected from a patient.

Amperometric enzyme biosensors have evolved through three main generations differentiated by electron transfer mechanism and relative placement of the components as delineated here:

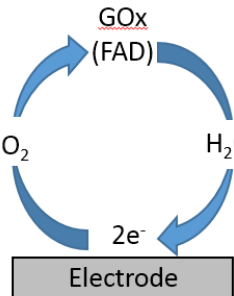
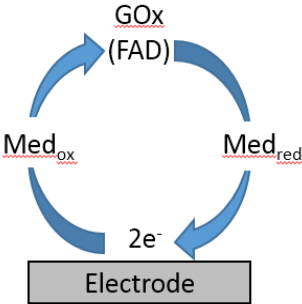
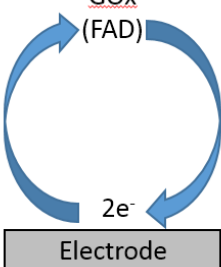
<p>1st Generation</p> 	<p>-Simplest starting materials.</p> <p>-Measures the concentration of analytes and/or products of enzymatic reactions that diffuse to the transducer surface and generate an electrical response.</p> <p>-Alternative name: 'mediatorless' devices.</p>
<p>2nd Generation</p> 	<p>-Employs 'mediator' molecules, to carry electrons between the enzyme redox centers and the electrode. This allows electrode functionality at lower voltages that affect fewer non-target sample molecules.</p> <p>-Mediator molecules must be added into the sensor construction and ideally contained near the surface. Mediator loss and toxicity are common drawbacks.</p>
<p>3rd Generation</p> 	<p>-Direct electron transfer between enzyme and electrode, either by binding the enzyme to the metal or to a conductive polymer matrix</p>

Table 1.1 Enzymatic glucose sensor generations

Two main classes of enzymes are employed in first generation and later sensors, the oxidases which promote the transfer of a hydrogen atom from a particular substrate to an O_2 molecule as previously described, and dehydrogenases that catalyze the removal of hydrogen atoms from a particular molecule. Oxidase enzymes rely on O_2 as a second substrate and as such their signals are sensitive to local oxygen concentration in addition to the target analyte. This dependence limits the environments in which such a sensor can be effective. Various strategies are employed to mitigate this drawback and are described below. Nonetheless, first generation sensors have still proven to be highly sensitive and are characterized by very fast response-times, often around one second. Due to toxicity drawbacks of the

dehydrogenase system and its complexity of fabrication, this work will focus on adapting first-generation technologies for implantable devices constructed with microfabrication tools.

1.4 Existing Technologies

The first commercially available glucose analyzers were developed by Beckman Instruments in 1968, which was soon followed by the Yellow Springs Glucose Analyzer from YSI Inc. in 1975. The YSI system has become the gold standard against which many new glucose sensors being developed for use are compared [15]. This analyzer utilizes electro-oxidation of H_2O_2 on a platinum surface with a protective membrane to limit the flux of analyte and other molecules. This membrane was made of layers of cellulose acetate (CA) and polycarbonate (PC) and the success of its application initialized a course for future device coating research. The PC is used to limit the analyte flux below the device saturation level, and the CA selectively filters electroactive molecules that would interfere with the H_2O_2 measurement. The current YSI 2300 model can handle one 25 μL sample every two minutes and measures glucose concentrations up to 50 mM with less than 2% error [20]. Subsequent commercial developments incorporated Ag/AgCl reference electrodes due to their long history as stable potential surfaces, to enable comparative three-electrode measurements to be discussed further below.

Medisense developed the first electrochemical blood-glucose monitors for individual patients in 1987 based on the 2nd generation modality which then became a ubiquitous implementation of electrochemical biosensors. These low-cost test strips, are fed into a handheld reader housing the measurement electronics, use carbon-paste electrodes and require small ($\leq 3 \mu\text{l}$) blood draw volumes per measurement. The modern test strip device has 5-10% error, relatively fast 5-15s scans and can be mass produced and shelf-stored for over a year [15]. The majority of a strip substrate is simply a mechanical handle that is electrically insulating, and the sensor portion is comparatively smaller. Continuing to shrink this sensor footprint has taken the form of wire or needle-type sensors in the 1980s and is continuing now in this decade to microfabrication scales [21]. Sensor fabrication has continued to utilize the manual processes of dipcoating and dropcoating the functional enzyme layer and protection layers, both of which can be difficult processes to calibrate. Through the 1990s, the subcutaneous implantable needle-type electrodes were developed by MiniMed to the point of commercial viability with their fabrication schemes sufficiently resolved. Present continuous glucose monitors (CGMs) sold by

Medtronic, Dexcom, and Abbott typically consist of a wireless handheld electronic reader, a ~1-2 inch-scale handle resting on the skin and a sensing element penetrating into the interstitial fluid below.

An early example of the needle type sensor was built by Zhang and Wilson [22] and took the form of a Teflon coated Pt wire with a separate AgCl wire coiled around it. The Pt wire was coated with GOx and CA by dipping into solution, and then also dipped into dissolved polymer solution to create a polyurethane topcoat. Heller and Feldman [23] developed a needle sensor of third generation approach around this same time and its construction consisted of an Au wire with GOx enzyme 'wired' to the electrode surface via osmium-polymer structures and contained additional coats of active enzyme interference-eliminating layers and biocompatible polymers on its surface. Today, Medtronic MiniMed Inc. and Dexcom offer needle-type sensors developed from the former format, Abbott Inc. has products developed from Heller's research, and a number of other companies have fielded products of similar technology.

1.5 Continuous Glucose Monitoring

The aforementioned transcutaneous devices are termed Continuous Glucose Monitors (CGMs) and extending the life-time of such sensors have been a critical research goal due to the benefits provided to patients and disease research. The first true in vivo CGMs were developed in the early 1970s in conjunction with an artificial pancreas to supply insulin [15] but this sensor was a benchtop device and the lack of portability made it infeasible to apply to general patients and the surgical requirements were highly invasive. The first fielded semi-implantable sensors were built by Medtronic in 2004 [24] and were far less invasive but still suffered from drift due to a variety of decay effects that limited their lifetimes to days and forced the devices to still be periodically re-calibrated via an ex-vivo measurement. Current CGMs can function up to 2 weeks without calibration [25] and measure every 1-4 minutes.

All of the currently fielded sensors operate on the described standard principles of placing glucose sensitive enzyme underneath a flux limiting membrane, and are constructed from a flexible wire or combination of wires acting as potentiostat electrodes inserted 5-10mm deep into the skin. Outer coatings were developed to take into consideration the immune response of the implantation, such as the tissue reorganization and blood flow changes at the access site, in order to maintain a stable measurement. Developing membranes to control molecular flux

and tissue response has been critical to realizing CGMs and are explored further in Chapter 6. Membranes serve multiple functions for these sensors: (i) they limit the glucose flow to below enzyme saturation levels so signals are linear, (ii) they limit glucose concentration below oxygen concentration since oxygen is an equally necessary substrate and peripheral tissues can be low oxygen environments, (iii) they prevent large molecule diffusion such as proteases that would destroy the enzyme, (iv) they may screen electroactive molecules, and (v) they may provide low-toxicity surfaces that the body incorporates and heals to without significantly altering blood flow or more specifically glucose flow.

Implanted CGMs are not intended to have direct access to blood, due to clotting effects and other complications and are commonly placed into the interstitial fluid (ISF) which has a correlated glucose concentration. ISF glucose levels have been measured with partial success with reverse iontophoresis methods as well [26] but transdermal needles are the only currently approved approach despite the drawbacks from leaving an open wound that stimulates a continual damaging immune response. Besides ISF and blood, glucose can be measured in urine, sweat, breath, saliva, and ocular fluid, with less correlation to the critical real blood concentration level but simpler construction requirements [27].

1.6 Sensor Performance Criteria

The metrics for what makes a good biosensor and the goals to pursue during fabrication have been resolved over decades of evaluations. The sensor must be able to perform with useful temporal resolution to describe the biological state. It must be sensitive enough to differentiate between analyte properties, i.e., concentrations of interest. Its limit of detection must match the reality of the biological sample, and its saturation point and behavior should be above biological feasible situations and not confuse the data collection. Tradeoffs must be made to balance the inherent advantages and disadvantage of each sensor type to work towards meeting all or specific criteria, such as balancing lifetime versus accuracy.

Sensitivity may be controlled by electrode material choices, voltage choices, or membrane choices. A membrane that blocks interfering molecules may end up limiting the analyte below the desired LoD. Membranes with good filtering properties may have biocompatibility issues that cause tissue inflammation.

Selectivity is inherently granted by the utilization of GOx enzyme in the sensor which has well characterized specificity [28]. Interferent filter layers are of course essential to signal selectivity since they counter the drawback of the electrode

surface itself not being selective. The voltage requirements are set by the ‘standard electrochemical potentials’ of the surfaces and molecules as described in the subsequent chapter. Second and third generation glucose sensor design research utilize mediator molecules with minimal voltage requirements.

Biocompatibility is essential to any in vivo device and can be described in two approaches as either seeking no reaction (inert-type material) or minimal unnatural perturbation (integrating-type material). The severity of immune response may impact must be considered for both the difficulty of the measurement created as well as the discomfort induced in the patient.

Temporal resolution is dependent on chemical reaction rates and diffusion stabilization of the sensor. When the input shifts or when the device is powered on or off, transients are introduced which require an in-depth understanding of the sensor dynamics for the sake of limiting electrical power utilization. Diffusion times scale roughly quadratically with distance, so shrinking the layer thickness from microns to hundreds of nanometers decreases the diffusion equilibration times by two orders of magnitude. Microfabrication techniques which give three-dimensional control over the functional enzyme layer surface, and analytical and simulation evaluation of the device construction enable the accurate use of short time scale measurements.

1.7 Potentiostatic Sensors

Potentiostats are the basis electronic hardware that performs amperometric measurements. Their primary function is to maintain a controlled voltage difference between a working electrode (WE) and a reference electrode (RE). These electrodes are in contact with a liquid cell and their solid-liquid junction potentials and the chemical reactions near their surface drive the dynamics of the system. A third electrode is often employed, as in this work, to allow a complete current flow within the cell while allowing the RE to be free of chemical reactions that are electrically driven thus maintaining a steadier cell bias potential.

A potentiostatic sensor records the current flow between the WE and CE and thus it is preferable that the electrode materials themselves vary little in behavior due to voltage or current effects so that only biorecognition signal is observed. Therefore, they are often made of a stable or noble material so that it may be employed repeatedly without dissolution or corruption of the desired chemical reaction measurement. The RE materials are chosen based on the expected environment such that their junction will maintain a constant potential throughout the expected concentration, pH, temperature, or other factor ranges. The CE completes the WE

circuit, but the chemical reactions occurring at its surface are often ignored since they are not relevant to the analyte measurement. They will be discussed in a later chapter since understanding the CE reaction is important to potentiostat and measurement design when designing sensors within miniaturized hardware constraints. The primary electrical components of the potentiostat circuit are the high impedance voltage meter (electrometer) which reads the WE-RE voltage and provides feedback control, and the control amplifier that generates the necessary WE-CE voltage to sustain the two-part redox reaction that would otherwise force the WE bias to decay. The current data is often measured over a shunt resistor which is balanced to the expected environmental load resistance and the dynamic range must be accounted for in the selected ADC approach.

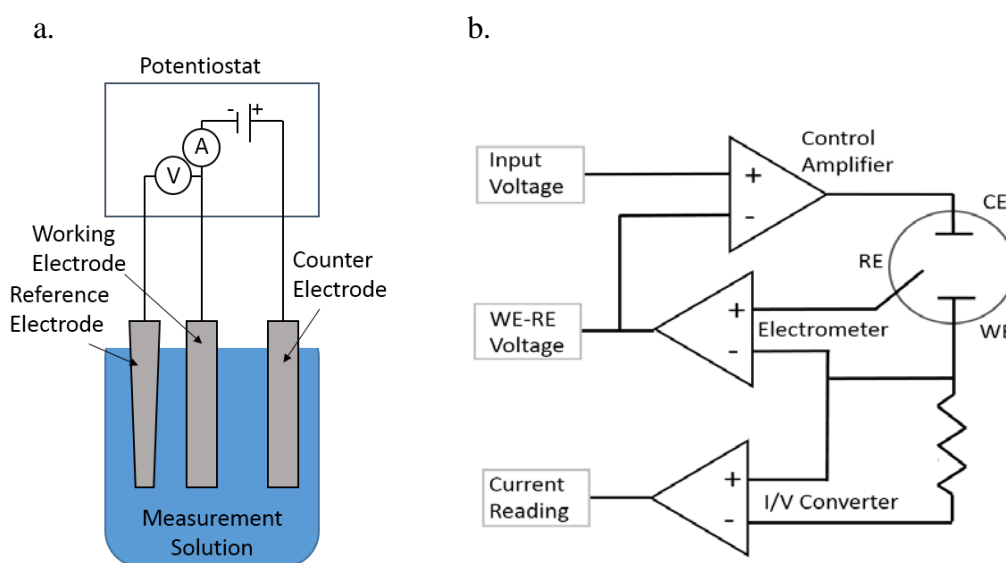


Figure 1.1 Schematic of a three-electrode potentiostat system (a) Simple model in solution (b) Example circuit

Amperometry or chronoamperometry is the use of these potentiostats for periodic or continuous current readings. In a biosensor, the enzyme immobilization layer is fabricated on top of the WE so reactions occur near it with the other two electrodes nearby to minimize solution impedance effects. An example of an unfunctionalized electrode set is shown in Figure 1.2, which was constructed in this work.

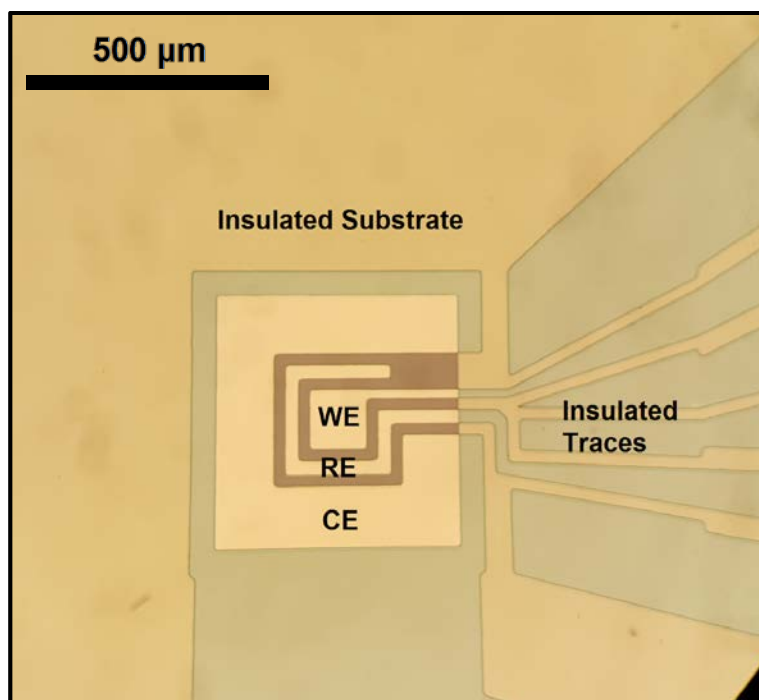


Figure 1.2 Example microfabricated 3-electrode set.
Complete wafer visible in Fig 5.9.

1.8 Microfabrication

The capabilities of microfabrication have expanded greatly over the past decades since the invention of the silicon transistor which drove the increased desire for high density solid state device circuits. These capabilities have begun to benefit biosensors as well [27] since material costs per device can decrease, microfabrication techniques can simplify and standardize accurate device construction, and biological interaction/sample volumes can be reduced. By consuming less analyte per measurement, sensors may stabilize faster, require shorter powering times and thus require less battery capacity. Top down microfabrication utilizing spincoating, photolithography, metal/insulator/polymer layer depositions, and the like have been employed over recent years to construct novel enzymatic-type sensors [29]. Ribet et al. have previously demonstrated microfabricated needle-shaped structures derived from silicon substrates for glucose sensor construction [30]. Developing planar electrode structures for enzymatic sensors via physical vapor deposition (PVD) methods is not that main challenge in adapting the full sensor technology, but consideration must be made of the resulting surface active site density. Our strategy for development of miniature sensors has been to adapt microfabrication techniques

to the deposition and patterning of enzyme layers and their barrier coatings. We demonstrate simultaneous fabrication of 10+ sensors in wafer-scale fabrication which is more difficult to achieve with current glucose sensor fabrication methods.

1.9 Wireless Implants

The primary goal of adapting microfabrication is to build devices that can reduce immune response while operating with high fidelity via miniaturization since immune response is injury-scale dependent [31]. Fully implantable style sensors are also preferable since they do not need further patient or doctor physical interaction thus causing less tissue disturbance. Patient costs may decrease for significantly long-lasting implants since consumable sensor strips are no longer necessary. Eliminating the transcutaneous aspect of such devices of course necessitates wireless communication to an external data collection/analysis point. UHF RF communication is a convenient approach due to its technological maturity and ability to operate with small scale antenna footprints and minimal power consumption [32,33]. Utilizing a CMOS platform for this purpose allows shrinking of the electrodes, control electronics, and signal processing/transmission system to these implant scales [33]. CMOS devices are constructed in massively parallel wafer fabrication in industrial foundries so adapting biosensor fabrication as a post-processing step would quickly enable high throughput manufacturing of many millions of complete sensor devices.

1.10 Goals

This work focuses on extending present microfabrication techniques to all parts of enzymatic sensor construction and to develop wafer-scale post-processing for manufacturable wireless CMOS sensors. We observed consistent sensor fabrication between devices on single substrate and between substrates and long term in vitro performance with high sensitivity in the target analyte ranges. Novel enzyme immobilization and topcoat methods are implemented on silicon substrates and adapted for CMOS-based wireless sensors. An understanding of amperometric enzyme-based biosensor construction requires interdisciplinary knowledge across electrochemistry, materials science, polymer synthesis, enzymology, electrical engineering, diffusion mechanics, and biological chemistry, which will be partially reviewed in these first chapters. Mathematical descriptions and characterization of such sensors is reasonably feasible in vitro but once in a biological environment, the

variety of variables involved creates major tractability challenges. This thesis will describe the fabrication techniques, modelling of the device behavior, and analysis of in vitro performance data.

References

- [1] N. Bhalla, P. Jolly, N. Formisano and P. Estrela, "Introduction to biosensors", *Essays In Biochemistry*, vol. 60, no. 1, pp. 1-8, 2016. Available: 10.1042/ebc20150001.
- [2] A. Hasan et al., "Recent Advances in Application of Biosensors in Tissue Engineering", *BioMed Research International*, vol. 2014, pp. 1-18, 2014. Available: 10.1155/2014/307519.
- [3] Y. Du and S. Dong, "Nucleic Acid Biosensors: Recent Advances and Perspectives", *Analytical Chemistry*, vol. 89, no. 1, pp. 189-215, 2016. Available: 10.1021/acs.analchem.6b04190.
- [4] S. Sharma, H. Byrne and R. O'Kennedy, "Antibodies and antibody-derived analytical biosensors", *Essays In Biochemistry*, vol. 60, no. 1, pp. 9-18, 2016. Available: 10.1042/ebc20150002.
- [5] R. Taylor, I. Marenchic and R. Spencer, "Antibody- and receptor-based biosensors for detection and process control", *Analytica Chimica Acta*, vol. 249, no. 1, pp. 67-70, 1991. Available: 10.1016/0003-2670(91)87009-v.
- [6] G. Rocchitta et al., "Enzyme Biosensors for Biomedical Applications: Strategies for Safeguarding Analytical Performances in Biological Fluids", *Sensors*, vol. 16, no. 6, p. 780, 2016. Available: 10.3390/s16060780.
- [7] M. Choi, "Progress in Enzyme-Based Biosensors Using Optical Transducers", *Microchimica Acta*, vol. 148, no. 3-4, pp. 107-132, 2004. Available: 10.1007/s00604-004-0273-8.
- [8] H. Aldewachi, T. Chalati, M. Woodroffe, N. Bricklebank, B. Sharrack and P. Gardiner, "Gold nanoparticle-based colorimetric biosensors", *Nanoscale*, vol. 10, no. 1, pp. 18-33, 2018. Available: 10.1039/c7nr06367a.
- [9] S. Vigneshvar, C. Sudhakumari, B. Senthilkumaran and H. Prakash, "Recent Advances in Biosensor Technology for Potential Applications – An Overview", *Frontiers in Bioengineering and Biotechnology*, vol. 4, 2016. Available: 10.3389/fbioe.2016.00011.

- [10] L. Clark and C. Lyons, "Electrode Systems for Continuous Monitoring in Cardiovascular Surgery", *Annals of the New York Academy of Sciences*, vol. 102, no. 1, pp. 29-45, 2006. Available: 10.1111/j.1749-6632.1962.tb13623.x.
- [11] M. Pohanka and P. Skládal, "Electrochemical biosensors - principles and applications", *Journal of Applied Biomedicine*, vol. 6, no. 2, pp. 57-64, 2008. Available: 10.32725/jab.2008.008.
- [12] Z. Zhu, L. Garcia-Gancedo, A. Flewitt, H. Xie, F. Moussy and W. Milne, "A Critical Review of Glucose Biosensors Based on Carbon Nanomaterials: Carbon Nanotubes and Graphene", *Sensors*, vol. 12, no. 5, pp. 5996-6022, 2012. Available: 10.3390/s120505996.
- [13] R. O'Neill, S. Chang, J. Lowry and C. McNeil, "Comparisons of platinum, gold, palladium and glassy carbon as electrode materials in the design of biosensors for glutamate", *Biosensors and Bioelectronics*, vol. 19, no. 11, pp. 1521-1528, 2004. Available: 10.1016/j.bios.2003.12.004.
- [14] S. Vaddiraju, I. Tomazos, D. Burgess, F. Jain and F. Papadimitrakopoulos, "Emerging synergy between nanotechnology and implantable biosensors: A review", *Biosensors and Bioelectronics*, vol. 25, no. 7, pp. 1553-1565, 2010. Available: 10.1016/j.bios.2009.12.001.
- [15] A. Heller and B. Feldman, "Electrochemical Glucose Sensors and Their Applications in Diabetes Management", *Chemical Reviews*, vol. 108, no. 7, pp. 2482-2505, 2008. Available: 10.1021/cr068069y.
- [16] G. Roglic, "WHO Global report on diabetes: A summary", *International Journal of Noncommunicable Diseases*, vol. 1, no. 1, p. 3, 2016. Available: 10.4103/2468-8827.184853.
- [17] "Diabetes", Who.int, 2019. [Online]. Available: <https://www.who.int/news-room/fact-sheets/detail/diabetes>. [Accessed: 21- May- 2019].
- [18] D. Bruen, C. Delaney, L. Florea and D. Diamond, "Glucose Sensing for Diabetes Monitoring: Recent Developments", *Sensors*, vol. 17, no. 8, p. 1866, 2017. Available: 10.3390/s17081866.
- [19] W. Franke and M. Deffner, "Zur Kenntnis der sog. Glucose-oxydase. II", *Annalen der Chemie*, vol. 541, no. 1, pp. 117-150, 1939. Available: 10.1002/jlac.19395410107
- [20] Ysi.com, 2019. [Online]. Available: <https://www.ysi.com/File%20Library/Documents/White%20Papers/Glucose-Analytical-Comparability-White-Paper-B91.pdf>. [Accessed: 21- May- 2019].

- [21] H. Yang, T. Chung, Y. Kim, C. Choi, C. Jun and H. Kim, "Glucose sensor using a microfabricated electrode and electropolymerized bilayer films", *Biosensors and Bioelectronics*, vol. 17, no. 3, pp. 251-259, 2002. Available: 10.1016/s0956-5663(01)00266-4.
- [22] Y. Zhang and G. Wilson, "In vitro and in vivo evaluation of oxygen effects on a glucose oxidase based implantable glucose sensor", *Analytica Chimica Acta*, vol. 281, no. 3, pp. 513-520, 1993. Available: 10.1016/0003-2670(93)85009-9.
- [23] B. Feldman et al., "FreeStyle™: A Small-Volume Electrochemical Glucose Sensor for Home Blood Glucose Testing", *Diabetes Technology & Therapeutics*, vol. 2, no. 2, pp. 221-229, 2000. Available: 10.1089/15209150050025177.
- [24] Professional.diabetes.org, 2019. [Online]. Available: <https://professional.diabetes.org/sites/professional.diabetes.org/files/media/db201811.pdf>. [Accessed: 21- May- 2019].
- [25] G. Cappon, G. Acciaroli, M. Vettoretti, A. Facchinetti and G. Sparacino, "Wearable Continuous Glucose Monitoring Sensors: A Revolution in Diabetes Treatment", *Electronics*, vol. 6, no. 3, p. 65, 2017. Available: 10.3390/electronics6030065.
- [26] "Accuracy of the GlucoWatch G2 Biographer and the Continuous Glucose Monitoring System During Hypoglycemia: Experience of the Diabetes Research in Children Network", *Diabetes Care*, vol. 27, no. 3, pp. 722-726, 2004. Available: 10.2337/diacare.27.3.722.
- [27] D. Bruen, C. Delaney, L. Florea and D. Diamond, "Glucose Sensing for Diabetes Monitoring: Recent Developments", *Sensors*, vol. 17, no. 8, p. 1866, 2017. Available: 10.3390/s17081866.
- [28] E. Adams, R. Mast and A. Free, "Specificity of glucose oxidase", *Archives of Biochemistry and Biophysics*, vol. 91, no. 2, pp. 230-234, 1960. Available: 10.1016/0003-9861(60)90495-1.
- [29] J. Yan, V. Pedrosa, A. Simonian and A. Revzin, "Immobilizing Enzymes onto Electrode Arrays by Hydrogel Photolithography to Fabricate Multi-Analyte Electrochemical Biosensors", *ACS Applied Materials & Interfaces*, vol. 2, no. 3, pp. 748-755, 2010. Available: 10.1021/am9007819.
- [30] F. Ribet, G. Stemme and N. Roxhed, "Real-time intradermal continuous glucose monitoring using a minimally invasive microneedle-based system", *Biomedical Microdevices*, vol. 20, no. 4, 2018. Available: 10.1007/s10544-018-0349-6.

[31] O. Veisheh et al., "Size- and shape-dependent foreign body immune response to materials implanted in rodents and non-human primates", *Nature Materials*, vol. 14, no. 6, pp. 643-651, 2015. Available: 10.1038/nmat4290.

[32] A. Agarwal et al., "A 4 μ W, ADPLL-based implantable amperometric biosensor in 65nm CMOS," *2017 Symposium on VLSI Circuits*, Kyoto, 2017, pp. C108-C109.

doi: 10.23919/VLSIC.2017.8008566

[33] M. Mujeeb-U-Rahman, M. Honarvar Nazari and M. Sencan, "A novel semiconductor based wireless electrochemical sensing platform for chronic disease management", *Biosensors and Bioelectronics*, vol. 124-125, pp. 66-74, 2019.

Available: 10.1016/j.bios.2018.09.077.

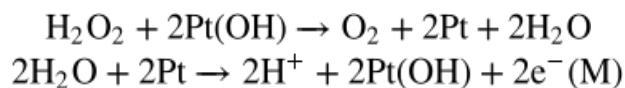
Chapter 2 Discussion on Device Electrochemistry

2.1 Redox Reaction Expectations

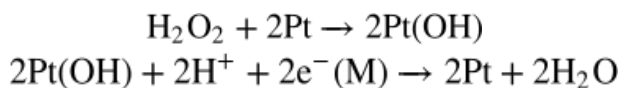
Electrochemistry is the study of chemical processes involving the transfer of electrons and changes of oxidation state. The monitoring of this flow of electrons, i.e., a current, serves as a direct measure of the dynamics of the processes occurring at the electrode surface. A number of DC and AC techniques have been developed to analyze and probe phenomena present therein. One of the most conventional methods is chronoamperometry, in which a constant potential is applied to an electrode and the resulting current is measured. Reduction and oxidation reactions (redox reactions), can be driven by inducing an electric field at the surface of an electrode. This change in the thermodynamic favorability of the reaction is in part dependent on the difference between the potential energy of the electrons in the electrode and the valence shells of the species. Potentiostats (described in section 1.7) can drive oxidation reactions for species near the electrode surface that undergo oxidation below the applied bias potential energy. The kinetics of the reaction must be taken into account, as well as the state of the electrode surface. For our high ionic strength solutions of interest, the characteristic decay length of the electric potential (Debye length) from the electrode into the solution is sub-nm (i.e., surface-based reactions). Due to the high speed of the platinum-peroxide redox reactions, for our typical peroxide concentration ranges, our observed signal is diffusion limited by the time for particles to reach the electrode surface. The nature of the platinum-hydrogen peroxide reactions and the measurement behavior will be explained further in this chapter. Some phenomena are given in reference to our fabricated devices which are described in Chapter 5.

The platinum redox process is electrochemical and involves the net transfer of charge to the electrode. By biasing platinum to either an oxidized or reduced surface state, hydrogen peroxide undergoes more catalytic breakdown by oxidation or reduction, respectively and this breakdown changes the state of the surface. The surface can then react with another hydrogen peroxide molecule, or the surface state can be changed by transfer of charge from the electrode, depending on the favored state (dependent on the bias). Under sufficient bias, one state is much more favored such that it is rapidly returned and effectively done so only electrochemically. The electrochemical reformation of the favored state is the actual process that causes the measured current in such junctions. The rate of this process is both proportional to the flow of electrons through the electrode and the flux of hydrogen peroxide at the

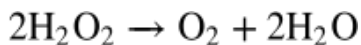
surface such that the current is a direct measurement of the hydrogen peroxide flux, which will have an approximately proportional steady state relationship to the bulk concentration of hydrogen peroxide in the cell. The following two step process is the most expected pathway on our positively biased WE [1]:



In the first step H_2O_2 catalytically breaks down at the platinum electrode surface, such that H_2O_2 and the previously oxidized platinum surface are oxidized and reduced, respectively. In the second step, an electron transfer occurs when platinum is encouraged to reoxidize by the bias. Since the first step does not involve net charge transfer whereas the second step does, this type of mechanism is referred to as a chemical-electrochemical (CE) mechanism. An analogous reduction reaction would occur at a platinum electrode biased in the negative direction (that is, in such a way that neutral metal surface is favored). As we employ a platinum counter electrode in our device, this process would be expected to contribute to the counter current:



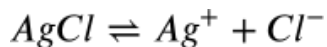
H_2O_2 will be preferentially reduced at the counter electrode as long as it is present, along with any O_2 present, but less ideally other solution species will reduce if neither are present. Interference reactions will be discussed in Section 3.4. Two half-reactions such as these can describe a full electrochemical cell but, as stated above, it is unlikely that these are the only reactions occurring at the electrodes. The specificity is more important at the working electrode, which should have a current only related to the concentration of peroxide in solution. Without any biasing, the cycle of oxidation and reduction at the surface forms to a catalytic process in which the surface does not have a net change, such that the reaction can be simplified to just the perspective of the hydrogen peroxide decomposition:



Which may be induced by platinum, other transition metals, or occur by thermal decomposition. This abbreviation misses the intricacies of the of hydrogen, oxygen, and hydroxide exchanges at the platinum surface which drive the true kinetics.

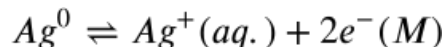
2.2 Electrode Behavior

For the potentiostat's third electrode, the reference electrode, we seek a stable junction voltage with respect to the solution, from which to reproducibly 'reference' the voltage bias of the WE. The materials that meet such criteria are rather limited and their fabrication can be complex [2]. Typically reference electrode construction generates a liquid junction that is in a solution partially isolated from the bulk but this geometry is not amenable to solid state microfabrication and the ideal volumes are inherently macroscale. The most common material choice for reference bioelectrodes is the silver chloride electrode, operating in a chloride solution. This type of electrode has been frequently used in commercial glucose sensors and were employed in this work for calibration purposes. The microfabrication of such electrodes is described in Section 5.2. Briefly, they are composed of metallic silver layer with a chloridized surface. Such electrodes are known as reference electrodes of the 'second kind' since the metal ion is not intended to transfer into solution and they can be described by basic Nernst potentials [3]. The redox equilibrium is described by:



where Cl^- ions dissolve in and out of solution. In our target application in vitro in physiologic saline and in vivo, the Cl^- concentration is approximately 140 mM. The metallic silver portion is intended to remain solid but its dissolution occurs as well in practice, the rate of which is faster in vivo than in vitro [2].

The half-cell equilibrium of such an electrode is determined from the balance of the chemical potentials of the chemical potentials (μ_i) of the solid electrode and the dissolved ions in solution. The chemical potential comes from the standard definition of free energy dependent on the number of particles of present species (n_i). The chemical potential for solutions in practice is calculated from the concentration of species which in turn can be more accurately described by the activity of the species (a_i). This can be broken into separate terms assuming no ion-ion interactions and an activity term [3] which accounts for ionic cloud self-interactions. The equilibrium description for a silver ion in solution is:



Balancing the electrons' potential field permits a voltage based equation to describe the equilibrium. This is known as the invaluable Nernst equation of electrochemistry

$$E = E^0 + \frac{RT}{zF} \ln a_{M^+}$$

The standard potentials are measured quantities given by collected tables [4]. They must be defined in reference to a particular repeatable electrode (e.g., the Standard Hydrogen Electrode [SHE]) and then offset for whichever reference electrode is used in measurement.

To describe the AgCl reference electrode we expand on the Ag ion half cell.

$$E_{Ag|Ag^+} = E_{Ag|Ag^+}^0 + \frac{RT}{F} \ln a_{Ag^+}$$

The generalized form of the Nernst equation for multiple species is:

$$E = E^0 + \frac{RT}{zF} \ln \left(\frac{\prod_{ox} a_{ox}^{v_{ox}}}{\prod_{red} a_{red}^{v_{red}}} \right)$$

Which gives us the full electrode's equation:

$$E_{Ag|AgCl|Cl^-} = E_{Ag|Ag^+}^0 + \frac{RT}{F} \ln \frac{a_{Ag^+} a_{Cl^-}}{a_{Cl^-}}$$

We can absorb the first half of logarithm, as the $a_{Ag}a_{Cl}$ solubility product is a constant, into a standard potential for the electrode such that we now reach an equation in response to the solution chloride activity:

$$E_{Ag|AgCl|Cl^-} = E_{Ag|AgCl|Cl^-}^0 - \frac{RT}{F} \ln a_{Cl^-}$$

We do not expect significant drift of the chloride concentration (or activity) in our in vitro solutions as we are maintaining voltage biases that avoid chloride consuming reactions. These reactions typically occur at greater than 1V vs Ag/AgCl on a platinum electrode in 7.4 pH 1x Phosphate Buffered Saline (PBS), whereas our bias in experiment is approximately 0.6 to 0.7V. As such we would expect a stable reference measurement with an Ag/AgCl reference electrode. The environment in vivo is far less stable as the ionic environment around the device can change due to immune system response and due to normal periodic nutrient variances [5].

For a reversible electrode such as Ag/AgCl, both the oxidation and reduction processes are occurring simultaneously. Individually, these reactions would lead to a change in the potential of the electrode relative to the solution, but together they maintain a constant equilibrium potential. The particular potential at which this equilibrium occurs is the potential at which the rate of both of the cell reactions are equal, such that there is no longer any net charge transfer to the solution. The equivalent current occurring in these balanced processes is referred to as the exchange current density, and since there is no net charge transfer, this current is hidden from the perspective of a connected device. For a well behaving Ag/AgCl electrode, this means that the rate of electrochemical interconversion between Ag and AgCl is equal at equilibrium. Dissolution of the AgCl layer over time leads to a situation in which the electrode must shift to more negative potentials in order to

supply positive charge. The lack of AgCl reactant causes the cell to lose its reversibility which was the basis of its stability. Silver is not a particularly biocompatible material and both the functionality and the construction are observed to fail in vivo unless precautions are taken [6].

The significance of the magnitude of exchange current density manifests when accounting for other charge transferring processes that could occur at the electrode such as other electrochemical reactions or other non-chemical charge perturbations. Possible electrochemical reactions with some other constituent of the solution would contribute additional potential dependent currents, which when comparable to the exchange current density can alter the equilibrium potential. In such situations when these other constituents also have time varying concentrations in the solution, the equilibrium potential will also vary with time. Similarly, if the exchange current density is comparable to some sort of leakage current into the attached electronics, then the equilibrium potential will also be altered by this leakage current. When also accounting for the electrode capacitance, the exchange current density can be viewed as a measure of how far the potential of the electrode will deviate when charge is transiently transferred to the electrode, and how quickly the electrode will return to the equilibrium potential after the transient. This conception is useful when considering the response of the electrode to electrically or mechanically induced noise.

2.3 Implemented Electrodes

For our present purposes of in vitro measurements we can suffice with a much simpler reference electrode construction by using the same material as the WE and CE, platinum. As mentioned above, platinum is a suitable material for implantable hydrogen peroxide sensing electrodes due to its inertness, low corrosion rate and fast reaction kinetics. Further, its stable cell potential in the expected hydrogen peroxide concentration range allows for its use as a reference electrode. The electrochemical behavior of a material can be better understood by considering its cyclic voltammograms (CV). From them we can detect the equilibrium reactions and their rates which determines the possible solution junction equilibria. CV measurements were performed in PBS as the glucose measurements are performed in this buffer to replicate an in vivo buffered environment (see Chapter 3). In vivo CV measurements were beyond the scope of this work. The ionic concentrations that constitute the Cold Spring Harbor PBS Protocol are: 137mM NaCl, 10mM Na₂HPO₄, 2.7mM KCl, 1.8 mM KH₂PO₄. This solution unfortunately provides chloride ions that oxidize on platinum as well as phosphates that may reduce, which narrows the

potential range of operation. Further, it is known that Cl^- ions affect the reaction kinetics of hydrogen peroxide on platinum, as well as the platinum metal reactions themselves [7]. An example CV performed under deoxygenated conditions is traced and annotated in Figure 2.1 for explanatory purposes

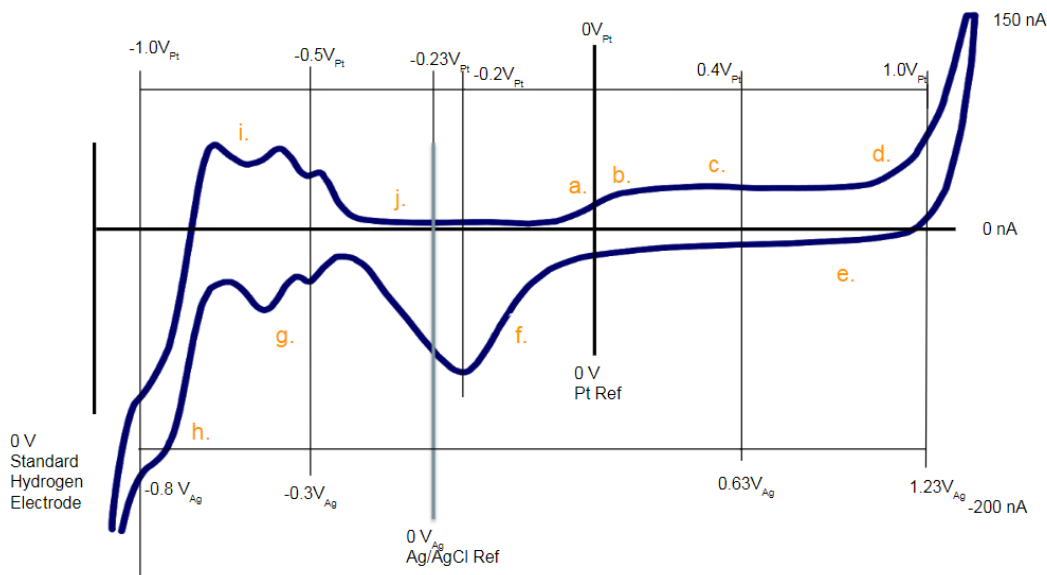


Figure 2.1 Platinum CV in deoxygenated PBS.

An ideal Ag/AgCl reference electrode voltage is marked as well as an expected platinum reference electrode voltage (for hydrogen peroxide-containing solutions) in the figure. A fabricated Ag/AgCl electrode in direct contact with PBS is not under chloride saturation so calibration measurements were performed with a traditional isolated saturated chloride cell with silver wire as this achieves a stable Nernst potential. An understanding of the platinum reactions throughout the voltage range provides insight to general expected sensor behavior and possible failure modes. In Figure 2.1:

- a-b.** Onset of reversible platinum oxide reactions and eventual irreversible place exchange reactions. $4\text{Pt} + \text{H}_2\text{O} \rightarrow \text{Pt}_4\text{OH} + \text{H}^+ + \text{e}^-$, $\text{Pt}_4\text{OH} + \text{H}_2\text{O} \rightarrow 2\text{Pt}_2\text{OH} + \text{H}^+ + \text{e}^-$, $\text{Pt}_2\text{OH} + \text{H}_2\text{O} \rightarrow 2\text{PtOH} + \text{H}^+ + \text{e}^-$
- c.** Irreversible place exchange reactions and onset of platinum oxide formation. $\text{PtOH} \rightarrow \text{PtO} + \text{H}^+ + \text{e}^-$
- d.** Chloride oxidation and at higher voltages, oxygen evolution $\text{H}_2\text{O} \rightarrow \text{O}_2 + 4\text{H}^+ + 4\text{e}^-$

- e. Platinum oxide reduction $\text{Pt(OH)} + \text{H}^+ \rightarrow \text{Pt} + \text{H}_2\text{O}$, $\text{PtO} + 2\text{H}^+ \rightarrow \text{Pt} + \text{H}_2\text{O}$
- f. Hydrogen adsorption peaks (two Pt crystal affinities visible)
- g. Phosphate reduction and hydrogen evolution
- h. Hydrogen desorption peaks (two Pt crystal affinities visible)

For thorough examinations of the platinum-PBS reactions see Khudaish [7], Kieninger [8], or Hudak et al [9]. Our primary concerns are the oxidation and reduction reactions which will occur at the WE and CE in our device. H_2O_2 reduction overlaps with O_2 reduction voltages and, as seen in the redox equation oxygen is a byproduct of the H_2O_2 decomposition pathway. Other pathways are also proposed but are outside the scope of this summary [1,10]. Increasing the concentration of oxygen in solution will increase the reduction current available as seen in Figure 2.2. Addition of H_2O_2 increases both oxidation and reduction currents significantly within the reasonable bias ranges in PBS. The chronoamperometric measurement at 0.4V vs Pt RE, where significant hydrogen peroxide current is evident in the CV, is our desired sensor data.

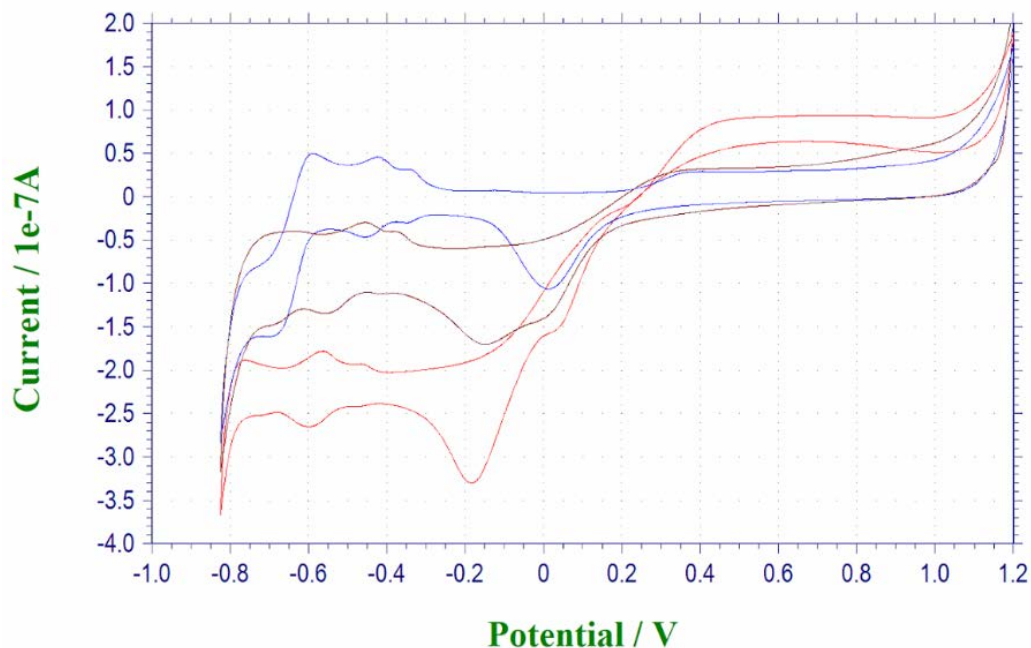


Figure 2.2 CV of platinum electrodes in PBS. Deoxygenated (blue), oxygenated (brown), and peroxide-containing PBS (red). 0.1V/s scanrate vs. Ag/AgCl RE. Platinum WE and CE visible in Figure 1.2.

As can be expected, potentiostat operating current and driving voltages are highly dependent on the available species for oxidation, reduction, and equilibrium reactions. For wireless implantable devices the available voltage range is often limited so we desire that the WE reaction and CE reaction occur within $<0.8V$ of each other. This will fail if sufficient amounts of H_2O_2 or O_2 are not available at the CE. Another crucial failure mode is reference electrode drift since robust construction options are limited [2]. Positive voltage drift $\sim 0.1V$ will increase the amount of H_2O_2 oxidized and negative drift will decrease the amount, raising or lowering the output signal respectively, and indicating an erroneously concentration. At highly positive voltage drifts chlorine may further poison the platinum surface. A number of other chemical reactions can occur within this potentiostat voltage range and those will be discussed in Chapter 3. The in vitro test solutions are absent of these interfering molecules unless specifically evaluated.

A platinum electrode at equilibrium with oxygenated PBS solution will rest at approximately $0.3V - 0.4V$ (vs Ag/AgCl) and with moderate peroxide concentrations added approximately $0.2V - 0.25V$ (vs Ag/AgCl) if the electrode has not undergone significant poisoning or permanent oxidation processes. This balance point is highly dependent on the bias history of the surface and the oxygen and peroxide concentrations as they distribute or remove adsorbed oxygen from the platinum. The equilibrium potential of the platinum reference can be considered through the exchange current density in a way analogous to that of the Ag/AgCl electrode. Oxygen undergoes reduction on a reduced platinum surface, which leads to a positive shift in the charge of the electrode. When the electrode is sufficiently positive, the platinum begins to undergo oxidation, which lowers the surface area available for oxygen reduction. When the surface is fully oxidized, reduction of oxygen no longer occurs and the electrode does not become more positively charged. Since there is no directly paired oxidation process, the electrode is not reversible or particularly stable. However, in solutions with hydrogen concentrations far above those available in PBS, platinum is utilized as a reference electrode in the form of the SHE.

For a fully reduced platinum electrode, there is a region between the onset of platinum oxidation and hydrogen adsorption in which only double layer capacitive charging occurs and there is no strongly preferred equilibrium potential. A similar but more complex situation occurs with an electrode that has been previously oxidized. Platinum oxidizes to an extent that is dependent on the potential applied to it and the duration of the application. If the electrode is held at a particular oxidizing potential until the current has approximately completely diminished, then it will show

only double layer charging behavior in the potential region between that oxidation potential and the onset of platinum reduction. The onset of platinum reduction does not become more positive as the electrode is further oxidized, and in fact becomes somewhat more negative with further oxidation due to progressively irreversible place-exchange processes occurring in the surface. This means that an oxidized platinum electrode also does not show a preferred equilibrium potential. See Angerstein-Kozlowska [11] and Kadiri et al [12] for deeper study on platinum oxidation and the oxygen-platinum reaction respectively. Although the presence of oxygen can lead to the oxidation of platinum, the irreversibility of the overall oxidation process leads to a situation in which the oxidized platinum electrode again must be brought significantly negatively in order to begin platinum reduction and again provide surface area to continue oxygen reduction.

As can be seen Figure 2.2, there is a potential dependence to the additional current measured at the electrode in the presence of hydrogen peroxide. Near the open circuit potential, the current change could be interpreted as representing a net shift from equal oxidation and reduction to one or the other. At negative potentials, the additional current is fairly constant, and it likely also includes some oxygen reduction current, both from the solution, previously oxidized hydrogen peroxide and hydrogen peroxide being oxidized at the counter electrode. The current at oxidation potentials is somewhat subtler, as it reaches a maximum and then starts decreasing before chloride oxidation begins and obscures any further hydrogen peroxide oxidation trends. It has been stated in the literature that more oxidized forms of platinum such as PtO have slower kinetics for hydrogen peroxide oxidation. However, it is not clear from the CV data or the literature what is the nature of the potential dependence of the peroxide-platinum decomposition rate. Until a definitive answer is found, accurate modeling of the hydrogen peroxide gradient from the electrode will be beyond reach.

Unlike oxygen, hydrogen peroxide reacts on both oxidized and reduced platinum. As mentioned above, these reactions themselves are not electrochemical and do not directly lead to a change in the potential of the electrode. Instead, they can be considered to, perhaps overly simplistically, switch the redox state. In other words, hydrogen peroxide would lead to reduced platinum on a previously fully oxidized surface, and vice versa. The utility of this interpretation can be seen when considering a platinum electrode that is fully covered in oxide and positively charged, such that hydrogen peroxide will then cause some of the surface to be reduced. Since the reduced state is not favored at that positive potential, the surface will be electrochemically converted to oxidized platinum, which will cause the overall

electrode potential to be less positive than before. A similar but reversed process would occur at a fully reduced platinum electrode that was negatively charged past the point of full reduction.

As each of these processes continue, they would then lead to a state in which the electrode has an equal mixture of both oxidized and reduced surface states and the potential no longer shifts. In other words, these opposing processes lead to an equilibrium potential for a platinum electrode in the presence of hydrogen peroxide. A practical complication is that the oxidation of hydrogen peroxide produces oxygen, which then can undergo reduction on reduced platinum surfaces. The extra current contribution causes the equilibrium potential to have a dependence related to the ratio of hydrogen peroxide to oxygen concentration, where the equilibrium potential shifts progressively more positive to a potential at which the electrode is fully oxidized as the oxygen concentration becomes relatively larger.

A visualization of a three platinum electrode system in peroxide solution is given in Figure 2.3. However, CV cannot elucidate the true behavior when operating amperometric measurements at general voltages since it observes double-layer capacitance and pseudocapacitance formation at the junctions at its common sweep speeds, whose effects rapidly diminish in CA.

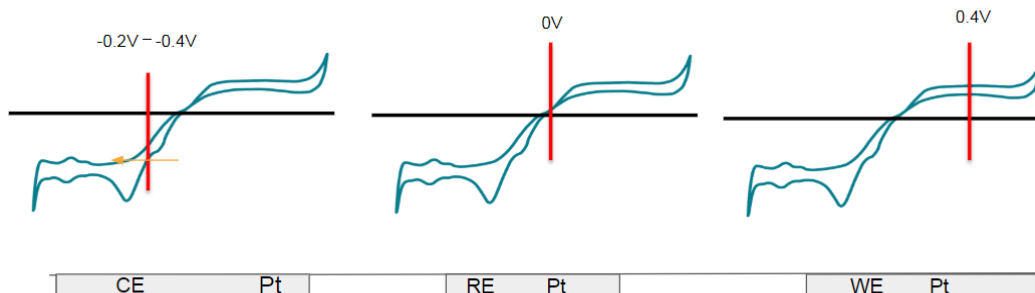


Figure 2.3 Visualization of voltage behavior of three platinum electrode system. RE rests at a balance between oxidation and reduction, WE is biased from that position, and CE will drive whichever voltage is necessary to match the current at the WE.

The surface reaction rate of H_2O_2 with Pt is known to be more rapid than the other kinetics of the device [7]. This can be immediately evidenced by the linearity of the peroxide-platinum reaction to concentration for our devices (see Figure 2.4).

The active site saturation behavior of the reaction occurs at concentrations beyond those utilized in our calibrations or present in our enzyme measurements.

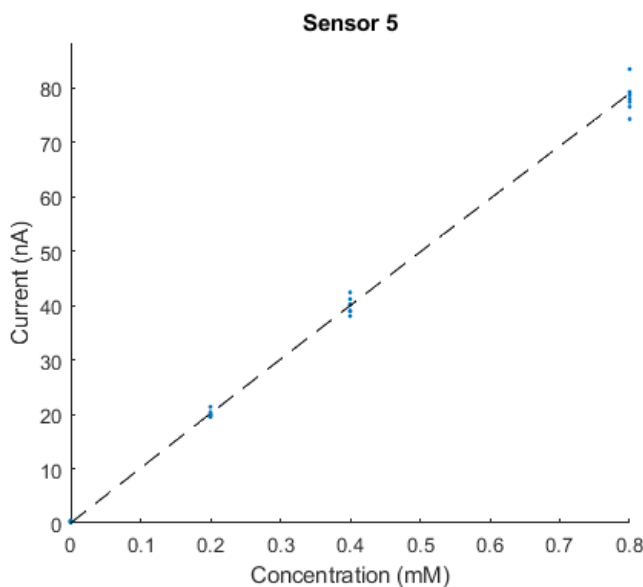


Figure 2.4 H_2O_2 oxidation current versus concentration on microfabricated Pt electrodes.

As such, platinum is not typically considered with Nernstian or Butler-Volmer reactant balances. Our expected currents are purely diffusion based as given by Cottrellian evaluation and we have observed as such with the microfabricated platinum electrodes utilized in this work. Unfortunately isolated the behavior of an electrode is difficult to observe in our configuration (see Fig 1.2) as they are all within plane to each other at sub $<20\mu\text{m}$ distances. Thus extracting the reaction speed of a single electrode from the consumption by the other electrodes and the drift of species between them will take further study.

A current at an electrode immediately reacting all of a species can be described by [3]:

$$j = nFD \left. \frac{\partial[C]}{\partial x} \right|_{x=0}$$

which is the form used to define the electrode surface boundary in the numerical simulations of Chapter 4. The time dependent behavior is given by solving Fick's second law of diffusion for the 0 surface concentration boundary and C_0 bulk fluid boundary. However, attempting to measure the platinum-peroxide reaction will not have satisfactory time boundary conditions since the decomposition reaction occurs without the applied measurement bias. The typical behavior is given by the 1D or 3D spherical Cottrell equations for a 0 concentration surface:

$$1D: \quad j = nF[C_0] \sqrt{\frac{D}{\pi t}} \quad 3D: \quad j = nFD[C_0] \left(\frac{1}{\sqrt{(\pi Dt)}} + \frac{1}{r_0} \right)$$

We can observe a time dependent decay in our calibration data but for the previously stated reasons: decomposition before measurement, and complex 3D interactions due to the small size of the electrodes and their proximity, we cannot immediately extract parameters.

An understanding of the voltages, currents, and chemistry required in a peroxide sensor informs design choices for the potentiostat, the electrode materials, and the expected measurement dynamics, which will be expanded upon in Chapter 4, and direct measurements given in Chapter 5. As discussed, considerations must be made for the valid in solution application ranges of Ag/AgCl RE, Pt WE/CE, and Pt RE. Our in vitro glucose data collections have borne out the well-known behavior of Pt WE/CE and the predicted functionality of the Pt RE. Further study made be made utilizing microfabricated platinum electrodes to explore surface species drift effects on the aforementioned critical surface states.

References

- [1] I. Katsounaros et al., "Hydrogen peroxide electrochemistry on platinum: towards understanding the oxygen reduction reaction mechanism", *Physical Chemistry Chemical Physics*, vol. 14, no. 20, p. 7384, 2012. Available: 10.1039/c2cp40616k.
- [2] M. Shinwari, D. Zhitomirsky, I. Deen, P. Selvaganapathy, M. Deen and D. Landheer, "Microfabricated Reference Electrodes and their Biosensing Applications", *Sensors*, vol. 10, no. 3, pp. 1679-1715, 2010. Available: 10.3390/s100301679.
- [3] C. Hamann, A. Hamnett and W. Vielstich, *Electrochemistry*. Weinheim: Wiley-VCH, 2007.
- [4] A. Bard and L. Faulkner, *Electrochemical methods*. New York [u.a.]: Wiley, 1980.

- [5] N. Yunos, R. Bellomo, D. Story and J. Kellum, "Bench-to-bedside review: Chloride in critical illness", *Critical Care*, vol. 14, no. 4, p. 226, 2010. Available: 10.1186/cc9052.
- [6] P. Hashemi et al., "Chronically Implanted, Nafion-Coated Ag/AgCl Reference Electrodes for Neurochemical Applications", *ACS Chemical Neuroscience*, vol. 2, no. 11, pp. 658-666, 2011. Available: 10.1021/cn2000684.
- [7] E. Khudaish, "The electrochemical oxidation of hydrogen peroxide on platinum electrodes at phosphate buffer solutions", Ph.D dissertation in Chemistry, Massey University, Palmerston North, New Zealand, 1999.
- [8] J. Kieninger "Electrochemical Microsensor System for Cell Culture Monitoring", Ph.D dissertation, University of Freiburg, 2011.
- [9] E. Hudak, J. Mortimer and H. Martin, "Platinum for neural stimulation: voltammetry considerations", *Journal of Neural Engineering*, vol. 7, no. 2, p. 026005, 2010. Available: 10.1088/1741-2560/7/2/026005.
- [10] R. Serra-Maia et al., "Mechanism and Kinetics of Hydrogen Peroxide Decomposition on Platinum Nanocatalysts", *ACS Applied Materials & Interfaces*, vol. 10, no. 25, pp. 21224-21234, 2018. Available: 10.1021/acsami.8b02345.
- [11] H. Angerstein-Kozłowska, "The real condition of electrochemically oxidized platinum surfaces Part I. Resolution of component processes", *Journal of Electroanalytical Chemistry*, vol. 43, no. 1, pp. 9-36, 1973. Available: 10.1016/0368-1874(73)80226-6.
- [12] F. El Kadiri, R. Faure and R. Durand, "Electrochemical reduction of molecular oxygen on platinum single crystals", *Journal of Electroanalytical Chemistry and Interfacial Electrochemistry*, vol. 301, no. 1-2, pp. 177-188, 1991. Available: 10.1016/0022-0728(91)85468-5.

Chapter 3 Sensor Chemical Environment and Reactions

3.1 Enzymatics

Sensors dependent on chemical reactions are driven by the input molecule concentrations, characterized by output molecule concentration, and reliant on the thermodynamically determined interaction rates of each step between analyte arrival and signal transduction. For enzymatic sensors, this takes the form of a substrate concentration [S], product concentration [P], and rate factors k_i that specify the number of reactions per molecule per time. Enzymes are by definition tools that modify reaction rates so rate evaluation is the fundamental component of their study. This section will be a brief overview of the standard reaction kinetics involved with a fabricated glucose oxidase sensor and the formulas explained here are utilized in simulations and evaluations in the following chapters.

Rate laws for chemical reactions are typically power law relations, as shown below for the first order reaction equation which is the familiar half-life decay formula [1].

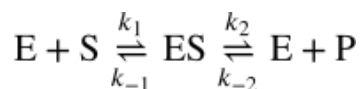
$$\frac{d[S]}{dt} = -k[S]$$

$$\ln\left(\frac{[S]}{[S_0]}\right) = -kt$$

$$[S] = [S_0] \cdot e^{-kt}$$

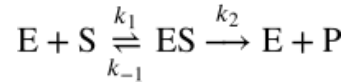
We will consider first order decay as part of our dynamics specifically in regard to H_2O_2 which experiences both thermal composition and collisions with tissue and polymer leading to a redox reaction [2]. The half-life of H_2O_2 is exceedingly brief in vivo due to catalases released by cells, and abundance of metal ions such as iron [3].

Next, we will consider a typical enzyme pathway to discern its overall rate equation. An enzyme (E) that catalyzes the substrate (S) to product (P) is described by the following form:



The overall rate of catalysis V , which is the number of moles of product formed per second, will vary with [S] and [E], and we consider only a fixed $[E_0]$ supply which is sometimes occupied in bound form. Total enzyme molecule gain or loss will not be considered, as it is not an intentional behavior in immobilized enzyme

sensors. The reaction will proceed during collisions until saturation effects occur as substrate [S] begins to exceed available enzyme [E]. The standard model for simple enzyme kinetic analysis, proposed by Michaelis and Menten (M-M) in 1913 [4], takes into consideration [ES] as an intermediate occupation, and typically considers the product back-reaction negligible.



We have three rate constants, which overall determine the binding affinity of the [ES] complex and the product creation rate. The latter is the starting point for the goal of building an equation that relates the V to our concentrations.

$$V = \frac{d[P]}{dt} = k_2[ES] \quad (1)$$

$$\frac{d[E]}{dt} = k_1[E][S] + (k_2 + k_{-1})[ES] \quad (2)$$

$$\frac{d[S]}{dt} = k_1[E][S] + k_{-1}[ES] \quad (3)$$

$$\frac{d[ES]}{dt} = k_1[E][S] - (k_2 + k_{-1})[ES] \quad (4)$$

And now considering the pseudo steady state operation of the enzyme with respect to substrate we can simplify these equations. Using initial values $[E_0]$, and $[E] = [E_0] - [ES]$ and $[ES_0] = 0$, (4) becomes:

$$\begin{aligned} \frac{d[ES]}{dt} &= k_1([E_0] - [ES])[S] - (k_2 + k_{-1})[ES] \\ \frac{d[ES]}{dt} &= k_1[E_0][S] - (k_1[S] + k_2 + k_{-1})[ES] \end{aligned}$$

Solution form of $y' = ay - b$ is $y = b/a - b/a * e^{at}$ and we only need the $t=0$ solution.

$$\frac{b}{a} = \frac{k_1[E_0][S]}{k_1[S] + (k_2 + k_{-1})}$$

Giving:

$$[ES] = \frac{[E_0][S]}{[S] + \frac{(k_2 + k_{-1})}{k_1}}$$

From which we reach the practically valuable M-M coefficient, which represents the ratio of complex formation and breakdown:

$$\begin{aligned} K_M &= \frac{(k_2 + k_{-1})}{k_1} \\ [ES] &= \frac{[E_0][S]}{[S] + K_M} \end{aligned}$$

And from equation (1) we get the M-M equation:

$$V = \frac{dP}{dt} = \frac{k_2[E_0][S]}{[S] + K_M} = \frac{V_{max}[S]}{[S] + K_M}$$

The maximal rate occurs when all enzymes are occupied.

$$V_{max} = \frac{dP}{dt}_{max} = k_2[ES]_{max} = k_2[E_0]$$

We can see when $[S]$ is small compared to K_M the response is linear in nature. Which is a preferable condition to be in for signal fidelity in a biosensor. The aforementioned filtering or topcoat layers which slow down analyte delivery to the biosensor help maintain that linear signal. And it is at $[S] = K_M$ that we reach $V_{max}/2$ which is somewhat indicative of where linearity ends. In comparison to K_M , which regards the first half of the chemical process, k_{cat} is defined as the turnover rate per enzyme which in this case is just k_2 . The ratio of the two is often used as a metric or figure of merit in considering enzyme performance in physiological conditions, where enzymes are evolutionarily optimized for their analyte ranges.

The K_M and V_{max} of an enzyme system can be derived from experimental data when analyte concentrations are controlled and product is accurately measured. The coefficients may be found by directly curve-fitting the $[S] - V$ response, or can be reformed by the Lineweaver-Burk method as a simple linear regression fit when the analyte and output are inverted.

$$\frac{1}{V} = \frac{K_M}{V_{max}} \frac{1}{[S]} + \frac{1}{V_{max}}$$

This approach is employed in Matlab scripts for data analysis in the following chapters, but is plotted in non-inverted form.

This formulation is most appropriate when product is being measured at the site of creation without product loss. This situation is not true for many biosensors, but we may still approximate their behavior with M-M analysis. An amperometric enzymatic sensor using diffusive electron mediators will experience product signal loss due to bulk diffusion loss and other transduction inefficiencies. Literature often defines a K_M^{app} and V_{max}^{app} which are found by curve fitting the sensor response, and they are a valuable tool for comparing performance between sensors which we use in the device descriptions in later chapters.

In the interest of better relating sensor-to-sensor and sensor over time performance for a single fabrication strategy, an exponential fit function is utilized in our approach as well since our devices have diffusion gradients and bi-substrate dependence which are not accounted for in standard M-M analysis. The coefficients are as follows:

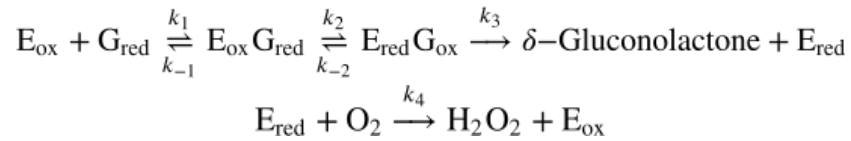
$$V = a \cdot (1 - e^{-b \cdot [S]})$$

$$s = \left. \frac{dV}{d[S]} \right|_{[S]=0} = ab$$

$$\kappa_p = \frac{1}{b}$$

Parameter ‘s’ serves at the sensitivity (nA/mM) metric, and κ_p identifies the “knee parameter” of the exponential which provides a metric for the useable device concentration range similar to K_M .

Glucose oxidase’s bi-substrate functionality means we must extend standard M-M kinetics to what is termed a ‘ping pong’ mechanism [5]. After the enzyme performs its main function of oxidizing glucose, to be regenerated it in turn must be re-oxidized, which is performed by molecular O_2 in its natural application (and in first generation sensors). A large portion of biochemical reactions are multi-substrate and cofactor molecules may either be freely available or in the case of GOx, held locally to undergo the redox reaction ($FAD \leftrightarrow FADH_2$). GOx is manufactured with the intention of being already paired with its cofactor, and environmental availability of the cofactor is negligible so FAD loss in a biosensor is considered a component of enzyme functionality loss, other possible causes being enzyme deherence or denaturation. As such it is not treated with allosteric dynamics and our observations in vitro, to be described later, agree the enzyme can function for many months. Further study may be placed on slowing down FAD loss from the biosensor structure if it determined to be a significant failure mode. The GOx pathway may be described in the following form:



We can follow a similar pseudo steady state analysis as before.

$$V = \frac{d[P]}{dt} = k_3[E_{red}G_{ox}] \quad (5)$$

$$\frac{d[E_{ox}G_{red}]}{dt} = 0 = k_1[E_{ox}][G_{red}] - k_{-1}[E_{ox}G_{red}] - k_2[E_{ox}G_{red}] + k_{-2}[E_{red}G_{ox}] \quad (6)$$

$$\frac{d[E_{red}G_{ox}]}{dt} = 0 = k_2[E_{ox}G_{red}] - k_{-2}[E_{red}G_{ox}] - k_3[E_{red}G_{ox}] \quad (7)$$

$$\frac{d[E_{red}]}{dt} = 0 = k_3[E_{red}G_{ox}] - k_4[E_{red}][O_2] \quad (8)$$

Some factors to compact and simplify the coming rate equations:

$$\beta = k_{-1}k_{-2} + k_{-1}k_3 + k_2k_3$$

$$\alpha = k_1(k_{-2} + k_3) + k_1k_2$$

Rearranging equations (6-8)

$$[E_{ox}G_{red}] = \frac{k_1[E_{ox}][G_{red}](k_{-2} + k_3)}{\beta} \quad (9)$$

$$[E_{red}G_{ox}] = \frac{k_1k_2[E_{ox}][G_{red}]}{\beta} \quad (10)$$

$$[E_{red}] = \frac{k_3[E_{red}G_{ox}]}{k_4[O_2]} \quad (11)$$

Plugging (10) into (11 and 5)

$$[E_{red}] = \frac{k_3k_1k_2[E_{ox}][G_{red}]}{k_4[O_2]\beta} \quad (12)$$

$$V = \frac{k_3k_1k_2[E_{ox}][G_{red}]}{\beta} \quad (13)$$

Now considering the total available enzyme:

$$[E_{tot}] = [E_{ox}] + [E_{ox}G_{red}] + [E_{red}G_{ox}] + [E_{red}]$$

$$[E_{tot}] = [E_{ox}] + [E_{ox}] \frac{k_1[G_{red}](k_{-2} + k_3)}{\beta} + [E_{ox}] \frac{k_1[G_{red}]}{\beta} + [E_{ox}] \frac{k_1k_2k_3[G_{red}]}{k_4[O_2]\beta}$$

$$\beta[E_{tot}] = [E_{ox}](\beta + [G_{red}](\alpha - \frac{k_1k_2k_3}{k_4[O_2]}))$$

Plugging back into (13):

$$V = \frac{k_1k_2k_3[G_{red}]}{\beta} \frac{\beta[E_t]}{\beta + [G_{red}](\alpha - \frac{k_1k_2k_3}{k_4[O_2]})}$$

Rearranging:

$$V = \frac{k_1k_2k_3[G_{red}][O_2][E_t]}{\beta[O_2] + [G_{red}]\frac{k_1k_2k_3}{k_4} + [O_2][G_{red}]\alpha}$$

$$V = \frac{\frac{k_1k_2k_3}{\alpha}[E_t][G_{red}][O_2]}{\frac{\beta}{\alpha}[O_2] + \frac{k_1k_2k_3}{\alpha k_4}[G_{red}] + [O_2][G_{red}]}$$

Simplifying with:

$$V_{max} = [E_t] \frac{k_1 k_2 k_3}{\alpha}$$

$$K_G = \frac{\beta}{\alpha}$$

$$K_{O_2} = \frac{k_1 k_2 k_3}{k_4 \alpha}$$

We reach our goal of the overall bisubstrate reaction rate. This will be employed in simulations in the subsequent chapter.

$$V = \frac{V_{max} [G_{red}] [O_2]}{K_{O_2} [G_{red}] + K_G [O_2] + [G_{red}] [O_2]} \quad (14)$$

Glucose oxidase based sensors are often simplified with single-substrate kinetics in literature which can fail to account for environmental fluctuations or is valid in sufficiently stable oxygen environments. It's clear from equation 14 that, if one of the substrates is held constant, it will return to standard single substrate M-M behavior. Enzyme kinetics also have pH and temperature dependencies which will not be considered in the following analysis. A design goal in biosensor construction is to ensure that analyte availability matches the optimal ranges for the enzyme(s) employed so comparing K_M values with expected in vivo concentrations is crucial. These numbers will be discussed in the follow section, and numerical evaluations will be made in Chapter 4.

3.2 Analyte Ranges:

Before continuing through discussion on impediments, it is necessary to consider the properties of the analytes of interests for predicting sensor behavior. Glucose ($C_6H_{12}O_6$) is an abundant carbohydrate throughout the human body and bloodstream. When glucose homeostasis is correctly functioning, blood sugar concentration is maintained in the range of **4.4mM to 6.1mM** [6]. It is delivered to all tissues as a primary cell energy source via the bloodstream and its cellular uptake is regulated by insulin hormone [7]. Hyperglycemia and hypoglycemia may be considered as events that push the bloodstream concentration out of this range, to over **11.1mM** or below **3.3mM** temporarily, or as sustained averages away from the mean of $\sim 5mM$. As stated previously, these excursions in concentration place stress on the operation of various organs and can lead to fatal reactions such ketoacidosis

when exceeding 16.6mM. At the other extreme, hypoglycemia results in impairments due to a lack of metabolic energy for organs to function properly, which may also lead to death.

Glucose concentrations may be measured in a variety of tissues besides direct bloodstream sampling, which is the most representative quantity for clinical evaluation, but a difficult environment for sensor integration. While ‘finger-prick’ type sensors directly measure blood drops from a capillary injury, modern CGM methods which operate via transdermal measurements observe glucose concentration in the Interstitial Fluid (ISF) and that particular environment is also a good candidate for locating fully-implanted microfabricated sensors. The wireless data communication range for implant sensors is limited by RF energy absorption by the tissue thus imposing a depth limit for injection choices as well. The ISF glucose concentration does not track exactly with blood concentration but will rise and fall with a time lag behind changes occurring in the bloodstream [8,9]. Under stable conditions, a constant correction factor is possible. The lag in concentration has been measured to be between 7 and 17 minutes in a number of studies [10,11]. As this deviation from the blood concentration value is a common concern for new biosensors, a standard methodology of evaluating errors from the real-time blood glucose concentration was developed, now termed the Clarke Error Grid Analysis and its implementation was described in Clark et al [12].

The oxygenation of tissue follows a more complex dynamic than simple aqueous delivery in plasma. The metabolism has evolved solutions to the insufficient dissolution percentage of oxygen in body-temperature water. Hemoglobin in the blood functions with a sigmoidal affinity to oxygen such that in high concentration regions (as in the lungs) it will bind and in low concentration regions it will debind (as in the extremities). Thus, a large portion of available oxygen in the body is chemically bound and is freed upon need. In general, interstitial oxygenation will be at half of the concentration or less of a typical vitro solution. Water in dry 25C air sees an O₂ partial pressure of 160 Torr, which, when determined by dissolution tables [13] predicts **256.9μM** as the dissolved molarity, while arterial blood has an effective partial pressure of 100 Torr (@37C) converting to **~138μM** which can drop in poorly oxygenated areas to 40 Torr as observed in venous blood at(@37C) giving **55μM**. Overall the %vol of oxygen drops from 21% in atmosphere down by a factor of 4, to 5% or less in peripheral tissues.

As described above, PBS is the saline solution chosen as buffer solution to replicate effects of the body’s natural bicarbonate buffer system. The pH is maintained at 7.4 despite addition or subtraction of H⁺ due to chemical reactions,

which is crucial to maintaining enzyme function rates. The salinity of 1x PBS is also designed to be compatible with human cells and replicate typical in vivo ionic strength. This understanding of the various analyte parameters is crucial to both the sensor design and simulating behavior that will be discussed in the next chapter.

3.3 Tissue Response Concerns

The foreign-body capsule (FBC) development which impacts many biosensor technologies has been observed for as long as medical experts have examined tissue injuries and is generally very advantageous for survival from physical traumas. In a natural setting without the ability to surgically remove foreign bodies the encapsulation protects the body from poisonous materials or toxins that may have been present [14]. This creates a challenge for modern medicine where we seek to repair and improve the function of human tissues with materials that are not native to the body.

Besides the desired analytes there are a wide variety of other molecules arriving to the in vivo sensor surface to contend with. In addition to the normally distributed nutrients in a living system there will be dedicated molecules and systems in place to deal with foreign entities, like our biosensor. Tissue inflammation caused by the initial implant injury and the foreign body response (FBR) due to its continued presence will onset within an hour for the former and within a day for the latter. The FBR results in proteins and cells surrounding the device in a 10-100 micron thick layer within days [15], creating an analyte transfer barrier [16]. Increased cellular activity at the surface also consumes our particular analytes of interest (glucose and oxygen) for their own function [17]. As interest in bioimplants climbed since the 1980s many branches of approach have been followed to create anti-fouling coatings that behave more compatibly with the body [18]. They seek to reduce the fibrous protein and cellular growth at the surface so they may maintain the desired analyte flux to calibratable levels. Overall, the extent of FBR has been observed to be highly determined by the extent of initial tissue damage [19] which drives the focus of this work to push glucose sensors to smaller total footprints in the form of CMOS devices. According to literature, FBR is today the dominant mode of failure observed as many other aspects of glucose sensor functionality have found workable solutions [18].

The particular steps in the FBR process include initial coverage by proteins like fibrin that cause a layer to form over the object and provide a skeleton for additional molecular response. Leukocytes carried by the bloodstream, primarily

phagocytes such as neutrophils and macrophages, which harbor mechanisms to chemically attack foreign bodies and/or engulf and ingest bodies are recruited by chemical signaling to the injury site. Communication from and between macrophages (via inflammation markers like cytokines) prompts the increased action of fibroblasts to synthesize collagen and subsequently secrete it into the extracellular space as final restabilization of the injury. Vaddiraju et al [18] provides visualization of the steps. Some research approaches add drugs or proteins to the surface preimplantation that lower signaling for the inflammatory response. [18]

Glucose availability is observed to fluctuate during the first week of implantation as the acute response rises and falls [20], but fibrotic encapsulation that ends all flux has always been the inescapable end result [21, 22]. Another suggested glucose oscillation source is the generation of new capillaries post-implant [23] which may be desired or specifically sought (via growth factor [VEGF] addition) but must be accounted for in calibration expectations over the first few days. An understanding of all of these effects and their progression are necessary to extrapolate causes of sensor failure during certain time spans when moving to in vivo study and motivates construction choices during in vitro testing.

3.4 Sensor Fouling and Immobilizations

The FBR has many chemical effects beyond the diffusion mechanics concerns described above such as dissolution and passivation of sensor components. Failure of electrical or mechanical aspects of the biosensors are often seen to precede the failure of the enzyme molecules, but the latter must still be considered [17,23]. Damage is eventually observed on protective coatings that then leads to dysfunction of the sensor [24,25] such as allowing proteases or protein inhibitor molecules access to the enzyme layer. Incorporating an excess of enzyme molecules during fabrication is a common design element to decrease sensitivity to enzyme loss [17]. Other component failures include passivation of the electrode metal surface or disconnection of the layers such as separation of the electrode from the electronics or separation of the enzyme from the surface [26]. Passivation may occur as small molecules become adhered to the electrode surface thus decreasing the active surface area for target redox reactions [27]. As mentioned previously, strategies that operate at lower voltages may also slow down the collection of passivating molecules at the electrode. [28]

Enzyme failure may occur due to conformation damage, active site interference, cofactor loss or adherence failure. [26]. Immobilization methods are

optimized to prevent both the long term occurrence of these problems and their occurrence during initial fabrication. The protective coating procedure may damage the top regions of the enzyme layer so achieving high immobilization survival efficiencies allows more flexible design. Various strategies of enzyme deposition are currently employed, such as adsorption (depositing enzymes directly to the surface by dipping [26]), covalent or affinity linking [29], polymer embedment (as in early CA YSI devices), or as employed in this work, addition of cross-linkers. Immobilization layers may also provide filtering of macromolecules via constrictions. The choice of glutaraldehyde as the immobilization layer in this work will be expanded upon in the fabrication chapters.

3.5 Sensor Coatings

Development of outer coatings that inhibit or retard protein adhesion have been the primary strategy to decrease the pace of biofouling [17]. A variety of materials have been explored such as polycarbonate (PC) [30], polyurethane [31], Nafion [32], chitosan [33] and more with varying degrees of success. These layers may behave as biomimics as with chitosan or take advantage of polymer groups that prevent protein adhesion, as in PEO/PEG which has a highly hydrophilic surface [17].

The success of the YSI device is based on their implementation of PC with the intention to lower glucose flux to match O_2 availability. As O_2 is the smaller molecule, this is a more surmountable challenge than the inverse situation. In addition, lowering the glucose flux eases the requirements on construction of the GOx layer, since a smaller portion of functioning enzyme post-fabrication is necessary. The large external concentration is scaled to a lower internal concentration to which the enzyme can still provide linear response [8]. Common flux reductions are on the order of 10-100x, which enable fabricated layers with low K_M to still function with external concentrations much larger than their available K_M . Biosensors are then characterized by their overall K_M performance with their barrier layer. The upper bounds on the restrictiveness of this layer comes from either bringing the concentration below the electrode limit of detection or increasing the time delay too far from current bloodstream concentration which is caused by the decreased diffusion rates. Second and third generation glucose sensors without oxygen dependence for the redox cycle only need the glucose flux limiting behavior rather than differential diffusion simplifying their construction. Utilizing the simplicity of the diffusion equation across a uniform medium we can define the

permeability of a membrane layer as $P=KDdx$, which is linear with K , the partition coefficient of the species, D , the diffusion coefficient for the species, and dx the thickness of the layer [26]. Barrier layer thickness control will be further explored during later description of device fabrication.

3.6 Interference Concerns

Besides desired analyte and undesired immune response molecule flux control, interferent screening is another essential aspect of barrier layers. Biological fluids contain a number of oxidizable acids, oxidizable bases, electroactive metabolites, and proteins capable of passivating the electrode [26]. Examples of dedicated tools to counter these issues are perfluorinated sulfonated membranes termed Nafion, which have been observed to be biocompatible while exhibiting rejection of anionic molecules and cellulose acetate (CA) which can be used to reject acetaminophen, an electrochemically active compound. A more active approach has been employed by Heller et al [34] by depositing layers containing Horseradish Peroxidase and Lactate Oxidase which oxidizes interference molecules with cyclical formation of H_2O_2 . A list of expected interferents has been developed by the FDA and their respective in vivo concentrations can be found in Heller et al [8]. Strategies to mitigate interference and the other aforementioned concerns have involved multilayer approaches combining different types of coatings for different functions. They may be adaptable to planar device geometries, but this work will focus on a novel microfabrication-originating coating approach to address these concerns.

References:

[1] D. Voet, J. Voet and C. Pratt, *Fundamentals of biochemistry*. 1998.

[2] J. Harris, C. Reyes and G. Lopez, "Common Causes of Glucose Oxidase Instability in In Vivo Biosensing: A Brief Review", *Journal of Diabetes Science and Technology*, vol. 7, no. 4, pp. 1030-1038, 2013. Available: 10.1177/193229681300700428.

- [3] B. Wagner, J. Witmer, T. van't Erve and G. Buettner, "An assay for the rate of removal of extracellular hydrogen peroxide by cells", *Redox Biology*, vol. 1, no. 1, pp. 210-217, 2013. Available: 10.1016/j.redox.2013.01.011.
- [4] L. Michaelis and M. Menten, "Kinetics of Invertase Action", *Biochemische Zeitschrift*, vol. 49, pp. 333-69, 1913.
- [5] Q. Gibson, B. Swoboda and V. Massey, "Kinetics and Mechanism of Action of Glucose Oxidase", *The Journal of Biological Chemistry*, vol. 239, no. 11, pp. 3927-3934, 1964.
- [6] American Diabetes Association, "Screening for Type 2 Diabetes", *Clinical Diabetes*, vol. 18, no. 2, pp. S20-23, 2019.
- [7] D. Wasserman, "Four grams of glucose", *American Journal of Physiology-Endocrinology and Metabolism*, vol. 296, no. 1, pp. E11-E21, 2009. Available: 10.1152/ajpendo.90563.2008.
- [8] A. Heller and B. Feldman, "Electrochemical Glucose Sensors and Their Applications in Diabetes Management", *Chemical Reviews*, vol. 108, no. 7, pp. 2482-2505, 2008. Available: 10.1021/cr068069y.
- [9] E. Cengiz and W. Tamborlane, "A Tale of Two Compartments: Interstitial Versus Blood Glucose Monitoring", *Diabetes Technology & Therapeutics*, vol. 11, no. 1, pp. S-11-S-16, 2009. Available: 10.1089/dia.2009.0002.
- [10] M. Boyne, D. Silver, J. Kaplan and C. Saudek, "Timing of Changes in Interstitial and Venous Blood Glucose Measured With a Continuous Subcutaneous Glucose Sensor", *Diabetes*, vol. 52, no. 11, pp. 2790-2794, 2003. Available: 10.2337/diabetes.52.11.2790.
- [11] B. Feldman, R. Brazg, S. Schwartz and R. Weinstein, "A Continuous Glucose Sensor Based on Wired Enzyme™ Technology - Results from a 3-Day Trial in Patients with Type 1 Diabetes", *Diabetes Technology & Therapeutics*, vol. 5, no. 5, pp. 769-779, 2003. Available: 10.1089/152091503322526978.

- [12] W. Clarke, D. Cox, L. Gonder-Frederick, W. Carter and S. Pohl, "Evaluating Clinical Accuracy of Systems for Self-Monitoring of Blood Glucose", *Diabetes Care*, vol. 10, no. 5, pp. 622-628, 1987. Available: 10.2337/diacare.10.5.622.
- [13] USGS, "National Field Manual for the Collection of Water-Quality Data Chapter A6. Field Measurements", 1998.
- [14] W. Ward, "A Review of the Foreign-body Response to Subcutaneously-implanted Devices: The Role of Macrophages and Cytokines in Biofouling and Fibrosis", *Journal of Diabetes Science and Technology*, vol. 2, no. 5, pp. 768-777, 2008. Available: 10.1177/193229680800200504.
- [15] Y. Onuki, U. Bhardwaj, F. Papadimitrakopoulos and D. Burgess, "A Review of the Biocompatibility of Implantable Devices: Current Challenges to Overcome Foreign Body Response", *Journal of Diabetes Science and Technology*, vol. 2, no. 6, pp. 1003-1015, 2008. Available: 10.1177/193229680800200610.
- [16] N. Wisniewski, F. Moussy and W. Reichert, "Characterization of implantable biosensor membrane biofouling", *Fresenius' Journal of Analytical Chemistry*, vol. 366, no. 6-7, pp. 611-621, 2000. Available: 10.1007/s002160051556.
- [17] G. Wilson and R. Gifford, "Biosensors for real-time in vivo measurements", *Biosensors and Bioelectronics*, vol. 20, no. 12, pp. 2388-2403, 2005. Available: 10.1016/j.bios.2004.12.003.
- [18] S. Vaddiraju, I. Tomazos, D. Burgess, F. Jain and F. Papadimitrakopoulos, "Emerging synergy between nanotechnology and implantable biosensors: A review", *Biosensors and Bioelectronics*, vol. 25, no. 7, pp. 1553-1565, 2010. Available: 10.1016/j.bios.2009.12.001.
- [19] P. Kvist et al., "Biocompatibility of an Enzyme-Based, Electrochemical Glucose Sensor for Short-Term Implantation in the Subcutis", *Diabetes Technology & Therapeutics*, vol. 8, no. 5, pp. 546-559, 2006. Available: 10.1089/dia.2006.8.546.
- [20] H. Lutgers, "Microdialysis measurement of glucose in subcutaneous adipose tissue up to three weeks in Type 1 diabetic patients", *The Netherlands Journal of*

Medicine, vol. 57, no. 1, pp. 7-12, 2000. Available: 10.1016/s0300-2977(00)00022-x.

[21] H. Clark, T. Barbari, K. Stump and G. Rao, "Histologic evaluation of the inflammatory response around implanted hollow fiber membranes", *Journal of Biomedical Materials Research*, vol. 52, no. 1, pp. 183-192, 2000. Available: 10.1002/1097-4636(200010)52:1

[22] A. Sharkawy, B. Klitzman, G. Truskey and W. Reichert, "Engineering the tissue which encapsulates subcutaneous implants. II. Plasma-tissue exchange properties", *Journal of Biomedical Materials Research*, vol. 40, no. 4, pp. 586-597, 1998. Available: 10.1002/(sici)1097-4636(19980615)

[23] S. Updike, M. Shults, R. Rhodes, B. Gilligan, J. Luebow and D. Heimborg, "Enzymatic Glucose Sensors", *ASAIO Journal*, vol. 40, no. 2, pp. 157-163, 1994. Available: 10.1097/00002480-199440020-00007.

[24] J. Anderson et al., "Recent advances in biomedical polyurethane biostability and biodegradation", *Polymer International*, vol. 46, no. 3, pp. 163-171, 1998. Available: 10.1002/(sici)1097-0126(199807)

[25] R. Mercado and F. Moussy, "In vitro and in vivo mineralization of Nafion membrane used for implantable glucose sensors", *Biosensors and Bioelectronics*, vol. 13, no. 2, pp. 133-145, 1998. Available: 10.1016/s0956-5663(97)00112-7.

[26] G. Rocchitta et al., "Enzyme Biosensors for Biomedical Applications: Strategies for Safeguarding Analytical Performances in Biological Fluids", *Sensors*, vol. 16, no. 6, p. 780, 2016. Available: 10.3390/s16060780.

[27] N. Wisniewski and M. Reichert, "Methods for reducing biosensor membrane biofouling", *Colloids and Surfaces B: Biointerfaces*, vol. 18, no. 3-4, pp. 197-219, 2000. Available: 10.1016/s0927-7765(99)00148-4.

[28] A. Curulli and G. Palleschi, "Construction and application of highly selectively sensors and biosensors using non-conducting electropolymerized films", in *Proceedings of the 2nd Workshop on Chemical Sensors and Biosensors*, Rome, Italy, 2000.

[29] A. Heller, "Electrical wiring of redox enzymes", *Accounts of Chemical Research*, vol. 23, no. 5, pp. 128-134, 1990. Available: 10.1021/ar00173a002.

[30] M. Schlesinger, *Applications of Electrochemistry in Medicine*, 1st ed. Springer US, 2013.

[31] D. Bindra et al., "Design and in vitro studies of a needle-type glucose sensor for subcutaneous monitoring", *Analytical Chemistry*, vol. 63, no. 17, pp. 1692-1696, 1991. Available: 10.1021/ac00017a008.

[32] D. Harrison, R. Turner and H. Baltes, "Characterization of perfluorosulfonic acid polymer coated enzyme electrodes and a miniaturized integrated potentiostat for glucose analysis in whole blood", *Analytical Chemistry*, vol. 60, no. 19, pp. 2002-2007, 1988. Available: 10.1021/ac00170a003.

[33] Y. Zhang, Y. Li, W. Wu, Y. Jiang and B. Hu, "Chitosan coated on the layers' glucose oxidase immobilized on cysteamine/Au electrode for use as glucose biosensor", *Biosensors and Bioelectronics*, vol. 60, pp. 271-276, 2014. Available: 10.1016/j.bios.2014.04.035.

[34] E. Csoeregi et al., "Design, Characterization, and One-Point in vivo Calibration of a Subcutaneously Implanted Glucose Electrode", *Analytical Chemistry*, vol. 66, no. 19, pp. 3131-3138, 1994. Available: 10.1021/ac00091a022.

Chapter 4 Modeling Sensor Behavior

Amperometric sensors with immobilized enzyme layers above the electrode surface are subject to a series of interdependent diffusion processes which complicate the description and prediction of their device performance. An evaluation will be described here, made via numerical simulations of the combined diffusion and enzymatic kinetics of a glucose oxidase sensor, in a 1-dimensional approximation built in COMSOL Multiphysics. Prior explorations have been made for diffusion kinetics of such sensors for single substrate concerns [1,2,3], non-mediated type sensors [4], and rarely for full bi-substrate behavior [5]. But our primary concern in this evaluation is motivated by our overall goal of applying microfabrication techniques to sensor construction. The goal is to use accurately formed and thinner than previously fielded enzyme layers to improve glucose sensor performance, and we would like to develop an intuitive understanding for their behavior. As such, the primary sweep parameter will be the thickness of the immobilized enzyme layer. A balance forms between glucose and oxygen consumption by the enzyme, peroxide to oxygen conversion at the electrode, peroxide loss due to diffusion, and glucose and oxygen delivery from the bulk for a device in fluid equilibrium. The following plots are meant to highlight dynamics inherent to oxygen mediated sensors.

The overall behavior is as follows. H_2O_2 is generated within some volume of the immobilization layer but not uniformly due to the bulk diffusion gradient and following the bisubstrate kinetics described prior (equation 14). This layer will have lower diffusion coefficients for the species than the external solution in general and we will estimate them for purposes here to be 20% of bulk coefficients based on the work of Stroe-Blezen et al [6] which found a range of 19%-40% for their GA hydrogels. The generated H_2O_2 may be consumed at the electrode, lost to the bulk diffusion or decay. The rate of loss is based either on diffusion speeds away from the electrode and the half-life decay of H_2O_2 within each volume. This half life has been observed to be very short in cellular media [7], as low as 50ms, primarily driven by catalase and metal reactant such as iron. For comparison the expected diffusion time the opposite direction through a $5\mu\text{m}$ GA film is $(5\mu\text{m})^2/(D_{\text{film}}(\text{H}_2\text{O}_2)) \approx 87\text{ms}$. At the applied positive bias of the working electrode, the catalytic surface reaction rate for H_2O_2 on platinum is assumed to far exceeds other dynamics of the system [8] and can be approximated as instantaneous upon contact for our purposes. As described previously, the platinum- H_2O_2 reaction produces two electrons and returns O_2 to the solution.

Besides the diffusion lengths, the main variable controlled when choosing an immobilization layer thickness is the total moles of enzymes within the layer. The V_{\max} of a layer is thus sensitive to the fabrication dilution choices and the inactivation of enzyme during the fabrication process. For our purposes here, the enzyme density is maintained constant while the film thickness varies. The opposite situation favors thin layers even more strongly since the higher activity layer can rapidly stabilize and efficiently cycle. Another factor not considered during these simulations is the internal loss of peroxide while travelling through the film to the electrode, which also lead to benefits from thinner layer choices. This process is known to cause damage to both the GOx [9] and GA film, thus shortening the lifespan of the matrix and the sensor while lowering available signal. As visible in the lower plots, H_2O_2 will be primarily generated at the 'top' of the interface, and must travel through the full film length to transduce and be measured. This process will be the automatic behavior dominate when assuming the top immobilization regions were not damaged during fabrication, but would likely eventually become true as the enzyme layer is damaged over time from external causes. The overall picture gained from the simulations is that when H_2O_2 destruction is considered, as would occur in vivo, decreasing the layer thickness may benefit signal collections, while in vitro where H_2O_2 is able to accumulate would show no such behavior. The lower bound on layer thickness is eventually determined by the lack of sufficient enzyme to process a measurable amount of glucose.

Model Description:

The total simulation cell length 'L' is 1mm and the immobilization thicknesses 'LT' are varied from 20nm to 10 μ m. The kinetic values for GOx were sourced from the analysis of Gibson et al. [10] and we will assume a similar active enzyme dentistry for our purposes. In vitro test values of 10mM glucose and 260 μ mol oxygen are the species boundary input.

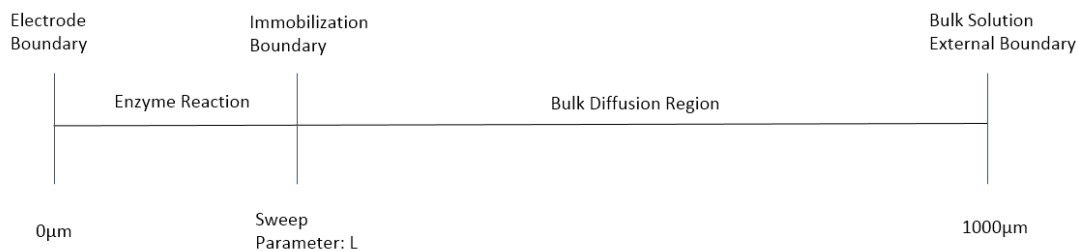


Figure 4.1 1D simulation cell schematic.

The right side boundary:

$$\begin{aligned}
 [O_2](t, L) &= 260 \mu\text{mol} \\
 [G](t, L) &= 10 \text{mmol} \\
 [H_2O_2](0, L) &= 0 \text{mol}
 \end{aligned}$$

The bulk source of the species is treated as constant concentration source, which is an approximation for in vivo or in vitro measurement situations but further specification may not yield any more information. The plots provided here assume analyte delivery at the outer boundary, but setting analyte boundary at the film surface does not have significant impact on the balancing behavior observed and described below.

The left side boundary is set as an electrode which runs the $H_2O_2 \rightarrow O_2 + 2e^-$ [M] reaction. A common approach to describe this boundary is simply as 0 concentration and calculating the resulting electrode current via the molar flux. We assume all H_2O_2 is consumed by the boundary which we control via the reaction speed k_0 . The electrode current is given per area as this is a 1D model. F is the Faraday Constant and $n=2$ for the electrons per H_2O_2 molecule. Thus the left boundary may be described as:

$$j = 2Fk_0[H_2O_2] = 2FD_{H_2O_2} \left. \frac{\partial[H_2O_2]}{\partial x} \right|_{x=0} \quad \text{with} \quad [H_2O_2](t, 0) = 0 \text{mol}$$

The film region behaves as such:

$$\begin{aligned}\frac{d[G]}{dt} + \nabla \cdot (-D_G \nabla[G]) &= -\frac{V_{\max}[G][O_2]}{K_{O_2}[G] + K_G[O_2] + [G][O_2]} \\ \frac{d[O_2]}{dt} + \nabla \cdot (-D_{O_2} \nabla[O_2]) &= -\frac{V_{\max}[G][O_2]}{K_{O_2}[G] + K_G[O_2] + [G][O_2]} \\ \frac{d[H_2O_2]}{dt} + \nabla \cdot (-D_{H_2O_2} \nabla[H_2O_2]) &= \frac{V_{\max}[G][O_2]}{K_{O_2}[G] + K_G[O_2] + [G][O_2]}\end{aligned}$$

The bulk region behaves as so with peroxide decay enabled:

$$\begin{aligned}\frac{d[H_2O_2]}{dt} + \nabla \cdot (-D_{H_2O_2} \nabla[H_2O_2]) &= -k_{H_2O_2}[H_2O_2] \\ \frac{d[O_2]}{dt} + \nabla \cdot (-D_{O_2} \nabla[O_2]) &= k_{H_2O_2}[H_2O_2]\end{aligned}$$

And as such with peroxide decay disabled:

$$\begin{aligned}\frac{d[O_2]}{dt} + \nabla \cdot (-D_{O_2} \nabla[O_2]) &= 0 \\ \frac{d[H_2O_2]}{dt} + \nabla \cdot (-D_{H_2O_2} \nabla[H_2O_2]) &= 0\end{aligned}$$

And glucose flow remains consistent in both conditions.

$$\frac{d[G]}{dt} + \nabla \cdot (-D_G \nabla[G]) = 0$$

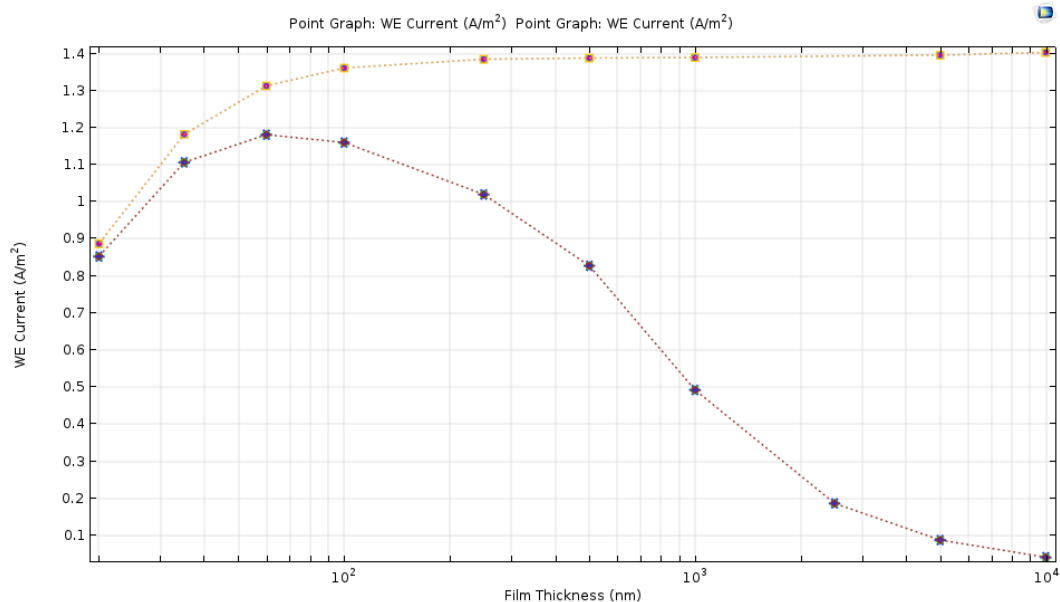
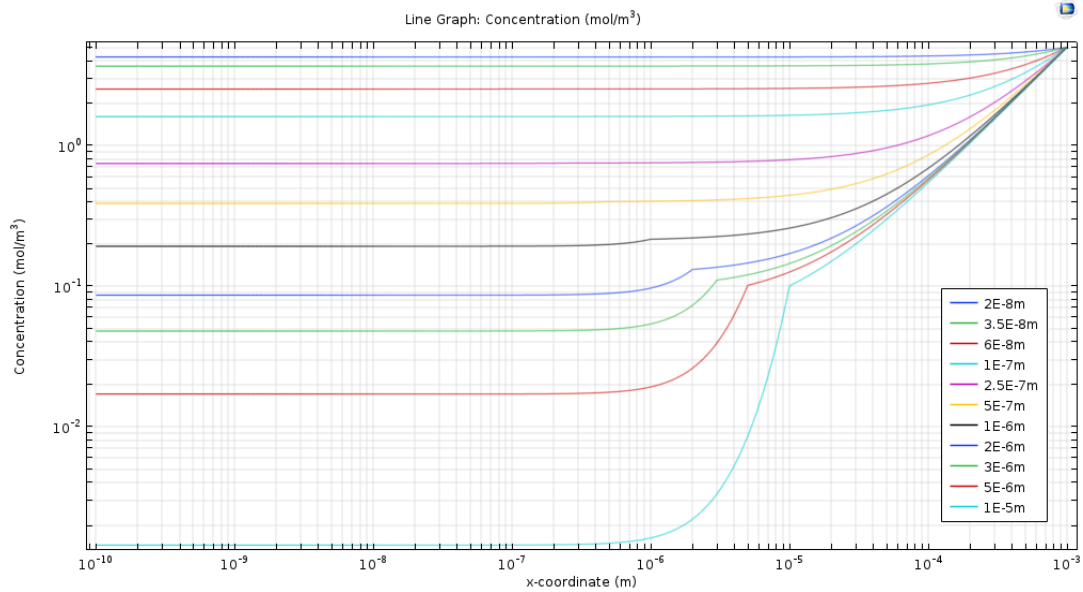


Figure 4.2 Current response to enzyme layer thickness. Each x-position represents a simulation performed with the corresponding immobilization layer thickness (purple) with in vivo considerations and (orange) with in vitro considerations

Immediately evident in Fig 4.2 is the optimal current response (purple) for thin layers when mediator decay is present. Meanwhile the in vitro current signal (orange) will eventually saturate as the enzyme layer itself saturates. The excess H_2O_2 raises the bulk H_2O_2 concentration as evident in the following plots which will also give a better understanding of the measurement behavior. The optimum thickness is highly dependent on V_{max} or rather the density and fabrication survival rate of the enzyme. The V_{max} utilized here, sourced from Gibson et al. performed their measurements with a $1.1e-5M$ enzyme concentration. For an immobilization layer the maximum enzyme density is approximately $((1 \text{ liter})/N_A) * ((1 \text{ liter})/(140\text{\AA} * 50\text{\AA} * 50\text{\AA})) \approx 0.5e-3M$, based on enzyme crystal dimensions. The actual density is further lowered by an at least 50% fraction of carrier protein and crosslinker and the functional enzyme post-fabrication is estimated in the 1-10% range. As such we choose to use Gibson's values directly for the enzyme parameters here and have observed variation to give nondramatic perturbations.

a.



b.

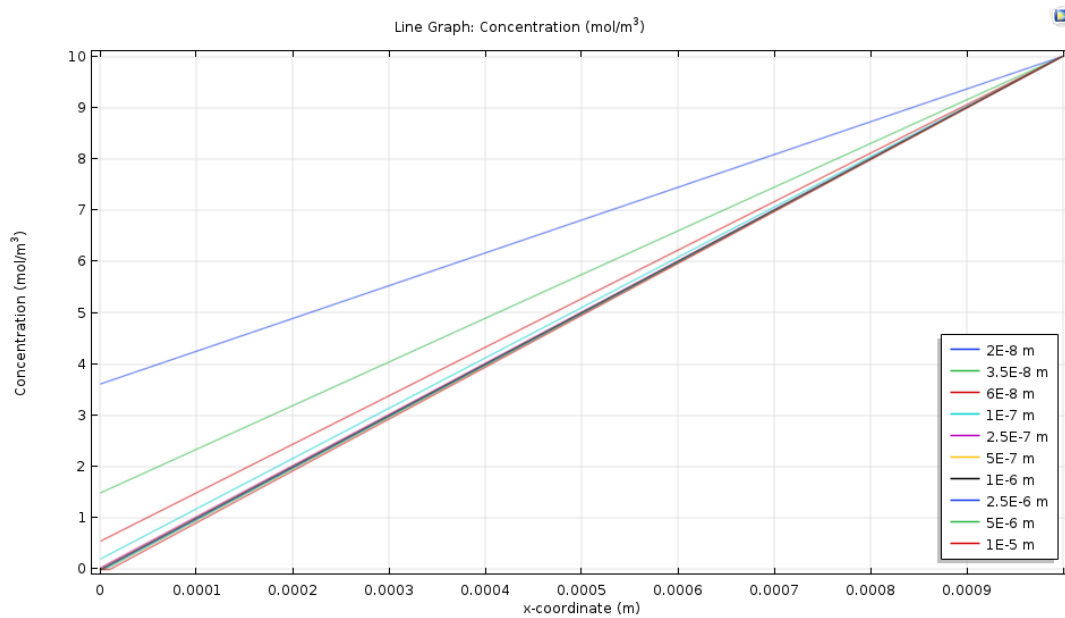
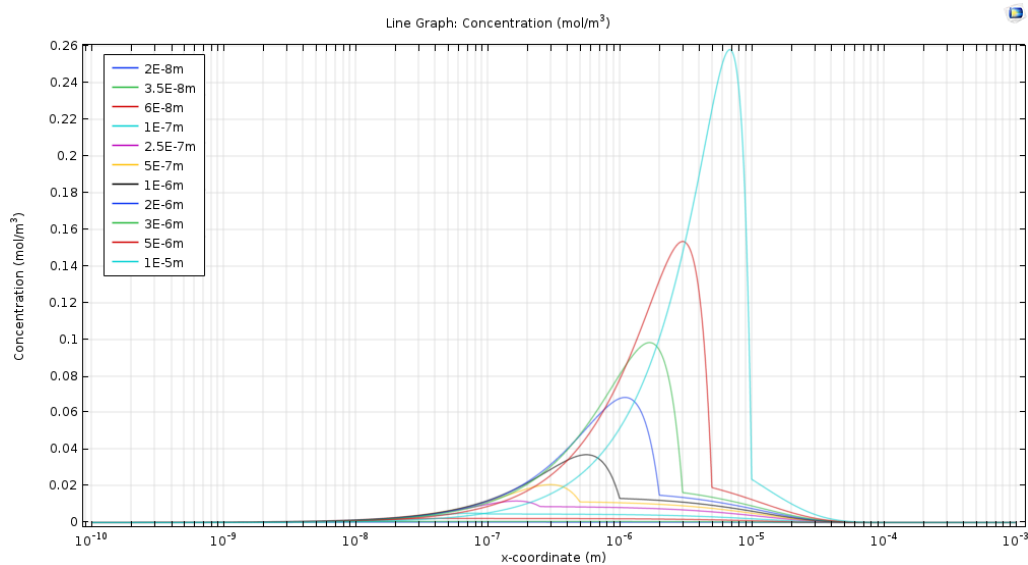


Figure 4.3 [G] vs. layer thickness. At sufficiently thin layers, glucose is not completely consumed at the surface. The log (a) and linear (b) forms are given for clarity of behavior.

a.



b.

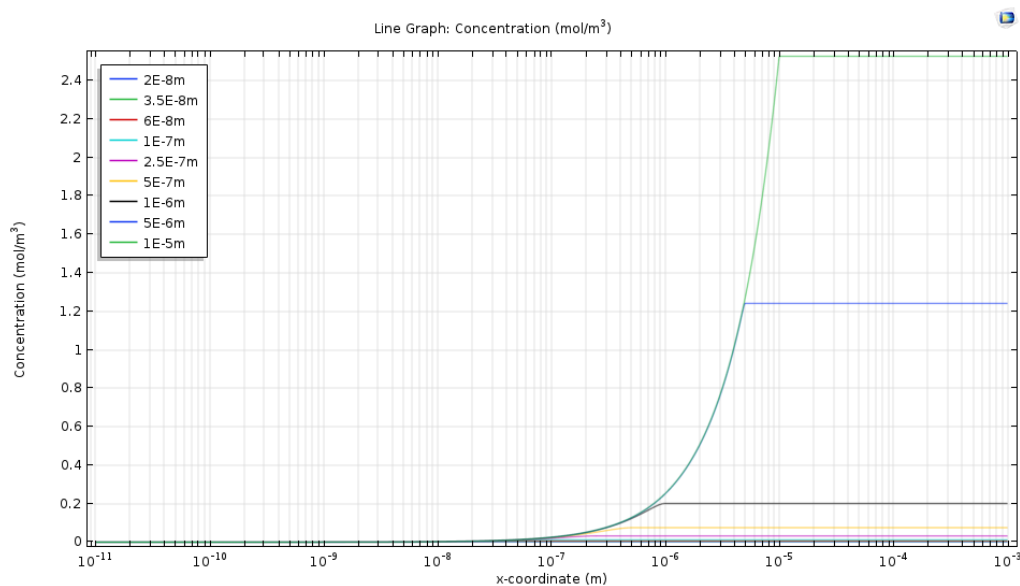
Figure 4.4 [H₂O₂] vs. layer thickness.

Fig 4.4a shows the formation of H₂O₂ near the ‘front’ boundary of the film. For thinner films an equilibrium is established with the electrode such that lower total H₂O₂ concentrations are formed which is beneficial in that it avoids oxidative damage to the film and oxidative stress to a cellular environment. H₂O₂ concentrations above 10μM can be considered stressful to cells and above 100μM

can become toxic [11]. Fig 4.4b shows the control behavior in vitro where the measurement vessel will be filled with peroxide over time.

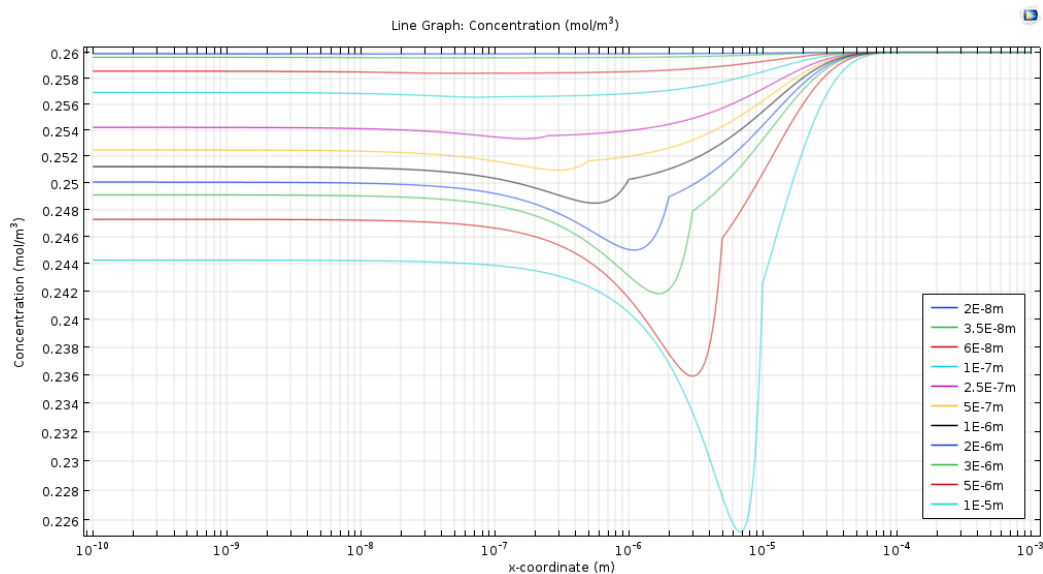


Figure 4.5 [O₂] vs. layer thickness.

For sufficiently thick layers, as seen in Fig 4.5, O₂ will deplete at the ‘front’ surface since it is both further from electrode reaction recycling and more total reactions occur in the larger enzyme volume. Another factor to consider for sensor stability purposes is, as can be seen in the plot, the available surface O₂ concentration will decrease due to the higher enzyme reaction amounts which would in turn affect equilibrium voltage of the platinum. In poorly oxygenated conditions, the slowdown of the enzyme kinetics is expected to become more apparent.

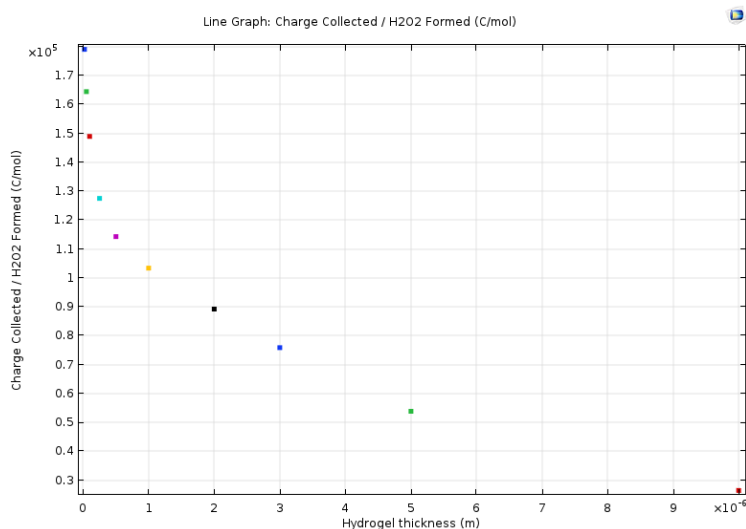


Figure 4.6 Current produced per mole of H₂O₂ generated in film.

The enzyme product transduction efficiency is evident in Fig 4.6. A larger portion of H₂O₂ in thin layers is measured as current although a balance must be chosen such that sufficient enzyme is present to provide overall signal.

There are many other parameters to further explore, but this study is focused on the nature of geometric layer thickness control, and to include all other parametric sweeps would require many additional assumptions about the nature of the in vivo environment. The behaviors explored here were also evaluated with 2D-symmetric and 3D models to verify their relevance to realistic geometries, but due to slow solution convergence speeds and additional assumptions required, we present 1D predictions here, following the standard approach in literature. Unfortunately, shrinking devices through microfabrication begins to violate the 1D diffusion approximation, and the concentric geometry of electrodes employed in fabrication work creates additional variables that will have to be elucidated in a future study. Filtering membranes, as described in the previous chapter, are a standard solution to in vivo measurement but they are not considered here, as again they require more assumptions and obscure the specific study of thickness effects sought after.

	In Film	In Bulk	External
D (H ₂ O ₂)	0.2*1.43e-9 m ² /s [6]	1.43e-9 m ² /s [6]	
D (O ₂)	0.2*1.93e-9 m ² /s [6]	1.93e-9 m ² /s [6]	
D (Glucose)	0.2*0.72e-9 m ² /s [6]	0.72e-9 m ² /s [6]	
[Glucose]			10mM
[O ₂]			260μM
Layer Thickness	LT = 20nm to 10μm	1000μm - LT	
H ₂ O ₂ half life	None	None (in vitro) 50ms (in vivo) [9]	
K _G	110mM [10]	0	
K _{O₂}	480μM [10]	0	
V _{max}	1150mol/s [10]	0	

Table 4.1 Summary of COMSOL diffusion and enzyme simulation parameters.

References:

- [1] O. AS, "Mathematical Modelling of an Enzyme-Based Biosensor", *International Journal of Biosensors & Bioelectronics*, vol. 3, no. 2, 2017. Available: 10.15406/ijbsbe.2017.03.00062.
- [2] A. Cambiaso et al., "Modelling and simulation of a diffusion limited glucose biosensor", *Sensors and Actuators B: Chemical*, vol. 33, no. 1-3, pp. 203-207, 1996. Available: 10.1016/0925-4005(96)80099-2.
- [3] L. Mell and J. Maloy, "Model for the amperometric enzyme electrode obtained through digital simulation and applied to the immobilized glucose oxidase system", *Analytical Chemistry*, vol. 47, no. 2, pp. 299-307, 1975. Available: 10.1021/ac60352a006.

- [4] M. Puida, J. Dabulytė-Bagdonavičienė, F. Ivanauskas, V. Razumas, J. Razumienė and I. Šakinytė, "Glucose sensor based on nanostructured carbon electrode with immobilized PQQ-containing glucose dehydrogenase: Construction, experimental study and mathematical modeling", *Nonlinear Analysis: Modelling and Control*, vol. 21, no. 5, pp. 702-715, 2016. Available: 10.15388/na.2016.5.9.
- [5] J. Leypoldt and D. Gough, "Model of a two-substrate enzyme electrode for glucose", *Analytical Chemistry*, vol. 56, no. 14, pp. 2896-2904, 1984. Available: 10.1021/ac00278a063.
- [6] S. van Stroe-Biezen, F. Everaerts, L. Janssen and R. Tacken, "Diffusion coefficients of oxygen, hydrogen peroxide and glucose in a hydrogel", *Analytica Chimica Acta*, vol. 273, no. 1-2, pp. 553-560, 1993. Available: 10.1016/0003-2670(93)80202-v.
- [7] B. Wagner, J. Witmer, T. van't Erve and G. Buettner, "An assay for the rate of removal of extracellular hydrogen peroxide by cells", *Redox Biology*, vol. 1, no. 1, pp. 210-217, 2013. Available: 10.1016/j.redox.2013.01.011.
- [8] S. Hall, E. Khudaish and A. Hart, "Electrochemical oxidation of hydrogen peroxide at platinum electrodes. Part 1. An adsorption-controlled mechanism", *Electrochimica Acta*, vol. 43, no. 5-6, pp. 579-588, 1998. Available: 10.1016/s0013-4686(97)00125-4.
- [9] J. Harris, C. Reyes and G. Lopez, "Common Causes of Glucose Oxidase Instability in In Vivo Biosensing: A Brief Review", *Journal of Diabetes Science and Technology*, vol. 7, no. 4, pp. 1030-1038, 2013. Available: 10.1177/193229681300700428.
- [10] Q. Gibson, B. Swoboda and V. Massey, "Kinetics and Mechanism of Action of Glucose Oxidase", *The Journal of Biological Chemistry*, vol. 239, no. 11, pp. 3927-3934, 1964.
- [11] H. Forman, A. Bernardo and K. Davies, "What is the concentration of hydrogen peroxide in blood and plasma?", *Archives of Biochemistry and Biophysics*, vol. 603, pp. 48-53, 2016. Available: 10.1016/j.abb.2016.05.005.

Chapter 5 Wafer Spincoated GOx Sensors

5.1 Overview

A 3-electrode planar arrangement of platinum electrodes was selected and arrayed across a wafer design as the basis for the microfabricated glucose sensor measurement. The non-passivated area of the electrode sets was chosen to be $500\mu\text{m} \times 500\mu\text{m}$ to mimic the available area on a future diced CMOS device. These electrodes are connected via insulated traces to larger probe pads approximately 2cm away. This allowed construction of a jig which delivers fluids to certain portions of the wafer surface while keeping dry electrical connections on other portions. The particular geometries are further described and given in the figures below.

The platinum electrode system is a reasonably well understood microfabrication task which we will details consider for below. But the new goals of wafer-scale biosensor fabrication led us to improve upon spincoat enzyme deposition methods. This fabrication process, measurement process, and data analysis follows.

5.2 Platinum Fabrication

Platinum was chosen as the primary electrode materials for the reasons discussed in Chapter 2. The primary deposition methods were electron beam evaporation and magnetron sputtering. Electron beam (e-beam) evaporation is performed in a high vacuum environment (10^{-6} Torr) with a 'pocket' source of evaporated platinum being sprayed towards the aforementioned wafer samples. E-beam evaporation provides high uniformity in the deposition thickness, particularly when the sample stage is rotated and all samples are equidistant from the source. Platinum's particularly high melting point makes it preferable to deposit with an e-beam process over a cheaper resistive thermal evaporation process because the operating temperatures are near the limits of the filament type sources used in thermal evaporation while in e-beam evaporation a balance is created between electron beam energy delivery to melt/evaporate the source and a water cooling system that protects the source-containing hearth and leads to greater purity.

Sputtering utilizes a DC or RF plasma field of argon gas in the ~ 10 mTorr range to bombard a source target and spray platinum towards the wafers. Due to the higher pressure of operation and the larger area of the target, the mean free path of source atoms is reduced and the velocity distribution smooths out away from line-of-

sight. This provides conformal deposition of source material onto the sample, which is preferable when 3-dimensional structures must be coated as described later, but not preferable when trying to 'shadow' depositions.

It was found that great care in the treatment of the platinum surface must be taken to not degrade its electrochemical properties. Our desire is to make final samples that need little calibration or cleaning as the need to do so adds cost to the fabrication process and complexity to the interface electronics. As such, plasma cleaning steps were avoided, or any processing besides directly applying the enzyme layer onto recently deposited platinum. During the deposition process a highly porous grain arrangement is grown, each with individual crystal orientations and exposed surfaces. The variety and lack of passivation of this platinum was found to enable better H_2O_2 consumption per surface area than coatings that were otherwise handled. AFMs are provided in Fig 5.1a-c of a comparison of newly deposited platinum and platinum that was used as an etch stop in an SF_6 -based oxide etch. Altering the grain structure of the platinum via introduction of contamination gasses was also explored and the resulting structure of the PtO formed in 10% oxygen is shown in Fig 5.1d

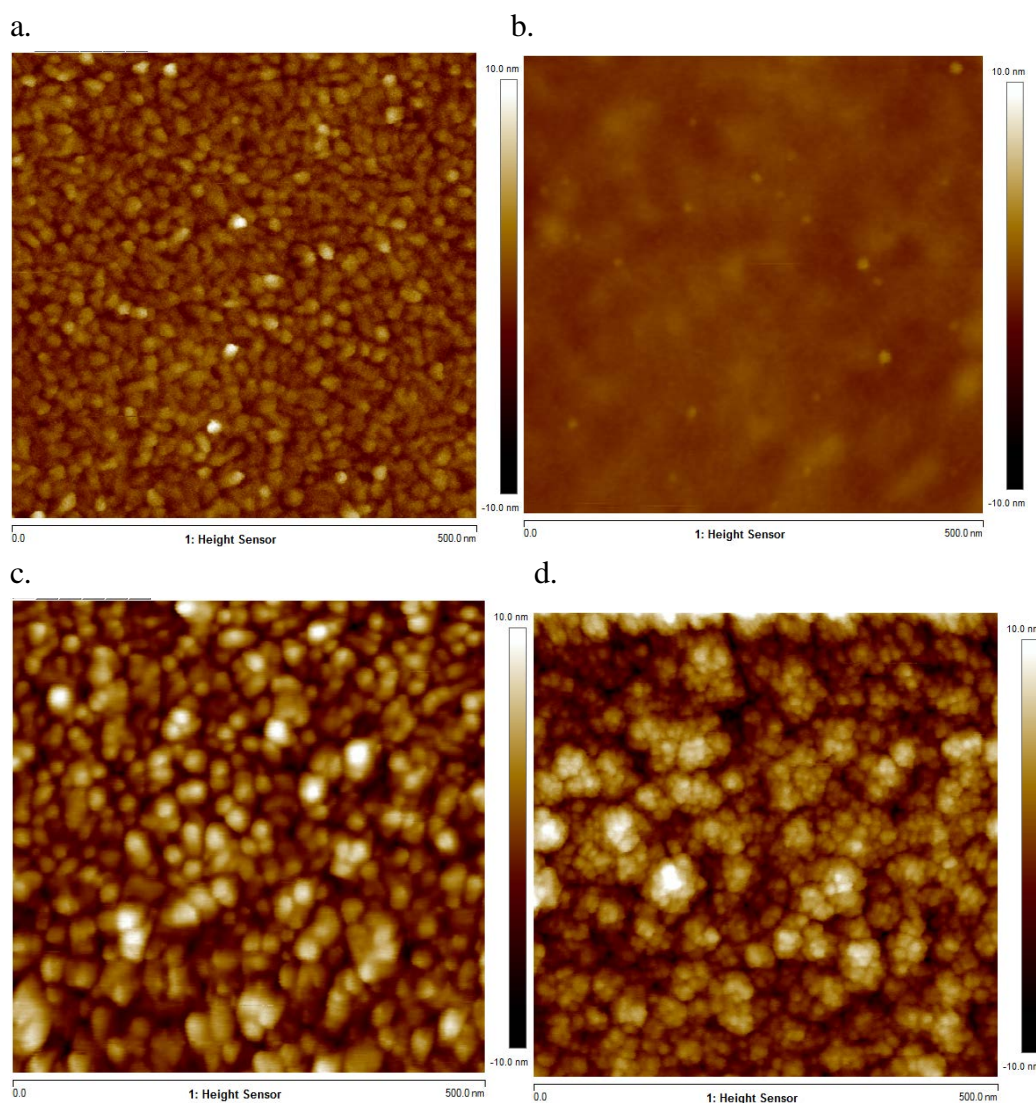


Figure 5.1 AFM of electrode surfaces (a) Evaporated platinum; (b) Evaporated platinum used as an etch stop; (c) Sputtered platinum; (d) Sputtered platinum oxide.

Platinum evaporation was performed below 2×10^{-6} Torr, with high purity 99.99% sources. An adhesion layer of 10nm Ti deposited at 0.5 \AA/s was typically used, followed by a 100nm Pt deposition at 1 \AA/s . Sputter deposition was performed at 0.5×10^{-3} Torr after reaching a base pressure of 5×10^{-6} Torr with a 99.99% platinum target, and 50sccm delivery of 99.99% purity argon.

Variety in grain structure from the different mechanisms of deposition are immediately evident. Evaporated grains were more densely packed and 10-20nm in size while sputtering produced greater variety of structure. Sputtering platinum in

the presence of oxygen had the desired effect to increase the available surface area, and is expected to have formed a high percentage of PtO on its surface versus Pt. Higher surface area should permit higher surface chemical oxidation reaction rates until the diffusion field reaches significantly higher than the surface in the fluid. PtO may be able to function as a more stable electrode in certain environments but this was not explored. Fig 5.2. shows the difference in crystallinity between platinum sputtered without and in the presence of oxygen, further highlighting the amorphous nature of the grown structures.

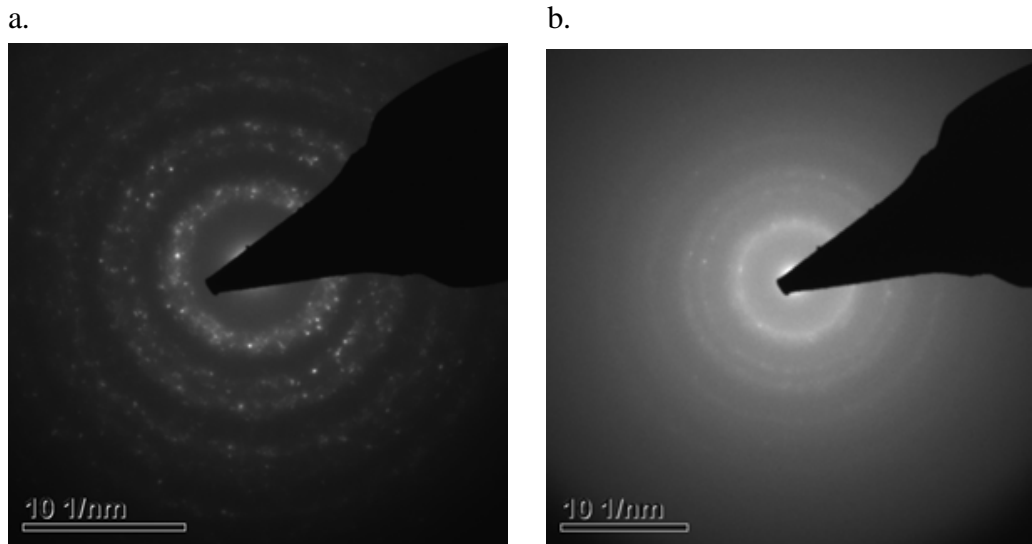


Figure 5.2 TEM diffraction patterns of (a) Pt and (b) PtO

Increasing the surface area of exposed platinum by increasing the surface area of the underlying substrate was also explored and data from such devices is collated in prior published work [1]. Nanopillar structures were fabricated using pseudo-Bosch [2] etching of crystalline silicon wafers to form high aspect ratio structures from aluminum oxide masks. The pillars were subsequently thermally oxidized to electrically isolate the substrate from the electrodes, followed by platinum sputtering to conformally coat the pillars (see Fig 5.3).

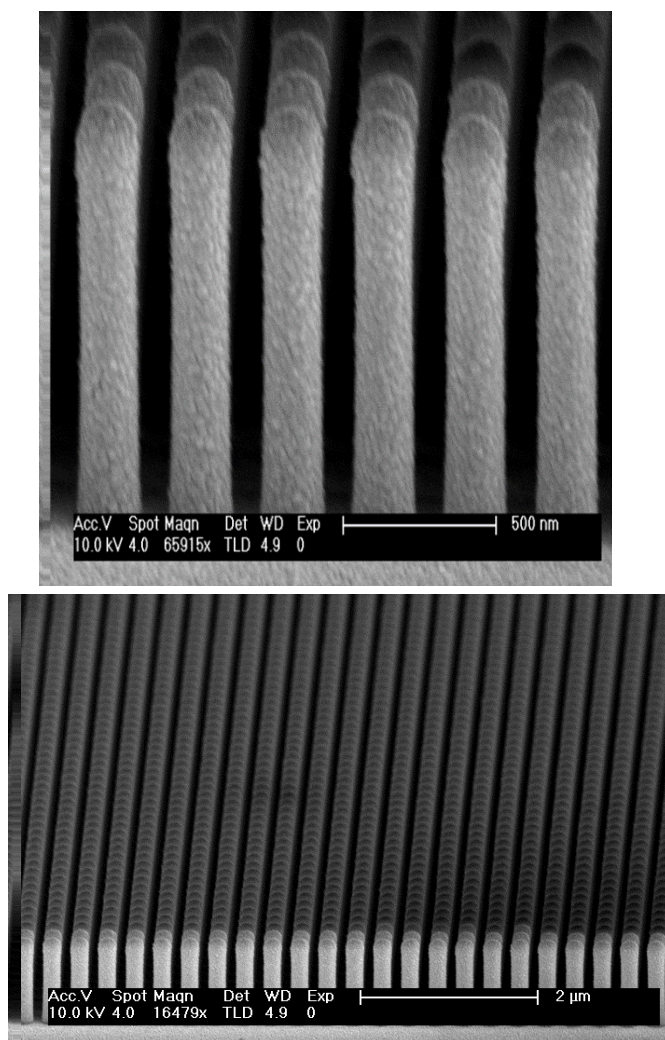


Figure 5.3 Pt-coated silicon dioxide nanopillars

Ag/AgCl reference electrodes were also built in plane in a similar fashion. They were typically electron beam evaporated, in a stack of: 10nm Ti as an adhesion layer, 10nm Pt to protect the Ag from the Ti diffusion, and 300nm of Ag. The Ag was then either chloridized in plasma or FeCl before a significant oxidation layer could form. An example electrode is visible in Fig 5.4 and with an SEM in Fig 5.5.

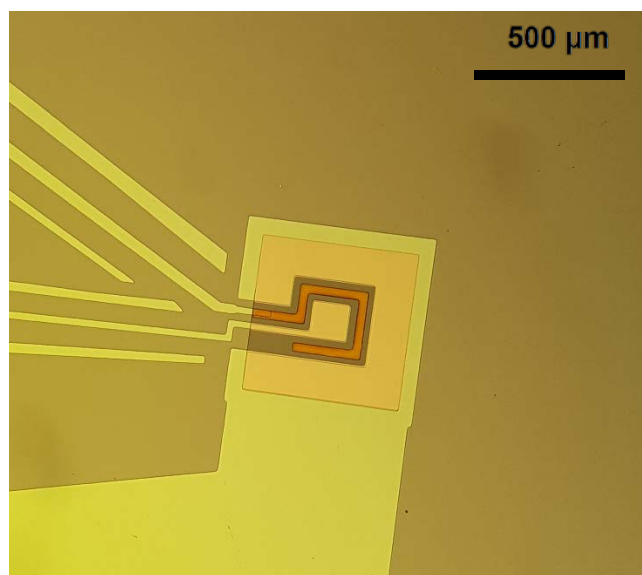


Figure 5.4 Reference electrode built with Ag/AgCl

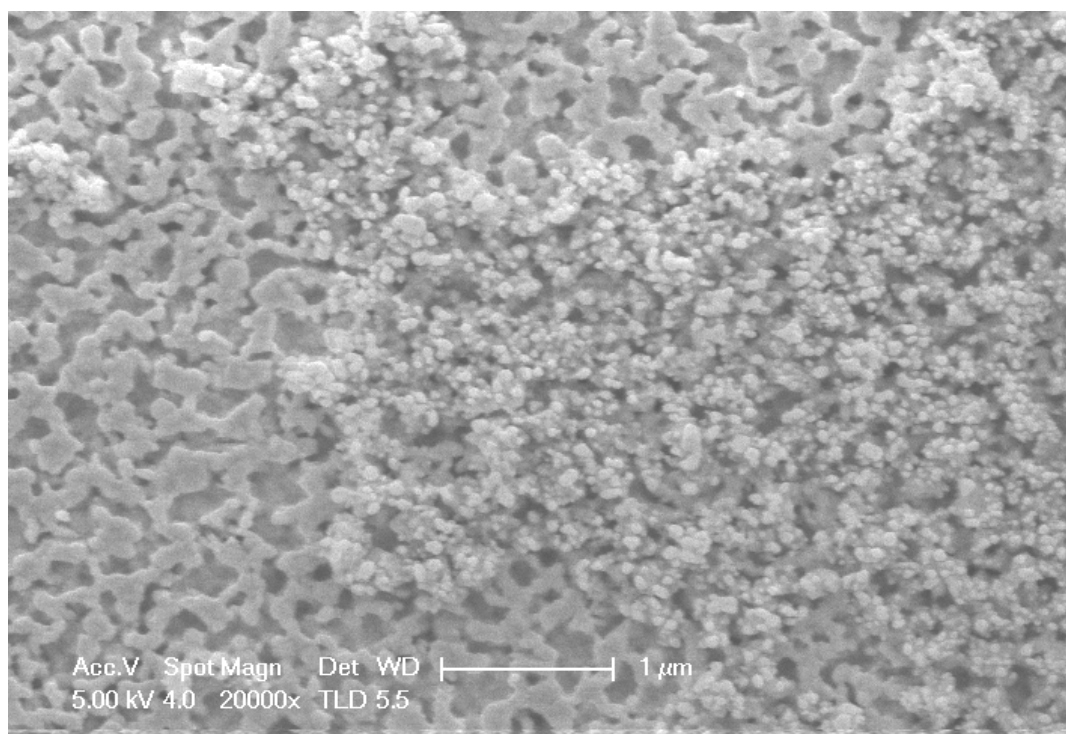


Figure 5.5 SEM image of Ag/AgCl electrode surface. Characteristic clumping of Ag during the chloridization process is visible on the right side.

5.3 Considerations for Seeking Spincoating:

Many methods of immobilizing GOx enzyme on electrodes have been developed for what are now termed 1st generation-type GOx sensors, ranging from applying the enzyme solution manually via drop or dip coat, to screen printing, entrapment inside grown polymer layers, and other approaches. However, most methods are not appropriate for the fabrication of microscale planar electrodes as they do not easily provide tight geometric control over multiple devices in parallel in plane. The most suitable technique for depositing an enzyme layer onto a silicon wafer would be spin-coating [3,4], as it utilizes established tooling and methods to enable uniform films across wafers, which we have extended here for functionalizing large areas with good uniformity and repeatability.

In general, immobilization of enzymes on sensor surfaces is accomplished by mixing the enzymes into a porous polymer matrix. The polymer serves to retain the enzyme near the electrode without over constraining the enzyme such that it can't perform its reaction, and the porosity permits the diffusion of the analytes and reaction products into and out of the matrix. For GOx immobilization, the enzyme is often mixed with bovine serum albumin (BSA) and glutaraldehyde (GA), a crosslinker that can function at protein-safe temperatures, to generate a hydrogel matrix. Typically, these components are pre-mixed, deposited onto the sensor surface by drop-coating or spotting, and then air dried, resulting in a several micrometer thick layer of enzyme-containing polymer. Such layers cover the chosen electrodes, but suffer from limitations in deposited film uniformity and reproducibility during application.

Some important considerations determining the optimal deposition conditions are (a) whether the polymerization of the GA has efficiently developed the crosslinked matrix to adequately retain the enzyme positions and (b) whether the polymerization has limited the enzyme catalytic activity for reacting with the analyte by restricting the motion of parts of the enzyme molecules. To characterize the latter, we can estimate the number of active enzyme molecules in a layer, and observe the signal transduction efficiency, by following Michaelis–Menten kinetic analysis. Based on our experience and of observation of others, a significant fraction of enzyme is inactivated in fabrication or prevented during operation from contributing to measured signal. We can calculate an efficiency of utilization of our deposited enzyme as follows:

Using an estimated density and commercial supplier-stated activity of the coated GOx enzyme and the thickness of our coating, we can calculate an upper

bound of product creation in a layer. Average protein density is 1.3g/cc and half of our layer is BSA, which is very nearly the same size and weight as GOx:

$$\frac{\frac{1.3g}{cm^3}}{2} \cdot \frac{290 \mu mol}{\frac{min}{mg}} \cdot 400nm = 1.2 \frac{nmol}{s \cdot mm^2}$$

We do not have to concern ourselves with diffusion flux if we are considering only saturated response. From the maximum transduced current at glucose saturation in steady state for our sensors we can give the bound of received product at the electrode from an observed saturation current of 200nA:

$$\frac{\left(\frac{200nA}{120\mu m \cdot 120\mu m + 190\mu m \cdot 20\mu m} \right)}{2 \cdot F} = 0.056 \frac{nmol}{s \cdot mm^2}$$

A greater than 90% loss of possible product is likely not entirely due to diffusion effects, but also represents the presence of enzyme inactivated in the fabrication process. These estimates were made considering our in vitro devices tested in buffer solution while in vivo devices have many more additional concerns causing signal loss.

These modest measured catalytic efficiencies may result from the inefficient diffusion of H₂O₂ from the enzymatic reaction sites near the top of the coating, where the H₂O₂ is generated by reaction with the exposed environment, down to the electrode contact. During this diffusion process, the H₂O₂ can oxidize bonds in GOx molecules, reducing the number of functional molecules available for glucose detection [5], or may be lost in oxidation processes with the polymer matrix. Moreover, the O₂ generated by the oxidation of H₂O₂ is typically formed micrometers away from the location where it can contribute to the next enzymatic reaction, and is able to diffuse away from the enzyme region entirely, limiting the sensor linearity and sensitivity by lowering availability of one of the kinematic components of the enzyme reaction. In order to improve the substrate to signal transduction efficiency, it is therefore desirable to develop geometries in which the enzyme reaction occurs close to the electrode surface so that the H₂O₂ is efficiently and rapidly converted into measurable working electrode current and in which the O₂ generated by H₂O₂ dissociation is efficiently recycled to supply the next glucose reaction.

A simple approach to improve enzyme reaction to signal transduction efficiency is to reduce the thickness of the active enzyme layer. This immediately aids in the H₂O₂ capture efficiency, as the most common point of reaction, the top of the hydrogel matrix, is brought closer to the reading electrode and the H₂O₂ residence time is reduced, such that it is more likely to reach the electrode. Because of the high

viscosity and the complexity of the interactions between the components of the enzyme layer mixture, traditional deposition techniques, such as dip-coating, drop-coating, ink-jet printing and spotting all result in micron-thick enzyme layers. The diffusion behavior within the immobilization layer is highlighted when there is no additional topcoat diffusion barrier applied as in this work, but similar considerations still apply regarding efficient consumption of H_2O_2 generated. The reaction-to-transduction distance is still dependent on the immobilization layer thickness. A thinner enzyme layer will not provide a large buffer to long term enzyme decay, but does reduce hazardous H_2O_2 exposure for the enzyme layer and increase sensor response speeds. Since FBC-induced failure is seen to precede enzyme failure in *in vivo* devices this may be a reasonable tradeoff.

Spin coating is widely used in semiconductor microfabrication as a method of depositing polymers in uniform thin films over large flat areas quickly and cheaply. Polymer-in-solvent photoresists can be reliably spread across a 200mm or wider diameter wafer surfaces with a uniform layer thickness ranging from less than 50nm to over 50 μ m, depending on the solution viscosity and rotation speed. A small amount of coating material is typically applied onto the center of the flat substrate, which is then rotated at high speed in order to spread the coating material by centrifugal force. Since the wafer may contain many devices, the uniform layer enables processing these in parallel. Rotation is continued while the fluid spins off the edges of the substrate, until the final desired thickness of the film is achieved. The same methodology can be applied with an enzyme-containing solution such as GOx/BSA in water as a coating layer on top of lithographically patterned planar electrodes distributed across a silicon wafer substrate. The spin coating of GOx onto planar surfaces [4] or as permeable membranes [6,7] has previously been demonstrated. However, it is not essential that the polymer crosslinker be added to the solution prior to the spin-coating and the devices can benefit from crosslinking as a subsequent step. GA has been used extensively as a crosslinking agent for biomedical materials such as collagen and albumin and a more recent method for the addition of GA is via vapor deposition [8,9]. By performing the spincoat process without GA in the coating solution, the uniformity of the layer can be improved significantly by avoiding changes in viscosity and clumping due to the ongoing polymerization. After spin-coating a mixture onto the sensor surface, we generate a GA cross-linked structure by exposing the enzyme layer to GA vapor in a low vacuum chamber. This two-step deposition approach enables us to reliably deposit enzyme layers with thicknesses below 500nm. The resulting device architecture can

easily be applied to dense, large-area wafer device arrays for high volume, cost-efficient fabrication.

5.4. Reagents and Materials

Glucose Oxidase from *Aspergillus niger* was purchased from BBI Solutions (#GO3A). Bovine serum albumin (AMRESCO # 97064-340) and 10X Phosphate Buffer Saline, Molecular Biology Grade (Corning #46-013-CM) were purchased at VWR. D-(+) Glucose (Sigma #G8270) and 25% Glutaraldehyde, electron microscopy grade (ACROS #23328) were purchased via VWR. Sodium Benzoate ge 99.0%(ACROS #AC148980010) was purchased at Fisher Scientific. Solutions were diluted using deionized water (resistivity 18.0 M Ω cm) filtered through 0.22 μ m pores (Durapore #CVDI02TPE) and UV sterilized (Aquafine). MicroChemicals AZ 5214-IR was the primary photoresist used. ACS Reagent grade acetone and isopropyl alcohol were used for liftoff.

Titanium (99.99%) and platinum (99.99%) were purchased from Kurt J. Lesker Company. 100mm silicon wafer substrates were utilized from a variety of sources since they are used only as a platform.

5.5. Instrumentation

Microfabrication of the three-electrode platinum planar devices (see Fig 5.6) was performed with standard photolithography tooling and depositions were performed with a CHA Industries Mk40 electron beam evaporator utilizing an IC/5 Inficon deposition control and quartz crystal thickness monitor. Silicon oxidation was performed with a Tystar Tytan furnace. Trace line insulation layers were built and patterned using an Oxford PlasmaPro 100 PECVD and an Oxford ICP PlasmaPro 380 RIE respectively.

A Laurell WS-400 Spin Coater was used for the application of GOx-containing solution to the wafers. GA deposition was performed with a hot plate contained in a bell jar. Thickness measurements were carried out on the wafer with Dektak XT Stylus profilometer.

All electrochemical experiments were performed with Keithley Instruments 2450 SourceMeters operating in 3-electrode potentiostat mode. The finalized devices were evaluated in a custom built fluidic cell system with centralized control of potentiostat reading and analyte concentration delivery to each cell.

5.6. Experimental Methods

5.6.1 Electrode Fabrication

The microelectrode systems were built using standard photolithography and thin film patterning techniques in a cleanroom environment. A silicon substrate was first thermally oxidized at 1000°C to grow a 2.5µm thick layer for isolating the metallic devices from each other and the substrate. Electrodes and traces to probe pads were patterned via liftoff of an electron beam evaporated film consisting of a 10nm Ti adhesion layer and a 100nm Pt sensor surface defining a working electrode (WE), counter electrode (CE), and reference electrode (RE), along with guard traces which improve voltage potential homogeneity. Then a 240nm thick layer of SiO₂ and 20nm of Si₃N₄ were deposited via PECVD, in order to insulate the trace lines from the cell solution. Openings for the defined electrode areas and probe pads were generated by photolithography and subsequent fluorine-based plasma etching. Subsequent metal layers for the electrodes were added in a manner similar to the first layer in order to achieve a material, thickness, or surface profile of choice. Prior to enzyme spin coating, a photoresist mask was patterned to constrain the functional region to within the 500µm footprint. The data presented in this work utilized a second layer of platinum and enzyme geometries that only coated the three initially defined electrodes after an acetone liftoff process. Though non-critical and perhaps counterproductive in this particular example, the rationale of this patterned electrode process will become more clear when membrane layers are included in the next chapter. For comparison, dropcoat-type wafers were also fabricated. These have no additional patterning performed and the coating geometry relied on the syringe process.

5.6.2 Electrode Functionalization

The enzyme layer solution for spincoating was prepared by dissolving 0.56g of GOx and 0.047g of BSA in 7ml of 1X PBS solution. The enzyme solution was then vortexed for 30s and centrifuged for 1 min. The enzyme mix was dispensed with a plastic pipette onto the wafer centered on the spinner and spin-coated at 500 rpm for 10s followed by 4000 rpm for 30s, accel. 0.15. Subsequently, the wafer was placed next to, but thermally isolated from, a 80°C heated GA source within an evacuated bell jar, which was allowed to vapor deposit for 7.5 minutes on top of the GOx/BSA layer. The sample was then removed and given 30 minutes of relaxation

time before further handling. Functionalized sensor wafers were stored at room temperature with electrodes immersed in PBS.

Drop coating was used as a deposition method for our comparison devices as informed by Shi et al [10]. A 20 μ l GOx / BSA solution comprised of 1.6 mg of GOx and 1.3 mg of BSA in 1X PBS was vortexed for 15s and then centrifuged for 15s. 25% GA was then diluted 10:1 with 1X PBS. 6 μ l of the GOx /BSA solution was mixed with 2 μ l of GA and then vortexed for 5s and centrifuged for 5s, while seeking to minimize the amount of time before final deposition in order to prevent early polymerization. The sensing layer was then applied by dispensing 1 μ l of the GOx/BSA/GA solution via pipette onto the electrodes. Beginning room temperature polymerization before final deposition requires tight timing control in order to obtain good reproducibility with this deposition method.

The complete fabrication process is illustrated in Fig 5.7.

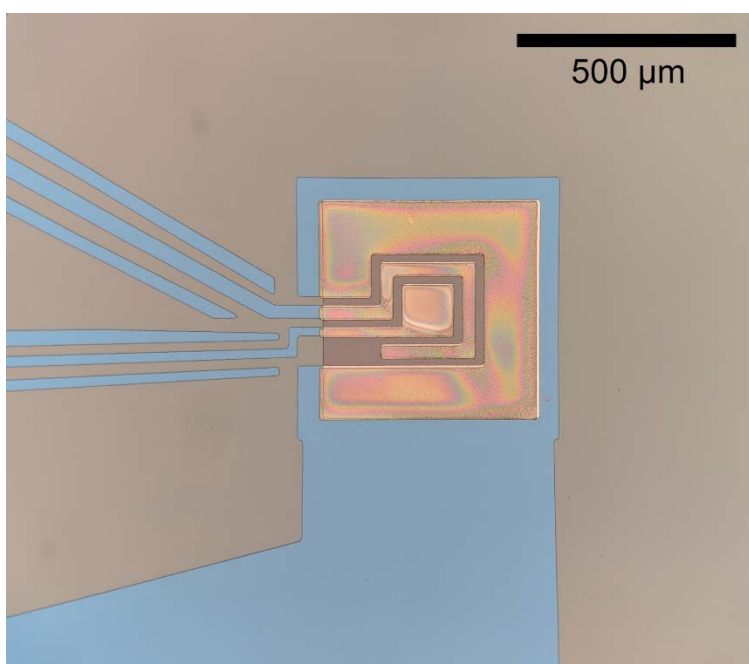


Figure 5.6 Three-electrode platinum GOx-coated sensor. Pads in order from center outwards: WE, RE, CE. Blue regions are connection traces covered by Si₃N₄/SiO₂ insulation

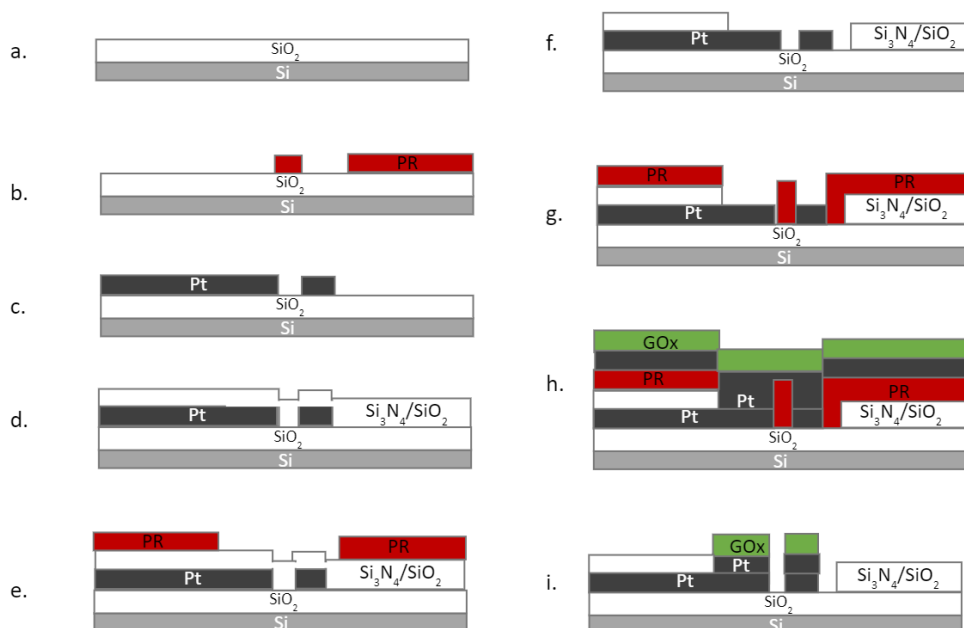


Figure 5.7 Spincoat wafer fabrication sequence: (a.) thermal oxidation of silicon substrate (b.) photoresist patterning (c.) platinum deposition and liftoff (d.) PECVD Si_3N_4 and SiO_2 (e.) photoresist patterning (f.) plasma etching (g.) photoresist patterning (h.) platinum evaporation and GOx spincoat. (i.) acetone liftoff

5.6.3 Experimental Measurement and Analysis Methods

Completed wafers were loaded into a custom probe system to provide voltage control to the WE, CE, RE, and guard trace lines via the potentiostat instruments. The probe system utilizes an array of aligned and o-ring sealed wet cells for delivering chosen concentrations of glucose to independently measured electrode sets across a wafer (Fig 5.8). These cells are serially connected by tubing in order to reduce the complexity of the external solution delivery system. Solutions of 1X PBS 0.1 w/v% sodium benzoate with clinically relevant glucose concentrations (0-40 mM) were prepared and fed in randomized sequences to all cells simultaneously at room temperature (22°C). The cell contents are flushed between measurements by 10,000 times the volume of the cell for 60 seconds and then a 5 second rest time is given before the electrodes are polarized for measurement. The measurements were conducted for 60 seconds at each concentration with 0.1s intervals. Each concentration is delivered 4-8 times in non-repeating sequences to eliminate

hysteretic effects. Uncertainties in solution preparation and electrical measurement were exceeded by the variance between measurement sweeps caused by the fluidic pumping system or oxidation state of the platinum surface. However, the variation between electrodes was observed to exceed the per sweep measurement variance.

During measurement, the WE is set to +0.4V versus the platinum RE of the same electrode set and solutions are expected to have room temperature oxidation levels which provide sufficient stability for the Pt RE. The oxidation current due to H_2O_2 produced by GOx in reference to glucose concentration was recorded and representative data is plotted below.

Fitting parameters are obtained via Matlab for the limiting exponential behavior of each sensor. An apparent K_M and electrical current I_{max} or product concentration V_{max} are determined via the Lineweaver-Burk method. Exponential fit parameters as described in Chapter 3 are utilized as well to better compare sensor-to-sensor performance and performance over time due to aforementioned violations of single-substrate M-M kinetics.

Measurement sweeps through multiple concentrations and iterations typically ran for 1-2 hours. Afterwards the electrode sets were maintained in PBS until the next measurement round.

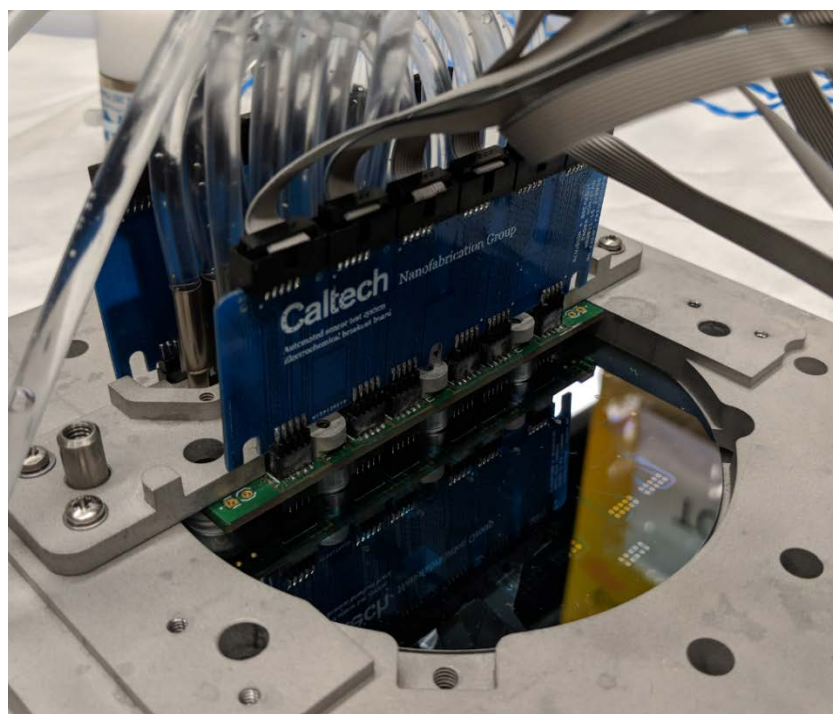


Figure 5.8 Wafer measurement station. Routing of fluidic and electrical connections to planar electrode sets visible.

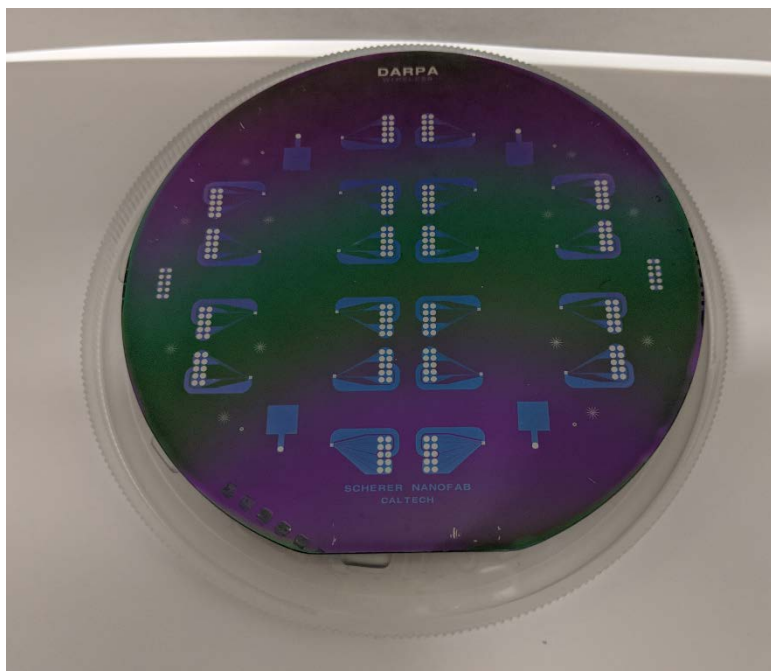


Figure 5.9 100mm wafer electrode layout. Electrode geometry is shown in Figure 5.6

5.7. Characterization

5.7.1 Layers

Twenty 3-electrode devices were built per wafer, evenly distributed over the surface as in the diagram Fig 5. The platinum WE was patterned at $.0182 \text{ mm}^2$, enclosed by an RE and CE within a total area of $500\text{micron} \times 500\text{micron}$. Figure 5.6 shows the typical geometry of the potentiostat electrodes. The enzyme spincoats were evaluated via profilometer on dummy samples of identical fabrication process to the wafers evaluated amperometrically. At 5000rpm the average enzyme layer thickness was 490nm with 158nm standard deviation between devices.

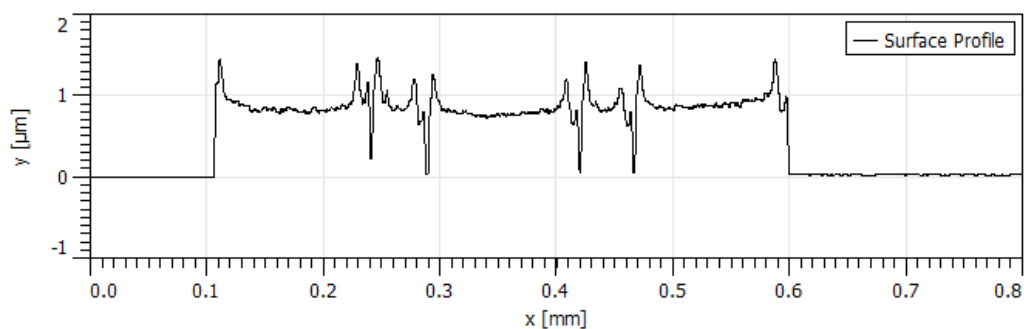


Figure 5.10 Surface profilometry of the enzyme spincoat post liftoff. Wake structures at the spincoat edges are visible. Non-flat regions between electrodes are due to tip width.

5.7.2 Amperometric Data and Kinetics

After flushing a potentiostat cell with new glucose concentration solution, measurements are initiated to find the steady-state signal and time-until-stability. Solutions experiments in the range of 0mM to 5mM or 0mM to 40mM were iterated through, in randomized order, each 5-10 times. A current-concentration response curve is shown in Fig. 5.11 from measurement sweeps of a spincoated wafer and dropcoated wafer. Averaging the initial measurement across the 7 devices plotted gives the following kinetics with standard deviations:

	K_M^{app} (mM)	I_{max} (nA)
Spincoat Process	5.14 ± 0.26	256.0 ± 34.1
Dropcoat Process	3.16 ± 0.65	91.45 ± 19.2

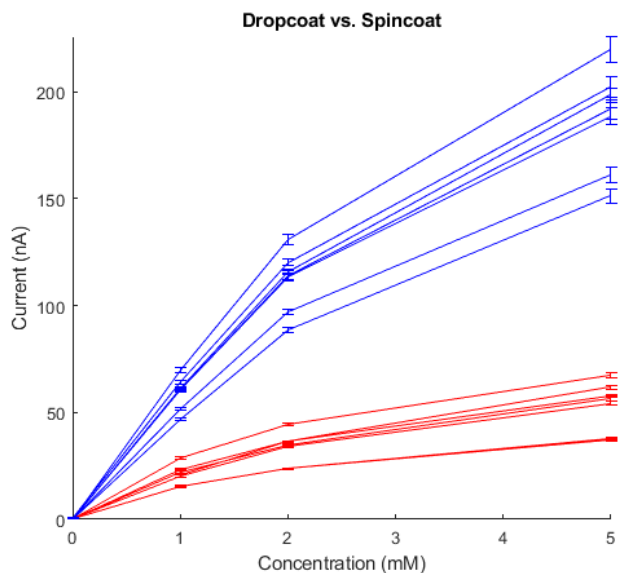


Figure 5.11 Current-concentration data from 7 electrodes, from spincoat (blue) and dropcoat (red) type wafers.

5.7.3 Transient Behavior

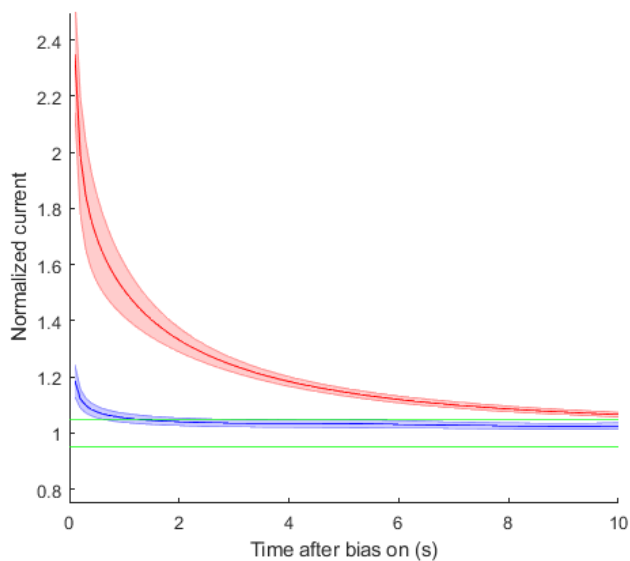


Figure 5.12 Sensor stabilization comparison of dropcoat (red) and spincoat (blue) type electrodes within their first 10 seconds of bias. Green bounding bars represent 5% deviation from 60s value. Normalizations are averaged over 9 electrodes of each type.

In addition to increasing the enzyme conversion efficiency, another key advantage of reducing the thickness of the enzyme layer is improving the response speed of the sensor to changes in analyte concentration, as well as the initial turn-on-to-accurate signal time of the sensor. In thicker, drop-coat type sensors, we observe the sensor response does not settle for bias times under 10 seconds, which may be due to the diffusion lengths of the analytes and products through the coating. In thin enzyme layers, we have observed the in vitro stabilization delay can be reduced to below 0.5 seconds, which may enable the opportunity of conducting pulsed measurements with a significant reduction in the energy required by the sensor system. By shortening the duty cycle but still utilizing the same bias voltage and operation power, total energy needs are reduced. To observe the dynamics of the sensor response, we have plotted time-dependent readings of sensor current for both thick (dropcoat) and thin (spincoat) enzyme layers (Fig 5.12). With these curves, we can predict the settling time required to obtain a stable and accurate reading. The data is normalized against the final 60 second current value, which is (highlighted) by 5% deviation bounding bars. Defining a true steady state is complex due to the nature of the platinum reaction and limitations of building a small volume diffusion cell.

Using layers with faster dynamics allows for more frequent, accurate reading which has understood benefits for patient treatment. Total energy requirements are reduced by the ability to briefly pulse a measurement that rapidly settles rather than be concerned about stabilization of the electrochemistry after biasing. Particularly since the dynamics of concentrations are much slower than these pulsing times, the same amount of data is learned with far less energy consumed. The ability to collect a data point rapidly is more tolerant to patient error with a wireless recording device since it reduces the time a patient must have successfully brought the external antenna and subdermal implant within range of each other which may be difficult since the implant is not visible to the patient.

5.7.4 Sensor Lifetimes

Apart from the sensor performance metrics, an important aspect in any application of a biosensor is the lifetime, deterioration rate, and understanding the mechanism of that deterioration. To confirm our in vitro sensor lifetimes we have performed measurement sweeps over the course of 45 days. Fig 5.14. shows the slow drift of K_M and I_{max} during this time period. These are viable sensor parameters during this period and did not indicate impending decline after the measurement

period had ending. The addition of a flux limiting membrane would stabilize the K_M over the functional life of the sensor, but this work is focused solely on the properties of the enzyme layer [1]. It is yet to be determined how much sacrificable enzyme must be present to guarantee linearity during enzyme decay for these sensors in vivo. Overall these K_M ranges agree with prior reported in vitro GOx on Pt measurements.

We have also examined the change in signal settling over these lifetime measurements and observed improved consistency via spincoat devices over dropcoat devices as shown in Fig. 5.15. We also observed that the spincoat glucose measurement settling behavior mirrors a pure H_2O_2 on platinum measurement of the same geometry and hence the glucose dynamics have been inherently shortened.

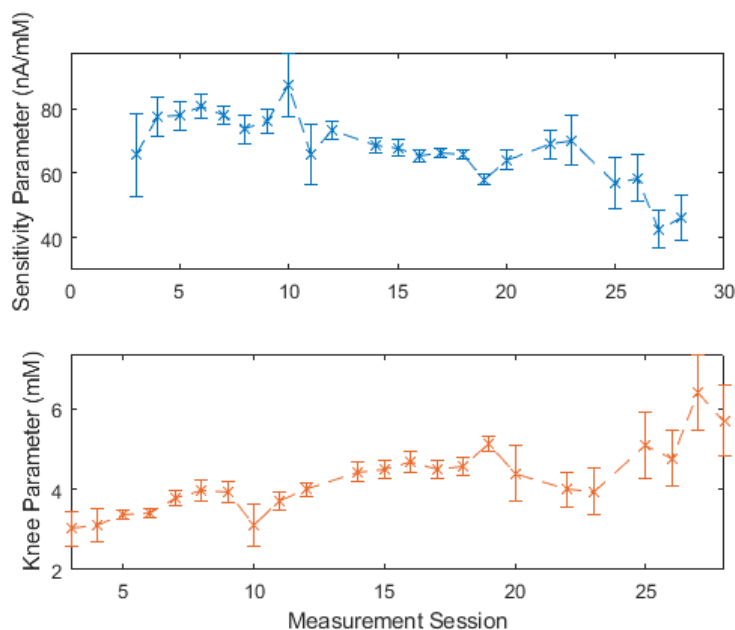


Figure 5.13 Sensitivity and exponential knee over 35 days of measurements, averaged over 5 electrodes.

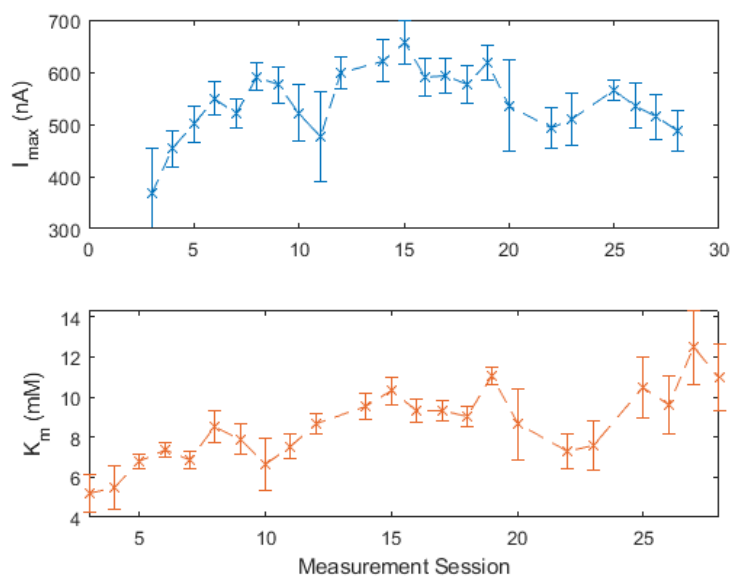


Figure 5.14 I_{\max} and K_M over 35 days of measurements, averaged over 5 electrodes.

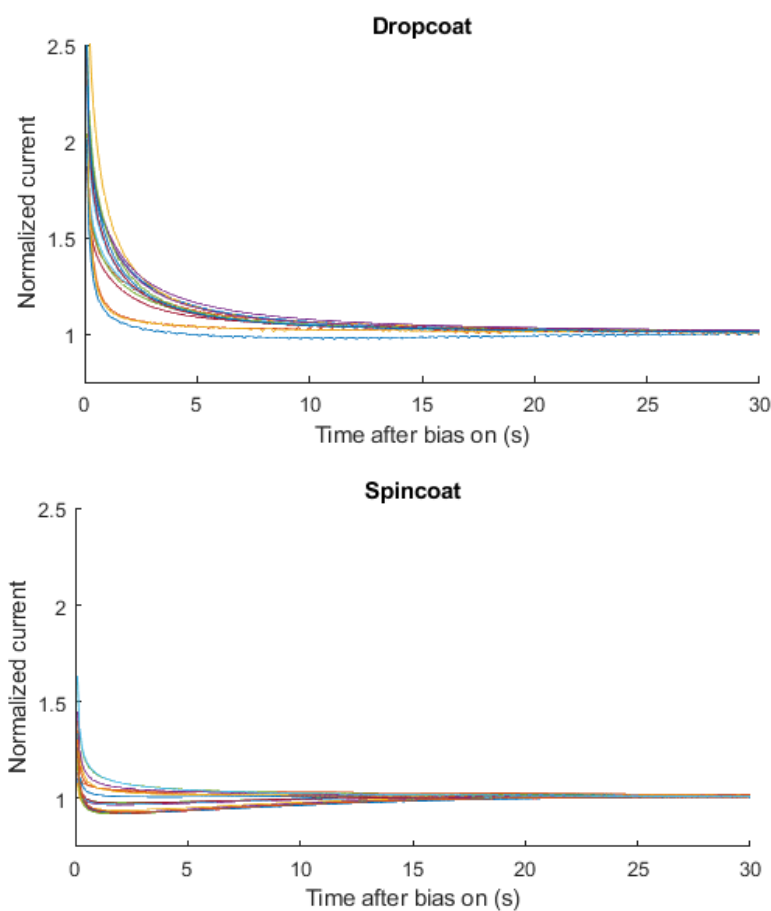


Figure 5.15 Settling times for dropcoat-type and spincoat-type wafers over 19 days.

5.8. Concluding Observations

We have observed that a combined methodology of applying glucose oxidase via spincoat and vapor deposition of GA is a viable approach to ease mass production while improving sensor performance. Spincoat enzymes have unique advantages in diffusion dynamics and substrate balance that make them more efficient devices than can be made via dropcoat means. The results demonstrate that building planar enzyme electrodes for future microfabrication CGM devices could be done with reduced QA and calibration costs.

References

- [1] M. Mujeeb-U-Rahman, D. Adalian and A. Scherer, "Fabrication of Patterned Integrated Electrochemical Sensors", *Journal of Nanotechnology*, vol. 2015, pp. 1-13, 2015. Available: 10.1155/2015/467190.
- [2] M. Henry, "ICP Etching of Silicon for Micro and Nanoscale Devices", Ph.D. Dissertation, California Institute of Technology, 2010.
- [3] I. Ges and F. Baudenbacher, "Enzyme electrodes to monitor glucose consumption of single cardiac myocytes in sub-nanoliter volumes", *Biosensors and Bioelectronics*, vol. 25, no. 5, pp. 1019-1024, 2010. Available: 10.1016/j.bios.2009.09.018.
- [4] J. Kimura, A. Saito, N. Ito, S. Nakamoto and T. Kuriyama, "Evaluation of an albumin-based, spin-coated, enzyme-immobilized membrane for an isfet glucose sensor by computer simulation", *Journal of Membrane Science*, vol. 43, no. 2-3, pp. 291-305, 1989. Available: 10.1016/s0376-7388(00)85104-2.
- [5] K. Kleppe, "The Effect of Hydrogen Peroxide on Glucose Oxidase from *Aspergillus niger*", *Biochemistry*, vol. 5, no. 1, pp. 139-143, 1966. Available: 10.1021/bi00865a018.
- [6] C. Chang, C. Pai, W. Chen and S. Jenekhe, "Spin coating of conjugated polymers for electronic and optoelectronic applications", *Thin Solid Films*, vol. 479, no. 1-2, pp. 254-260, 2005. Available: 10.1016/j.tsf.2004.12.013.
- [7] A. Soldatkin et al., "Glucose sensitive conductometric biosensor with additional Nafion membrane: reduction of influence of buffer capacity on the sensor response and extension of its dynamic range", *Analytica Chimica Acta*, vol. 288, no. 3, pp. 197-203, 1994. Available: 10.1016/0003-2670(93)e0627-j.
- [8] Y. Peng, V. Glattauer and J. Ramshaw, "Stabilisation of Collagen Sponges by Glutaraldehyde Vapour Crosslinking", *International Journal of Biomaterials*, vol. 2017, pp. 1-6, 2017. Available: 10.1155/2017/8947823.

[9] B. Zhu, W. Li, N. Chi, R. Lewis, J. Osamor and R. Wang, "Optimization of Glutaraldehyde Vapor Treatment for Electrospun Collagen/Silk Tissue Engineering Scaffolds", *ACS Omega*, vol. 2, no. 6, pp. 2439-2450, 2017. Available: 10.1021/acsomega.7b00290.

[10] J. Shi et al., "A comparative study of enzyme immobilization strategies for multi-walled carbon nanotube glucose biosensors", *Nanotechnology*, vol. 22, no. 35, p. 355502, 2011. Available: 10.1088/0957-4484/22/35/355502.

Chapter 6 Sputtered Layers on Immobilized Enzyme

6.1 Overview:

We have developed a new strategy for the microfabrication of microfabricated enzyme-based electrochemical sensors utilizing sputtered metal layers as diffusion, collection and protection barriers on top of a enzyme-embedded polymer layers. High performance glucose sensors were defined by using spincoat deposition approaches of the glucose oxidase (GOx) enzyme onto photoresist patterns with subsequent polymerization by glutaraldehyde (GA) vapor deposition, building on the methods developed in the previous chapters. A thin platinum layer was then vacuum magnetron sputtered onto the polymerized enzyme matrix. Finally, a liftoff process was used to isolate the electrodes from each other. Electrodes coated with this multilayer structure were built on silicon wafer substrates to define three electrode configurations adapting from the previously evaluated designs from Chapter 5. The resulting devices exhibited improved sensor performance, with K_M increased beyond expected physiological glucose concentrations and excellent linearity above 6mM in 1x PBS. This research sought to demonstrate the utility of using sputtered metal protective coatings integrated into the layer design for amperometric enzymatic biosensors. The nanoporous structure of the sputter-deposited platinum layers provide decreased effective diffusion rates with correspondingly valuable size selectivity. Platinum and other noble metals may also serve as stable in vivo protective layers, protecting the enzyme from attack by the immune system. And alternatively, when electrically connected with the bottom sensor electrode, this layer creates a sandwich structure with excellent peroxide capture efficiency. Thin sputtered layers, combined with spincoat enzyme processes, enable the use of standard photoresist techniques for high-performance microfabricated enzymatic sensors.

6.2. Considerations for Barrier Layers:

Existing Continuous Glucose Monitors (CGMs) have been developed primarily using GOx enzyme in conjunction with organic protective barrier layers to limit the effect of immune response on the functional enzyme molecules, to screen interferences, and to restrain the flow of analyte to a below enzyme kinetics saturation pace [1]. In the effort to further miniaturize this technology, we must also focus on finding microfabrication solutions to the barrier layers of these

devices to ease the mass manufacture and standardization of sensors electrodes [2]. The prior chapter established methods of selectively patterning the enzyme coated areas on substrates, and now we expand those techniques to permit patterning of a thin film metal barrier layers. Spincoat enzyme deposition will continue to form the basis for device functionalization as it is compatible with wafer-scale photolithographic liftoff processing.

Through the past 60 years of the fabrication of glucose sensors, an appropriate flux-limiting outer membrane on top of the GOx immobilized layer of the electrode has been a critical component to device viability, controlling the oxygen/glucose concentration differential in vivo. In order to control the flux of oxygen and glucose, numerous polymer layers that selectively slow the diffusion of glucose relative to dissolved oxygen have been examined [3]. The decreased flux of glucose also enables a more linear current response by the enzyme layer, since it is kept well below glucose saturation levels (visualization provided in Figure 6.1) and oxygen concentrations do not limit the enzyme-assisted conversion reaction. This linearization is preferable for in vivo sensor signal fidelity and interpretation, where changes in enzyme activity must be re-calibrated with time. A barrier layer can also serve to encourage enzyme-formed H₂O₂ to diffuse to the lower electrode surface for electrochemical oxidation, and thus improve its capture efficiency and reduce local tissue damage [4]. As described previously, the top membrane can also be used to filter out electro-active interferent molecules that degrade and obscure the sensor selectivity to glucose, bypassing the peroxide-platinum reaction. Finally, top membranes can protect the enzyme and electrode surface from oxidizing species, proteins, and the other immune response chemistries.

Even the most resilient polymers currently used to protect bio-functionalizing layers, such as polyurethane and Nafion, are understood to decay with time in vivo due to swelling/cracking, calcification, peroxide damage, and other immune chemistry attack [5,6]. As far as we know, there are no previously described examples of sputtered metals being examined prior to this research work as protective membranes on biochemical sensor layers. As the density, thickness and porosity of such layers can be optimized, we propose that a porous metal overcoating could have similar size-specific, diffusion limiting effects, while potentially being prone to less damage in addition to other new benefits, as discussed below.

Platinum is an attractive material for the sputtered coating due to its well described nobility and biocompatibility characteristics [7]. Platinum is utilized as a catalytic surface for many types of chemical reactions [8,9,10,11,12]. Relative to

other materials, platinum does not undergo significant dissolution when in use, which may be a relevant property in blocking molecules known to damage enzyme sensors while providing long-term signal stability. We have observed excellent binding of the sputtered platinum onto the enzyme layer, and have directly tuned its porosity by altering the thickness of the sputter deposition process. The behavior of this additional layer can be estimated as a region with a selectively reduced effective diffusion coefficient as a function of the size of the diffusing molecule. The layer can also be chosen to either serve as part of the electrode circuit and thus act as a sandwiching structure for consumption of the analyte, or as an isolated metal electrode that can screen molecules without affecting the measurement circuit. In the latter form it may act either as a floating electrode which is undergoing equilibrium reactions, or could be a driven electrode configured similarly to a bipotentiostat system. In driven form, voltages could be selected for particular screening goals without modifying the current read through the bottom working electrode.

In this work, the primary device performance criteria we sought to improve was the linear range of sensor performance with glucose concentration. Therefore, we optimize the platinum layer's diffusion limiting behavior and the endurance lifetime of the GOx enzyme layer as a sensor through the Pt fabrication process.

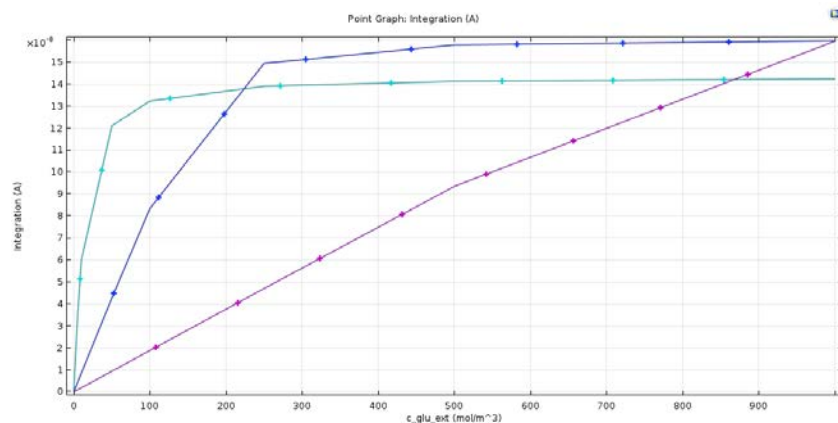


Figure 6.1 Visualization of signal linearity control. Dependent on the strength of a diffusion barrier, the concentration-current response for a sensor can be shifted from M-M saturation behavior to linear in the desired regime.

6.3. Reagents and Materials

The spincoat layers were prepared from the same materials as described in Section 5.4. MicroChemicals AZ 5214-IR was the primary photoresist used. ACS Reagent grade acetone and isopropyl alcohol were used for liftoff.

Titanium (99.99%) and platinum (99.99%) evaporation sources were purchased from Kurt J. Lesker Company. Titanium (99.995%) and platinum (99.99%) sputtering sources were purchased from ACI Alloys. 100mm silicon wafer substrates were utilized from a variety of sources since they are used only as a platform.

6.4. Instrumentation

The equipment used in the manufacture of the base layers of the devices are the same as described in Section 5.5. Sputterings were performed in a custom built tool using AJA International 2" diameter sputter guns with turbopumping and gas flow control. A Laurell WS-400 Spin Coater was used for the application of GOx-containing solution to the wafers. GA deposition was performed with a hot plate contained in a bell jar.

All electrochemical experiments were performed with Keithley Instruments 2450 SourceMeters operating in 3-electrode potentiostat mode. The finalized devices were evaluated in a custom built fluidic cell system with centralized control of potentiostat reading and analyte concentration delivery to each cell.

6.5. Experimental Methods

6.5.1 Wafer Processing

Wafer fabrication shares many similar steps as those described in Section 5.6.1. However, it has been observed that subtle fabrication choices can dramatically affect the electrochemical activity of platinum so they are detailed here. A silicon substrate was first thermally oxidized at 1000°C to grow a 2.5µm thick layer for isolating the metallic devices from each other and the substrate. Electrodes and traces to probe pads were patterned via liftoff of an electron beam evaporated film consisting of a 10nm Ti adhesion layer and a 100nm Pt sensor surface defining a working electrode (WE), counter electrode (CE), and

reference electrode (RE), along with guard traces which improve voltage potential homogeneity. Then a 240nm thick layer of SiO₂ and 20nm of Si₃N₄ were deposited via PECVD, in order to insulate the trace lines from the cell solution. Openings for the defined electrode areas and probe pads were generated by photolithography and subsequent fluorine-based plasma etching.

Two alternative procedures were applied in final electrode surface fabrication. A photoresist pattern of identical geometry to the bottom electrodes was patterned and then used in a platinum liftoff process repeating the deposition described above. And subsequently a photoresist mask with a 500μm x 500μm window over the electrodes was used in a liftoff process for the enzyme layer (Fig 6.3). Alternatively, the enzyme spincoat may be performed before the platinum liftoff into the same photoresist pattern and then lifted off concurrently.

6.5.2 Electrode Functionalization

See Section 5.6.2 for the spincoat enzyme method.

6.5.3 Topcoat Sputtering and Liftoff

After sufficient relaxation time for excess GA to evaporate, the wafer is then loaded into a high vacuum chamber. During deposition with a magnetron sputter source, the argon flow to the chamber was limited to 50sccm via a mass flow controller while the chamber pressure was maintained at 10mTorr. A 80W DC magnetron plasma was struck in front of the platinum sputter target, and the platinum deposition rate was determined to be 10nm/minute. Typical final coat thicknesses were 50nm and 200nm. The sample was then removed from the chamber and soaked in acetone with periodic ultrasonic agitation for approximately 2 hours. For some of the experimental comparisons described below, platinum was only sputtered only half of the devices on a single wafer by partially occluding the wafer surface during the sputtering process.

The complete fabrication process is illustrated in Fig 6.2.

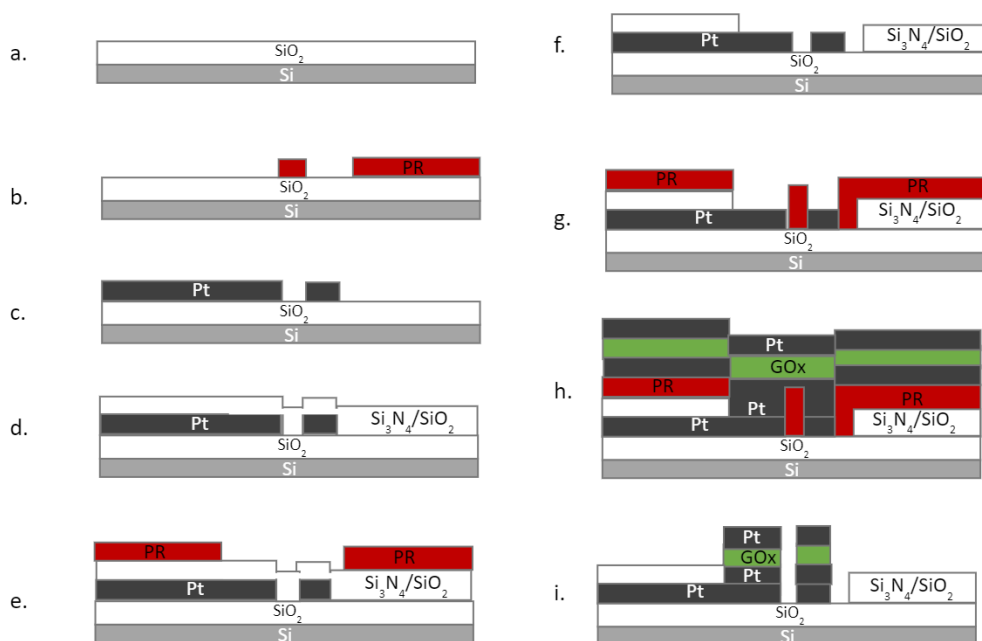


Figure 6.2 Sputter coated sensor fabrication sequence: (a.) thermal oxidation of silicon substrate (b.) photoresist patterning (c.) platinum deposition and liftoff (d.) PECVD Si_3N_4 and SiO_2 (e.) photoresist patterning (f.) plasma etching (g.) photoresist patterning (h.) platinum evaporation, GOx spincoat, and platinum sputtering (i.) acetone liftoff

6.5.4 Experimental Measurement and Analysis Methods

Measurement methods and analysis are similar to as described in Section 5.6.3. Additional focus was placed on the linearization of the measurement signals which was characterized by simple linear regression. As described in the fabrication, some comparison tests were performed by analyzing data between separate wafers, and some were performed by comparing electrodes of different fabrication design on the same wafer to reduce fabrication variance effects. For wafers fabricated with their platinum electrode and enzyme layers in separate photolithography steps, calibration measurements of peroxide in PBS were performed, but this was found to degrade the efficiency of the GOx sensor due to platinum passivation. Functionalized sensor wafers were stored at room temperature with electrodes immersed in PBS between measurement sessions.

6.6. Characterization

6.6.1 Devices and Layers

Twenty 3-electrode devices were built per wafer as described in Section 5.7.1 and shown in Figure 5.9. For comparison tests within the same wafer, the top 10 electrodes were constructed with platinum sputter coats and the bottom 10 electrodes are of standard spincoat form without a barrier.

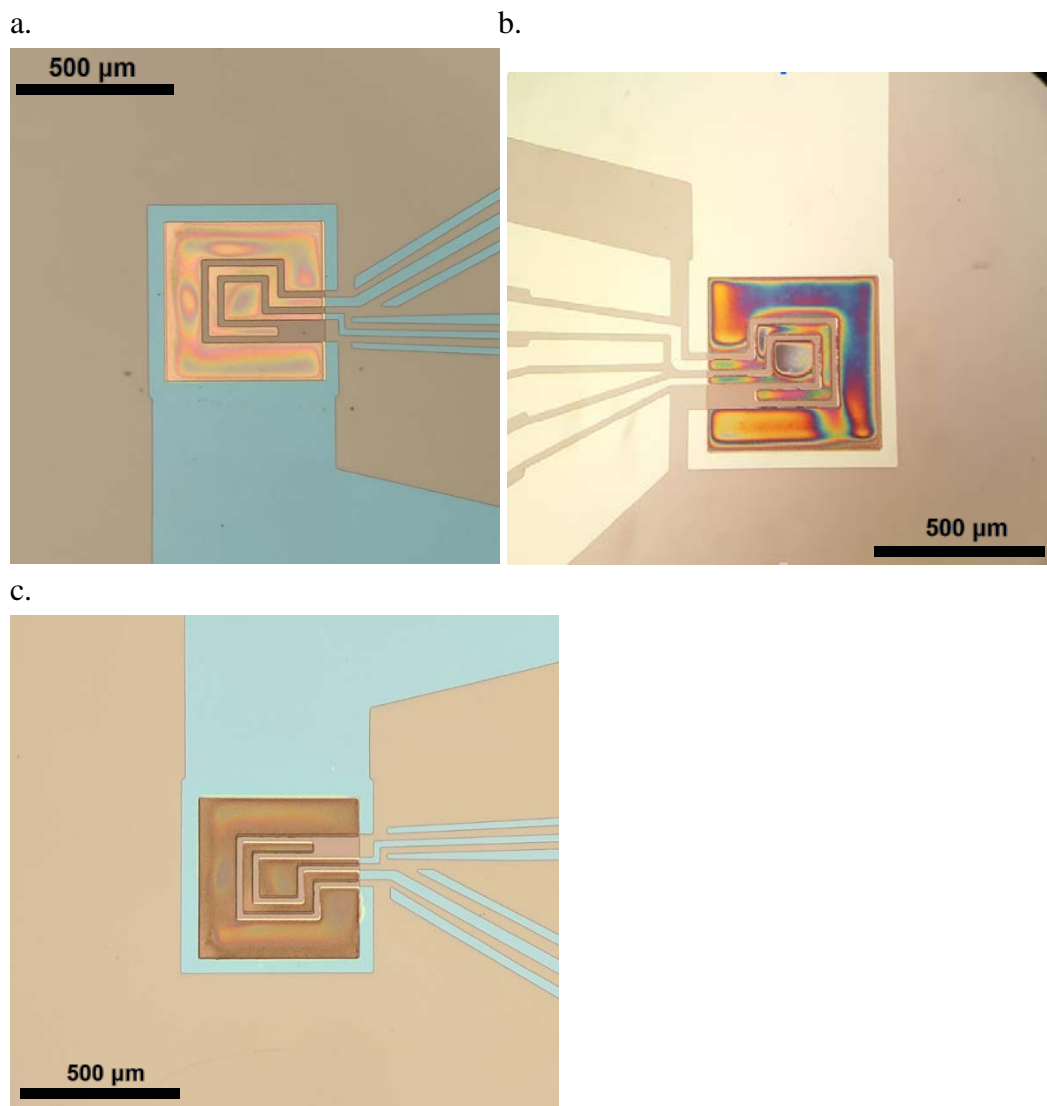


Figure 6.3 Electrode coating comparisons. (a) uncoated GOx enzyme layer (b) 50nm sputtered platinum coat over enzyme layer (c) 200nm sputtered platinum coat over enzyme layer

6.6.2 Amperometric Data

After flushing a potentiostat cell with new glucose solution, measurements are initiated to find the steady-state signal stabilization speed. Solutions experiments in the range of 0mM to 5mM or 0mM to 40mM were iterated through, in randomized order, each 5-10 times. A current-concentration response curve is shown in Fig. 6.4 from measurement sweeps of two different wafer constructions: A spincoat type wafer (shown in blue) with an enzyme layer and electrode layer built in separate photolithography steps, and (shown in red) a 50nm sputter coated enzyme sensor with the sputter coat, enzyme layer, and electrode all deposited in the same photolithographic step. It is evident that the additional handling or possibly the calibration process passivates the platinum surface in comparison to current signals observed in Fig 5.11. The initial observed average and standard deviations of M-M parameters of the electrodes were:

	Uncoated GOx sensors	Pt Coated GOx sensors
K_M (mM)	1.98 ± 0.47	11.88 ± 0.99
I_{max} (nA)	57.85 ± 12.9	125.03 ± 13.2

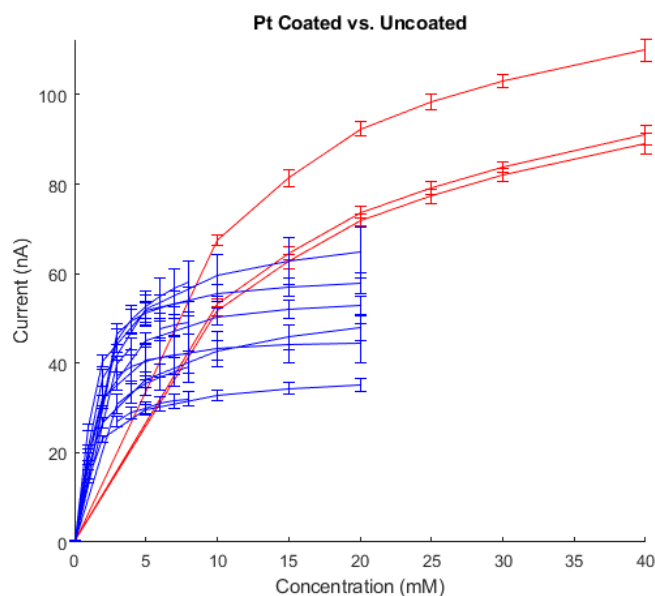


Figure 6.4 Comparison of sensor fabrication methods. (Blue) sensors were constructed with enzyme layers and electrode in separate steps, while (Red) sensors were combined construction and a 50nm sputtered platinum coat.

Integrating the enzyme layer and platinum electrode into the same photolithography step as described in the devices in Chapter 5 was observed to provide benefits, but it was also observed in trials that the vacuum and solvent processes improved K_M and linearity of sensors even without the platinum sputter coat. This is believed to be caused by dead enzyme layers at the top of immobilization layer acting partially as a diffusion barrier and permitting enzymes closer to the electrode surface to process a larger portion of the glucose. To that end wafers were constructed where all electrodes experience the same fabrication process except that a physical object occludes platinum landing on the enzyme layer during the sputter process. This the effects of the platinum coat itself may be more directly measured while controlling for other process effects. Figure 6.5 shows data from a wafer where electrodes 12 and 17 were topcoated with 200nm of platinum while electrodes 15 and 19 were uncoated. The observed M-M parameters of the electrodes were:

	Sensor 12	Sensor 17		Sensor 15	Sensor 19
K_M (mM)	14.25±0.04	11.18±0.03		1.99±0.01	1.49±0.01
I_{max} (nA)	113.75±0.01	141.45±0.01		116.03±0.01	98.62±0.01

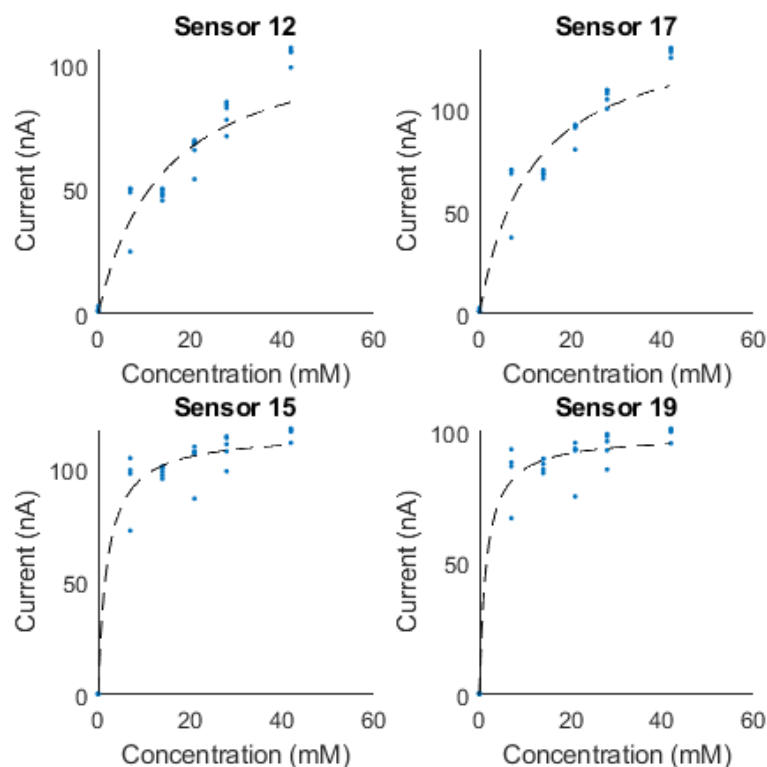


Figure 6.5 200nm platinum coated and uncoated sensors, wide concentration range. Sensors 12 and 17 were exposed to a 200nm platinum sputter deposition while sensor 15 and 19 were not coated.

Besides the full concentration range of the sensor we are also interested in the linearity of the sensor for calibration purposes. Glucose concentrations exceeding 20mM are unrealistic physiologically but the K_M control exhibited in Figure 6.5 demonstrates the capability of the topcoat to provide flux limiting for other enzyme and analyte combinations. Measurements were also focused on the realistic physiological glucose ranges in Figure 6.6. Sensors 12-13 on a wafer were coated with 200nm of Pt while sensors 14-16 on that same wafer were not. The linear regression errors were found to be:

	200nm Pt Coated Sensors	Uncoated Sensors	Spincoat Sensor Data from Sec. 5.7.2	Dropcoat Sensor Data from Sec. 5.7.2
R^2	$99.96 \pm 0.04\%$	$97.47 \pm 0.67\%$	$95.89 \pm 0.97\%$	$97.52 \pm 0.45\%$

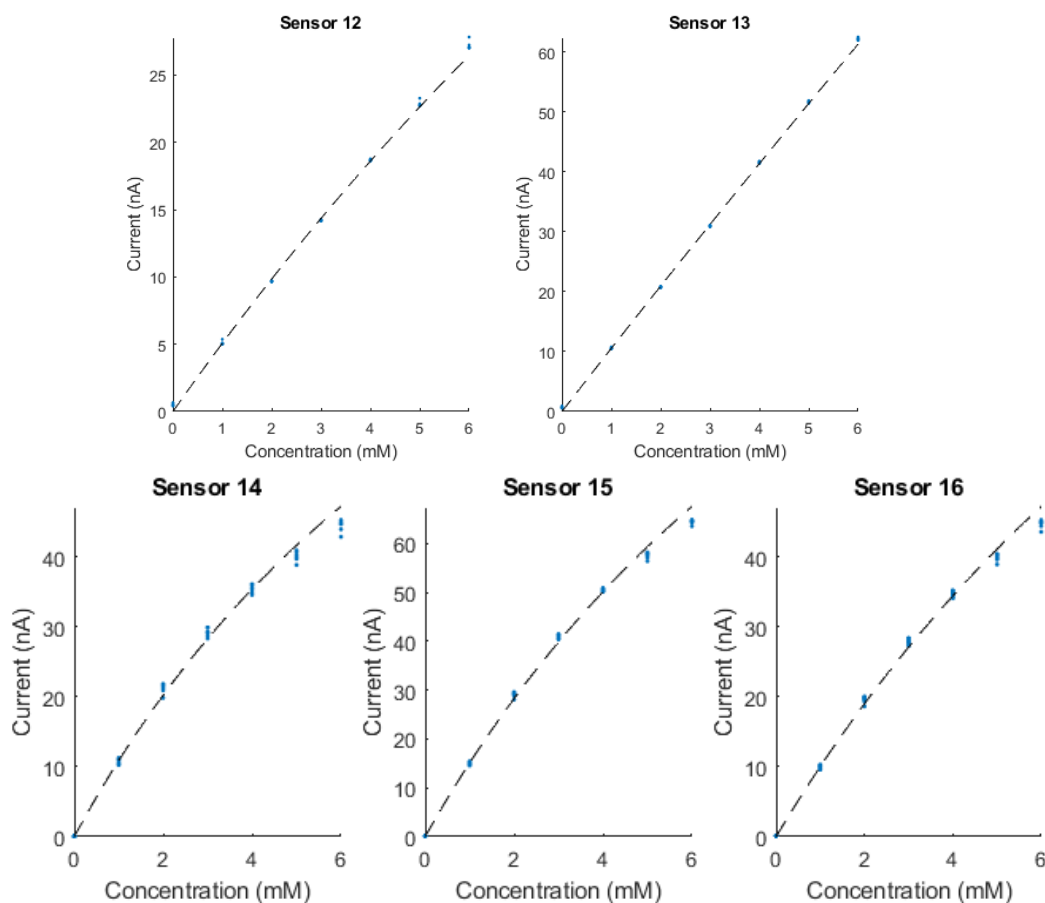


Figure 6.6 200nm platinum coated and uncoated sensors, narrow concentration range. Sensors 12-13 were exposed to a 200nm platinum sputter deposition while sensor 14-16 were not coated.

6.6.3 Sensor Lifetimes

To confirm our in vitro sensor lifetimes we have performed measurement sweeps over the course of 3 months. Fig 6.9. shows the slow drift of K_M and I_{max} during this time period. This sample utilized a 50nm platinum topcoat which was observed to be still fully adherent after the 3 month measurement period. No significant changes to the <5 second stabilization times examined in Section 5.7.3 were observed for these devices.

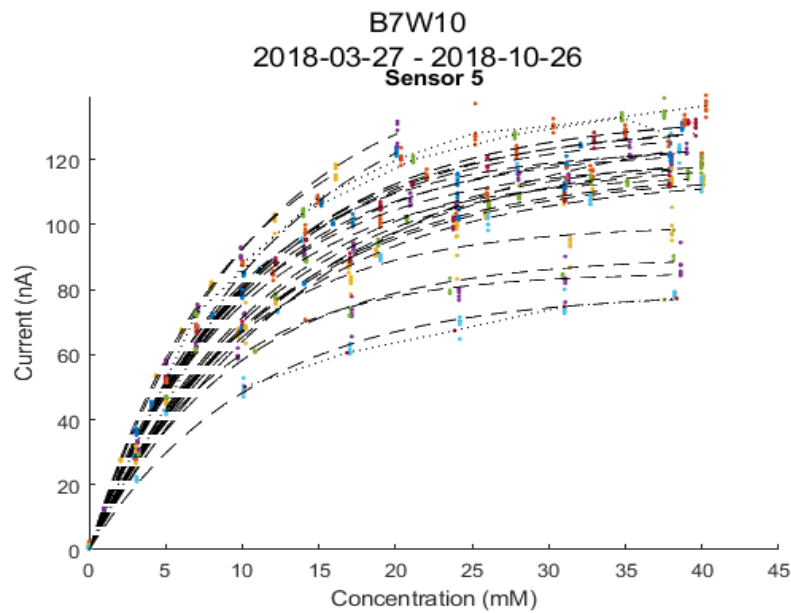


Figure 6.7 Example data for single electrode over 3 months. The lowest current signals were observed at the latest measurements dates as clarified in the following 2 figures.

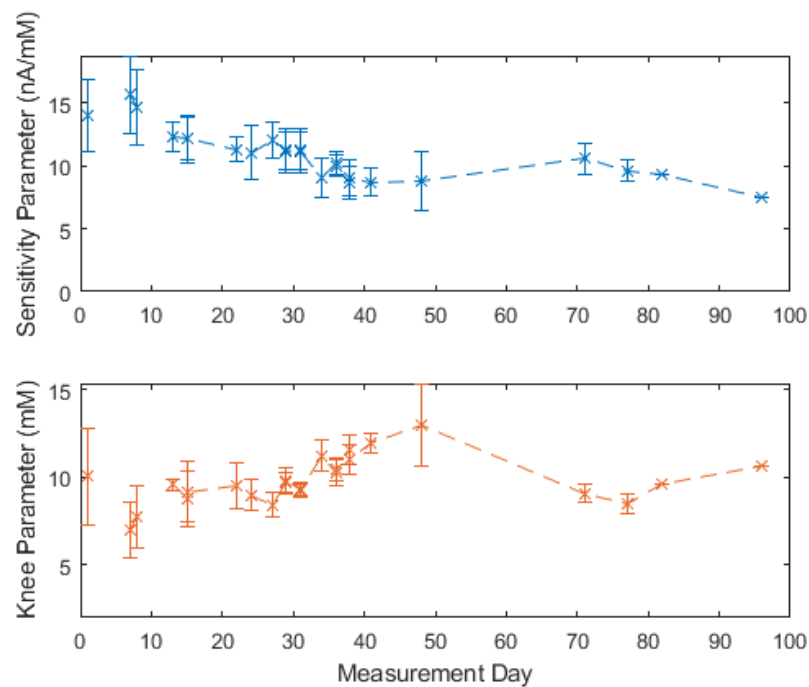


Figure 6.8 Sensitivity and exponential knee over 95 days of measurements averaged over 5 electrodes.

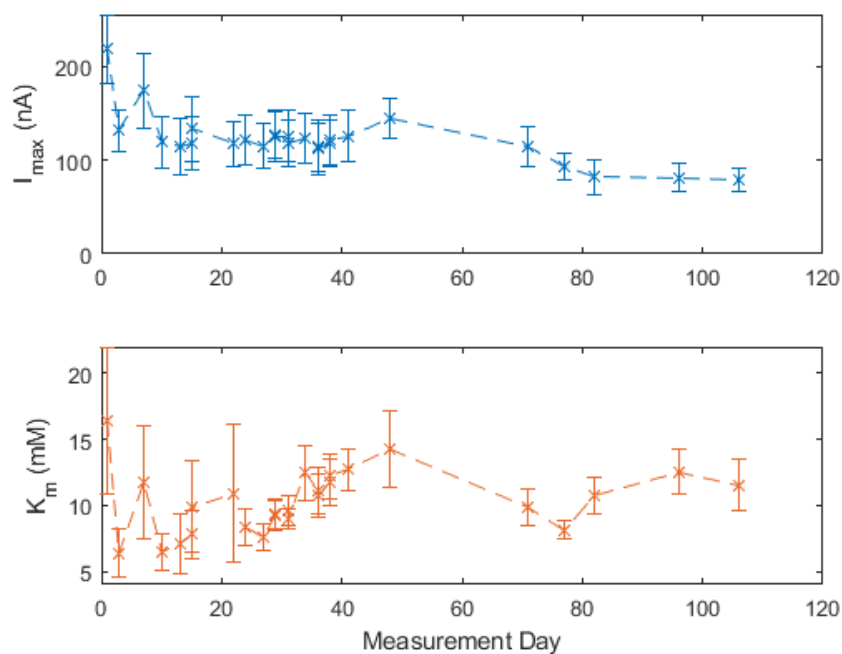


Figure 6.9 I_{\max} and K_M over 95 days of measurements, averaged over 5 electrodes.

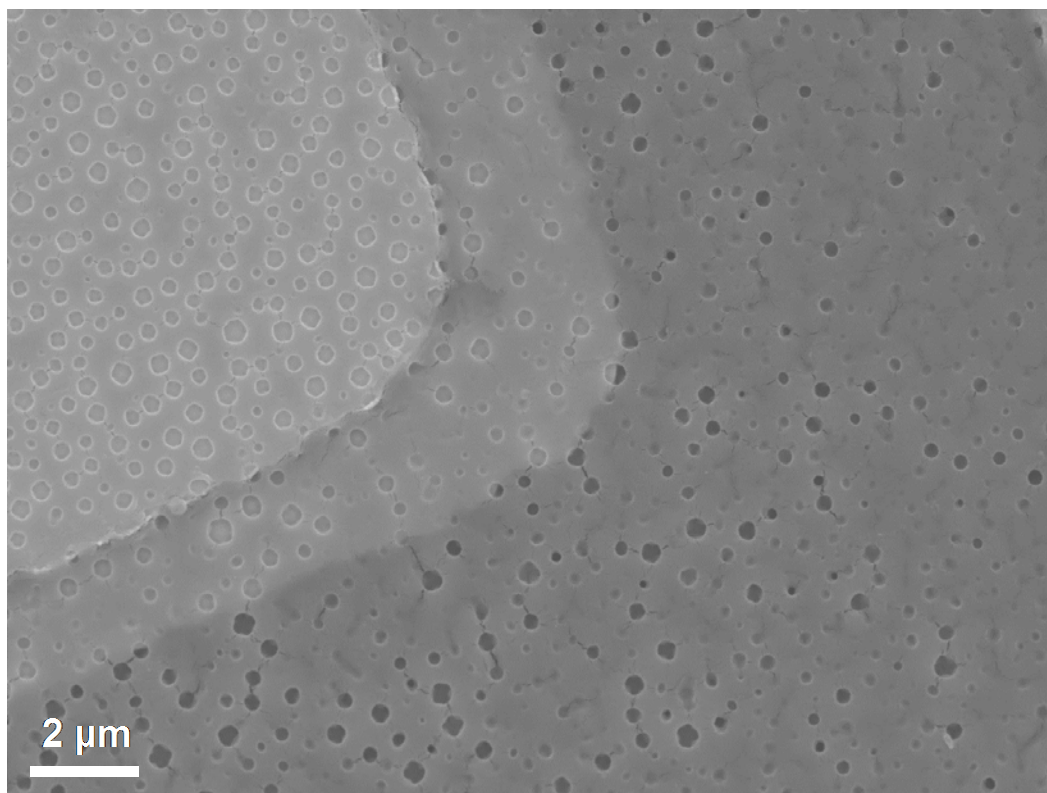
6.7 Discussion

Sputter deposited metal layers typically grow as nanocrystalline grains with a porosity controllable by the deposition parameters. Nucleation and growth of sputtered films is strongly influenced by the seeding surface onto which the material is deposited. The SEM images in Fig 6.10 show both the texture of the underlying enzyme polymer, and the granularity of the Pt sputtered on top, with a small grain size of 5-10nm typical of porous platinum. The porosity naturally modifies the diffusion coefficient, resulting in a morphology-dependent effective diffusion coefficient determined by grain size and constrictions. Analyte delivery can therefore be geometrically controlled and products can be chemically catalyzed more efficiently under a platinum topcoat. Oxygen diffusion, determining the oxygen concentration available to the enzyme layer, is reduced less than glucose diffusion with such a layer. Moreover, O_2 generated by the electrode and H_2O_2 catalytic oxidation process can be recycled to benefit the enzyme reaction with less bulk loss. Finally, the Pt surface also serves to react with any escaping H_2O_2 and incoming oxidizing species, thus potentially reducing crosstalk between adjacent electrodes and lowering potential damage from immune response. This H_2O_2

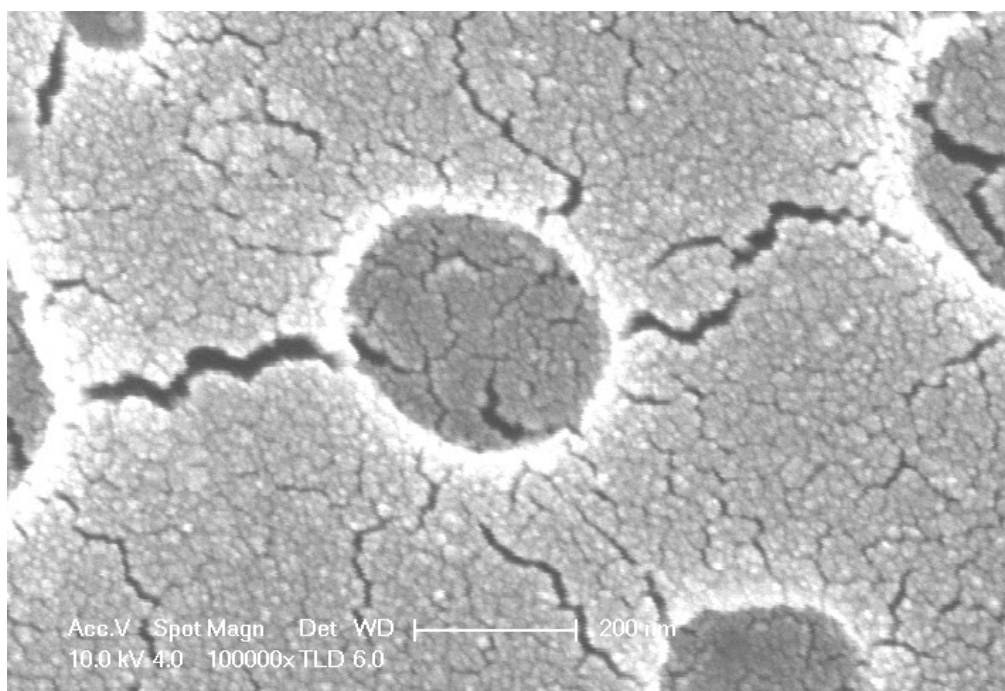
decomposition may act as a portion of the WE current when the polymer is porous enough to have cavities reaching from its top surface to the bottom electrode surface (examples visible in Fig 6.10). However, it is also possible to electrically separate the top platinum layer from the measurement electrode if an electrically insulating polymer is used below the Pt topcoat. Such a floating electrode may act as a catalyst for equilibrium reactions without influencing the functional Pt WE below.

Sputtered layers may also serve as a part of a more complex multi-layer as required by the particular measurement case. Platinum polycrystal films cannot match the same swelling behavior observed in polymers, but we expect that as the underlying polymer expands, the porosity of the Pt layer also increases. The fabrication process requires a high vacuum environment exposure step which dehydrates the enzyme polymer layer, but in our experience this step has not significantly degraded the subsequent enzyme functionality. It would be expected that the polymer would re-swell when introduced into the measurement solution, and this would determine the final porosity of the Pt layer. Since photolithography enables control of the Pt topcoat position, this may give more options for varied restrictive control on different electrodes of the same device substrate. Since this work was done with standard microfabrication photolithography and sputtering techniques, it is apparent there is a much larger window of microfabrication options for these sensors than we have had time to explore. The total exposure time to vacuum was approximately 30 minutes and exposure to solvent approximately 2 hours while still yielding high enzyme performance. Other inorganic materials that can be sputter deposited, such as gold and titanium, have yet to be explored, and combinations of such layers could lead to additional functionalities. The chemical function of a floating platinum layer as an additional controlling electrode in the electrochemical sensor system will also require further study.

a.



b.



c.

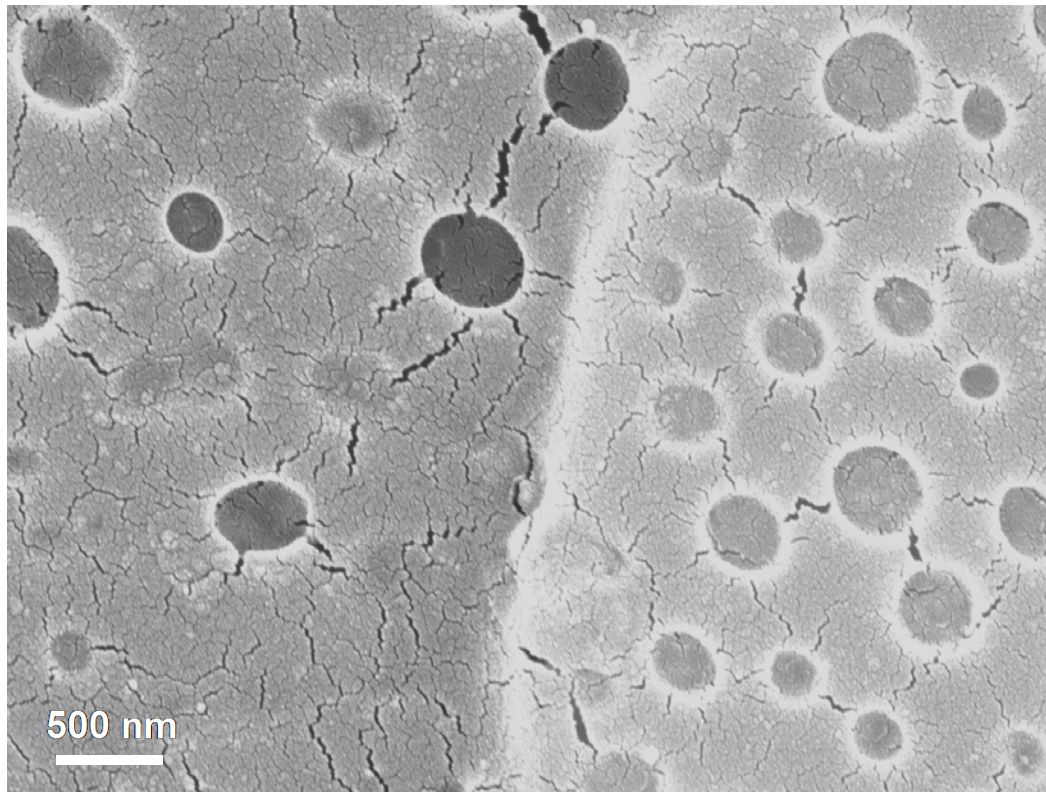


Figure 6.10 SEM images of a platinum sputter coat on top of an enzyme layer. The porosity of enzyme-polymer layer allows electrical continuity between the top layer platinum and the electrode below.

6.8 Concluding Observations

We have demonstrated the utility of sputter deposited metal layers as a method to extend the linear concentration range of enzyme-based electrochemical sensors. Vacuum processing and photolithography do not cause significant degradation of glucose oxidase enzyme performance. Combined with enzyme spin-coat techniques this sensor stack enables microelectronic wafer processing methodologies to provide the high fabrication uniformity and reproducibility needed for the mass production of continuous glucose sensors. The sensors demonstrated here provide high sensitivity, fast response times, and good linearity in the clinically relevant glucose concentrations. Platinum may also serve in the future as a good choice of biocompatible outer layer of a long term implanted glucose monitors.

References:

- [1] G. Wilson and R. Gifford, "Biosensors for real-time in vivo measurements", *Biosensors and Bioelectronics*, vol. 20, no. 12, pp. 2388-2403, 2005. Available: 10.1016/j.bios.2004.12.003.
- [2] M. Mujeeb-U-Rahman, M. Honarvar Nazari and M. Sencan, "A novel semiconductor based wireless electrochemical sensing platform for chronic disease management", *Biosensors and Bioelectronics*, vol. 124-125, pp. 66-74, 2019. Available: 10.1016/j.bios.2018.09.077.
- [3] T. Kulkarni and G. Slaughter, "Application of Semipermeable Membranes in Glucose Biosensing", *Membranes*, vol. 6, no. 4, p. 55, 2016. Available: 10.3390/membranes6040055.
- [4] H. Forman, A. Bernardo and K. Davies, "What is the concentration of hydrogen peroxide in blood and plasma?", *Archives of Biochemistry and Biophysics*, vol. 603, pp. 48-53, 2016. Available: 10.1016/j.abb.2016.05.005.
- [5] F. Moussy and D. Harrison, "Prevention of the Rapid Degradation of Subcutaneously Implanted Ag/AgCl Reference Electrodes Using Polymer Coatings", *Analytical Chemistry*, vol. 66, no. 5, pp. 674-679, 1994. Available: 10.1021/ac00077a015.
- [6] W. Van Antwerp, "Polyurethane/polyurea Compositions Containing Silicone for Biosensor Membranes", 5882494A, 1995.
- [7] K. Scholten and E. Meng, "Materials for microfabricated implantable devices: a review", *Lab on a Chip*, vol. 15, no. 22, pp. 4256-4272, 2015. Available: 10.1039/c5lc00809c [Accessed 22 May 2019].
- [8] J. Selvakumaran, J. Keddie, D. Ewins and M. Hughes, "Protein adsorption on materials for recording sites on implantable microelectrodes", *Journal of Materials Science: Materials in Medicine*, vol. 19, no. 1, pp. 143-151, 2007. Available: 10.1007/s10856-007-3110-x.

- [9] C. Dubois and C. Jorge, "Clinical utility of platinum chromium bare-metal stents in coronary heart disease", *Medical Devices: Evidence and Research*, p. 359, 2015. Available: 10.2147/mdir.s69415.
- [10] T. Mallat and A. Baiker, "Oxidation of alcohols with molecular oxygen on platinum metal catalysts in aqueous solutions", *Catalysis Today*, vol. 19, no. 2, pp. 247-283, 1994. Available: 10.1016/0920-5861(94)80187-8.
- [11] A. Schwartz, "Catalytic oxidation studies with platinum and palladium", *Journal of Catalysis*, vol. 21, no. 2, pp. 199-207, 1971. Available: 10.1016/0021-9517(71)90138-2.
- [12] V. Voorhees and R. Adams, "The use of the Oxides of Platinum for the Catalytic Reduction of Organic Compounds Part I," *Journal of the American Chemical Society*, vol. 44, no. 6, pp. 1397–1405, Jun. 1922.

Chapter 7 CMOS Sensor Fabrication

7.1 Overview

The overall effort of this research work is towards enabling enzymatic electrochemical biosensor fabrication on top of CMOS devices in a fashion that integrates with the inherently parallel wafer microfabrication of the CMOS platform. This would enable low-cost development of fully implantable-type subcutaneous sensors. Wireless CMOS potentiostats were developed in a collaboration effort and the prior silicon wafer sensor fabrication techniques were adapted to this new structure. The devices are initially designed with industry-standard aluminum contact pads that are then adapted via microfabrication processes to platinum electrodes. The CMOS device was designed to function with low wattage UHF RF power delivery and drive a stable potentiostat to the voltage and current ranges utilized in the prior wafer devices. Minimizing power consumption is critical due to tissue absorption losses [1], the goal of minimal antenna size, and the available q-factor of building an antenna in-plane in a copper layer of a CMOS circuit. The sensor system developed is powered by near-field RF coupling of an on-chip antenna to an external coil antenna at approximately 915 MHz. Configuration data is delivered via an RF downlink utilizing a PWM communication scheme, and a potentiostat current value is returned via RF backscattering. The prototype was fabricated by TSMC in their 65nm CMOS process with a total footprint of $1.2 \times 1.2 \text{ mm}^2$. The potentiostat was designed to operate up to 350nA, which exceeds the current values measured in vitro in Chapters 5 and 6, with a total power consumption of $4 \mu\text{W}$.

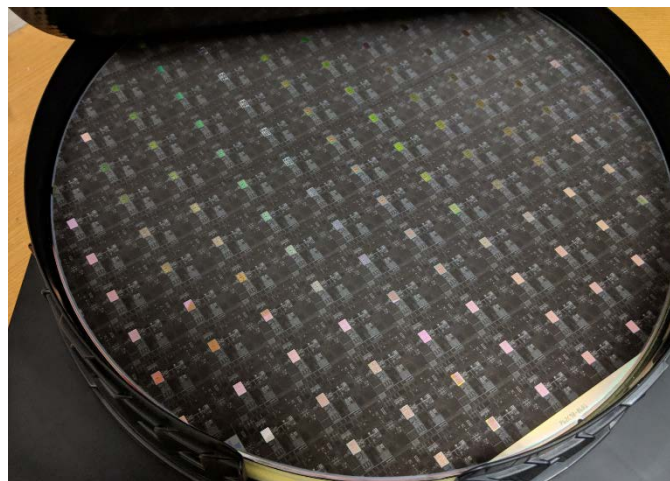


Figure 7.1 CMOS wafer containing approximately 120 dies.

7.2 CMOS Design

The goal of the design is to have a fully implantable footprint while performing critical potentiostat operations consistently. Observed measurement currents on the prior in vitro wafer tests were in the range of 0-300nA at the selected 0.4V bias. To allow future choice of electrode materials (and in turn interference reactions) it is preferable to have a selectable voltage bias and the chosen range was 0.2-0.6V. This WE-RE voltage, in addition to the WE-CE voltage, sets the minimum voltage gap the complete device must generate be able to drive the potentiostat and stably run the desired chemical reaction.

The CMOS device utilized a novel potentiostat architecture to maintain low measurement power while maintaining accuracy within the proscribed range. A typical potentiostat device may be built with shunt resistors measured by a transimpedance amplifier [2], however due to limited available voltage on an RF CMOS device, this method may require a voltage drop that hampers the potentiostat output voltage range. Another option are relaxation oscillators which convert the measurement current to a frequency by integrating the current into a capacitor which discharges when a threshold is reached [3]. However, increasing measurement current necessitates increased frequency operation which in turn requires unacceptable levels of power delivery. An All Digital Phase Locked Loop (AD PLL) was implemented instead which operates as follows. The input current is fed into the loop from a current mirror on the potentiostat. This is fed into the Digital Controlled Oscillator (DCO) which contains a digitally tunable capacitor (DTC). The end goal is that the DTC is tuned to help match a mild speed (32kHz) onboard reference oscillator, and thus the charging from input current only creates a phase shift compared to the reference. The output from DCO goes to a Phase-Frequency Detector (PFD) which gives an output pulsed signal dependent on the phase shift from a reference oscillator. This is fed to a Time to Digital Converter which converts the pulsed signal to a bit value. And this bit value is fed into the Digital Loop Filter, which cleans out the non-carrier frequency components from the PFD operation and the resulting output DTC setting is fed to uplink system (as the measurement value), and fed back as the control value for the DTC so it is adjusted to maintain that near 32kHz oscillation. Thus completing the PLL. These components were all designed in relatively low voltage digital logic without much demand on circuitry footprint [4].

The system is powered by a two-turn on-chip coil patterned into the top copper layer of the CMOS process. It is designed for maximum power transfer

efficiency from a 1.5 cm external reading antenna located 1cm away. The antenna is designed for ~ 20 q-factor and provides 1.2V DC power to the device via full wave rectification. A low-dropout regulator is used to provide a stable load current.

7.3 Electrode Fabrication

Post-processing on top of completed foundry CMOS material presents unique challenges not present on virgin silicon wafers. The CMOS device top structures consist of passivation layers made from materials such as silicon nitride and silicon dioxide and aluminum contact pads intended for wirebonding. The material is purchased in full wafer form but only a portion of the die map is allocated to our particular project so the rest of the surface is ‘RIP’ (removal IP) processed by laser ablating structures designed by other customers. Both the die and RIP regions have significant amounts of terrain beyond that typically tolerated for high resolution spincoat lithography. In addition, the RIP regions shed molten silicon/metal material frequently.

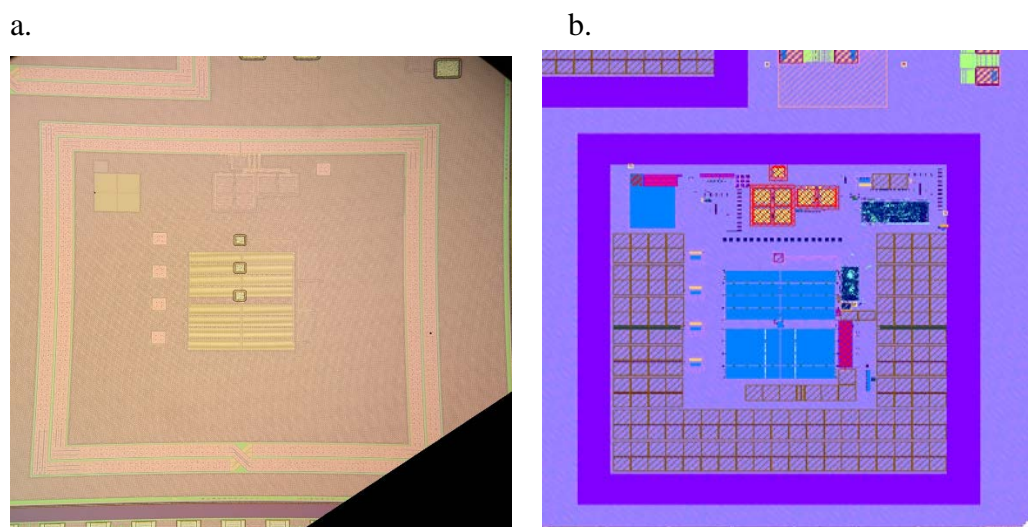


Figure 7.2 Individual CMOS potentiostat device. (a) optical image of top layer (b) GDS design layout. Antenna loops are 1.2mm wide.

Three aluminum contact pads for the WE, RE, and CE of dimension $30\mu\text{m} \times 30\mu\text{m}$ are designed centered within the antenna region (See Fig 7.2a). The completed device is meant to have three, much larger, platinum electrodes built on top of these contact pads with a similar geometry to the wafers devices. The first obstacle observed is that the aluminum bond pad material is highly reactive in PBS,

and even more so when under voltage bias, such that any diffusion access to the aluminum causes heavy corrosion. Few deposition processes guarantee pinhole-free layers so alternative steps were followed to circumvent direct ionic solution exposure. A process was developed to completely etch away the aluminum material, build contacts to the lower layer device, add additional passivation to protect the pad regions, and then build final platinum and GOx coated electrodes. The fabrication recipe is depicted in Figure 7.3, the steps are listed below, and the justifications for choices made described immediately afterwards.

1. CMOS wafer is scribed or sawed from 300mm down to 1-9 die chips.
2. Chips are placed in Aluminum Etch Type D for 12minutes at 40C and rinsed (Fig 7.3b)
3. Bond pad lip structures are removed by physical abrasion. (Fig 7.3c)
4. Chips are placed in acetone sonication to remove RIP debris and organic contamination.
5. Dependent on the particular chip design, an SF₆/C₄F₈ based etch is used to access buried metal traces below the passivation surface.
6. Photoresist patterning is performed using a thicker photoresist than the wafers, AZ nLoF 2070.
7. Sputter deposition of 200nm Ti, 100nm Pt (Fig 7.3d)
8. Acetone liftoff
9. PECVD deposition of 1000nm of SiO₂ (Fig 7.3f)
10. Photoresist patterning and SF₆/C₄F₈ etch to form access vias shifted from the original pads. (Fig 7.3g)
11. Photoresist patterning with AZ 5214-IR for a final metal layer
12. Sputter deposition of 100nm Ti, 200nm Pt.
13. Spincoat GOx as described in Chapter 5. (Fig 7.3h)
14. Optional platinum topcoat as described in Chapter 6.
15. Acetone liftoff
16. Devices are diced to their final dimension of 1.2x1.2 mm² and edges are sealed with biocompatible epoxy.

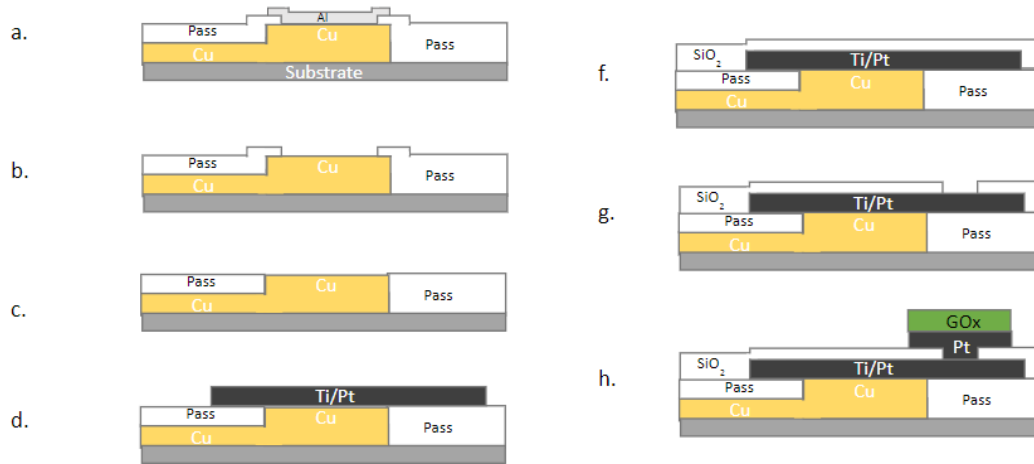


Figure 7.3 CMOS device post-processing recipe summary.

The CMOS foundry fabricates wafers at the 300mm scale for material cost efficiency reasons. The increased number of completed dies built per wafer justifies the increased equipment costs and 300mm wafers have become a common foundry scale format. For our fabrication purposes we must immediately partition this sample to smaller amounts of dies from the initial ~120, both because the recipe development process must consume individual samples, and because no research-grade microfabrication equipment can accept samples of this scale.

Aluminum Etch Type D was chosen as it has a relatively slow etch speed against the copper traces below the aluminum bond pad thus preventing undesired circuit damage. It is also a compatible chemical with the passivation layers of the device. This process alters the bond pad region as elucidated in Figs 7.4-7.6.

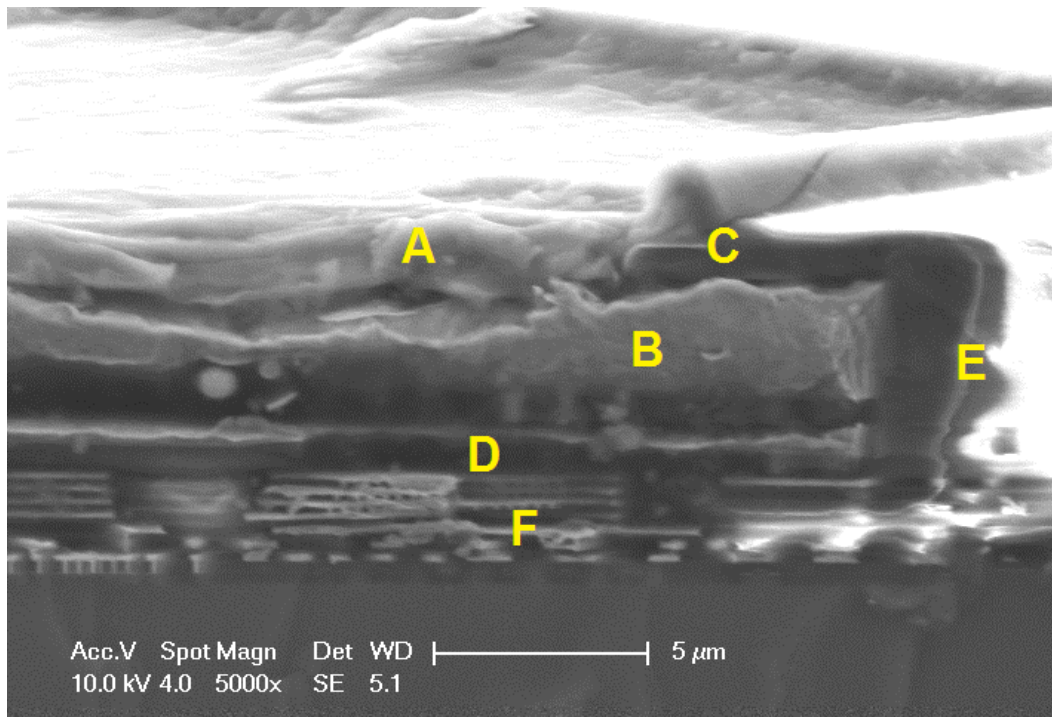


Figure 7.4 Cross-section view of aluminum bond pad. One of the three aluminum pads is visible. Layer A is the aluminum pad material. Layer C is a barrier lip composed of Si₃N₄ intended to constrain wire bond material during the wirebonding process. Layer B is the copper trace below the aluminum pad. Layer D is a passivation layer between the pad and layer F where additional circuitry lies which is not interfaced directly vertically with the pad. Layer E marks the rest of the passivation layer across the device (~4μm thick) where the contact pads are not present.

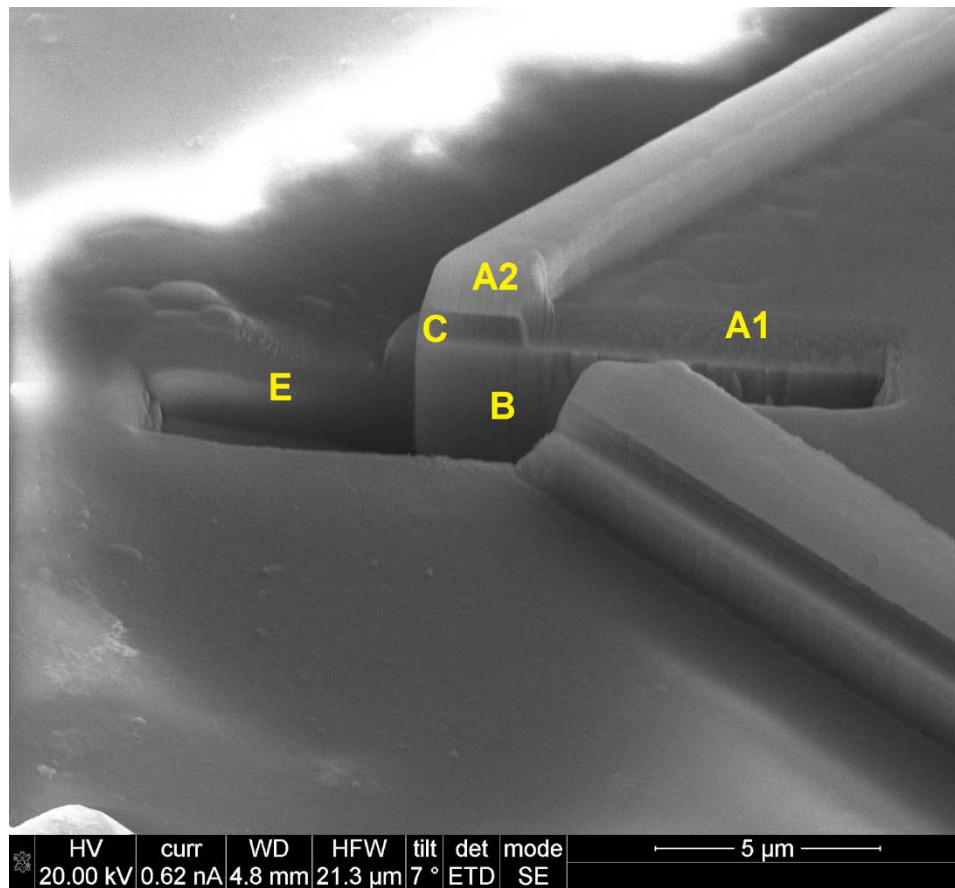


Figure 7.5 A cross-section FIB cut of 1 of the 3 aluminum pads. Areas marked A1 and A2 are aluminum pad material. Layer C is the barrier lip. Layer B is the copper trace. Layer E marks the rest of the lateral passivation layer across the device.

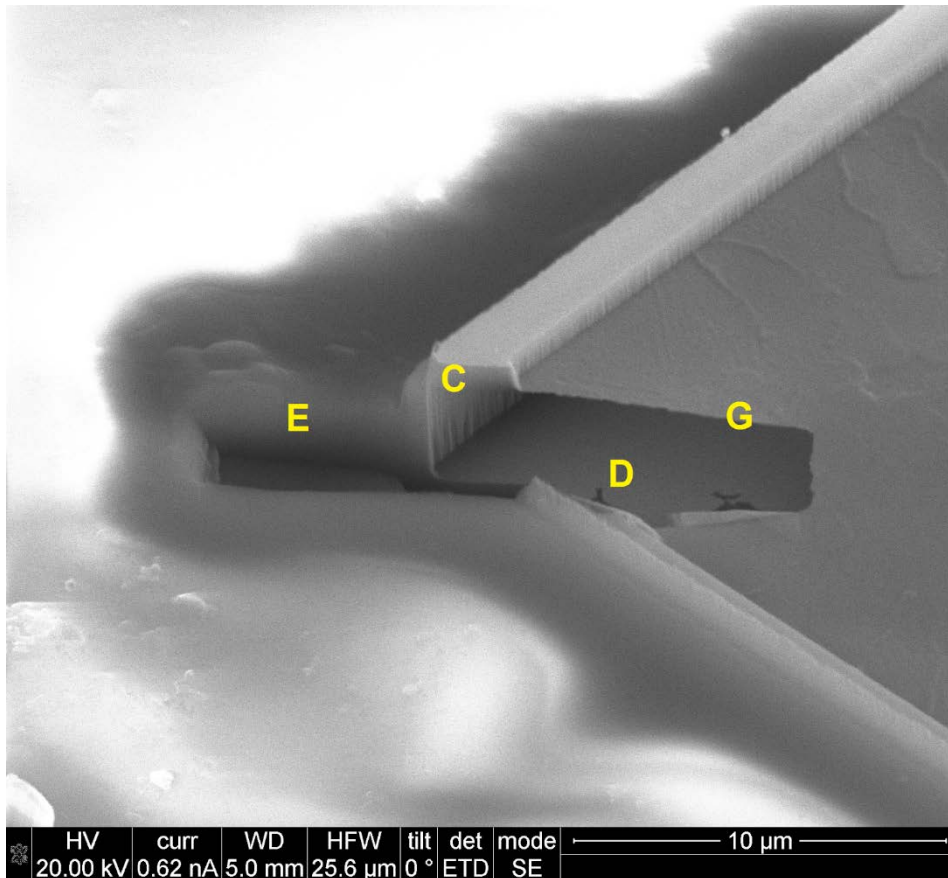


Figure 7.6 Cross-section FIB cut after etching with Aluminum Etch Type A. Layer C is the barrier lip. Layers A and B of aluminum and copper are etched away in this instance. Layer E marks the rest of the lateral passivation layer across the device. Layer D is the bottom passivation layer of the pad. Layer G is a TaN diffusion barrier between the Al and Cu which was not affected by the wet etch. Typically, the structure is not undercut during etching because the FIB access hole is not present.

Thick ($\sim 7 \mu\text{m}$) photoresist is used despite lateral accuracy losses due to the terrain created by the RIP processing, the bond pad structures, the necessary metal layer liftoff thicknesses (to reduce sublayer corrosion speeds), and the depth of passivation etches needed for circuit corrections. The lip structures are often removed because they cause difficulty in building a continuous metal contact of platinum between the outer lateral region and inner pad well structure. Most deposition processes are not conformal enough to guarantee continuity otherwise. This removal step is performed via mechanical abrasion with a swab. Afterwards the chips are thoroughly solvent cleaned to remove as much debris from the surface as possible to ease the following 4 photoresist processes.

Sputter deposition of platinum layers is performed instead of platinum evaporation, as in the wafer devices, to improve coverage of the uneven surfaces. We have not found significant difference in chemical properties between the two deposition methods. Thick layers of Ti are used as filler to reduce Pt consumption. Ti passivates to TiO_2 which is stable in most environments but corrosion can begin if PBS ions reach unpassivated Ti regions.

An additional passivation layer is built to laterally shift the electrode vias away from the original contact pads. This forces any corrosive particles to travel both vertically hundreds of nanometers, and laterally several microns through pinholes, along grain boundaries, or layer interfaces, thus reducing time to corrosion failure. Access vias are made with an SiO_2 plasma etch.

Final sputter deposition of a thick platinum layer is made to protect the lower circuit layers, and the standard GOx and/or sandwich structure process follows. The entire device is then protected in unbaked photoresist prior to being sent to a silicon wafer dicing service. A complete device before dicing is shown in Fig 7.7a.

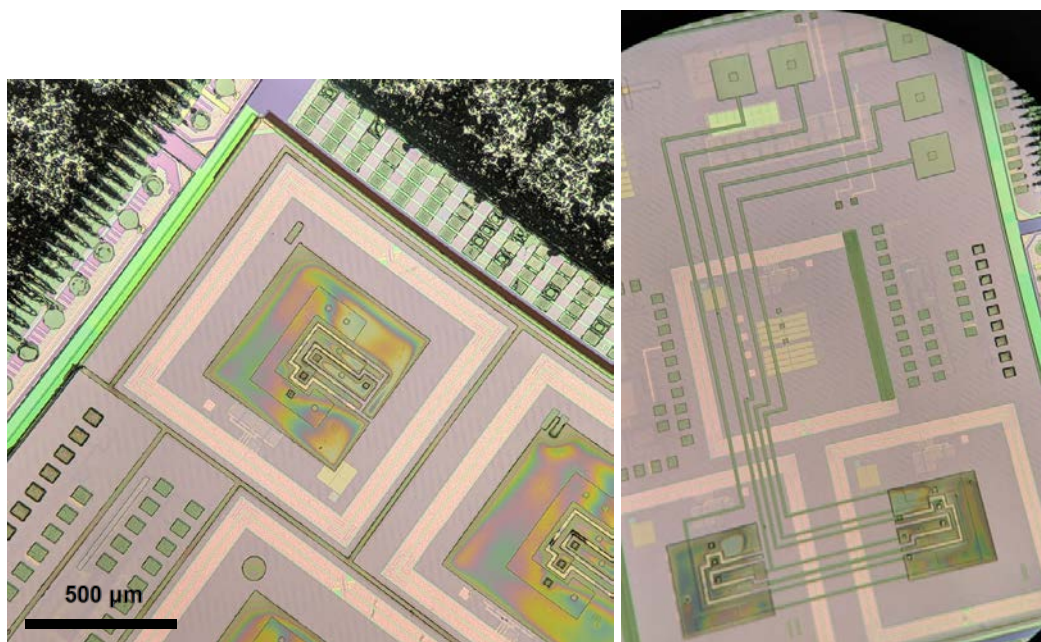


Figure 7.7 Completed CMOS device with platinum electrodes and GOx layer. (a) The dicing process follows the square region around the antenna. (b) test structures for direct probing the electrodes while under RF power. Antenna loops are 1.2mm wide.

Since the information relayed and controls available for the electrodes are limited by the RF CMOS subsystem, test structures were also built to physically probe the electrodes. This allowed a wider voltage monitoring and control range and AC options not available in the CMOS hardware. These devices were operated via RF power, the electrodes were immersed in glucose solutions, and traces to the electrodes were monitored by an electrometer.

These planar electrodes match the footprint and surface area of the planar wafer electrodes of the previous chapters. As with the silicon nanopillar etching techniques discussed in Chapter 5, the terrain of the CMOS device can be increased by alteration of the device factory design. Figs 7.8 and 7.9 show a periodic pattern of passivated structures which are specified to the foundry as an alternative construction of the aluminum bond pad. The aluminum and copper may then be etched down to expose the pillar structures, which are then sputter coated in the final electrode material (e.g., platinum).

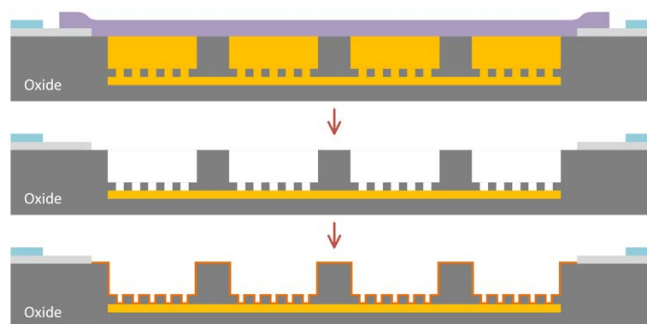


Figure 7.8 Cross-section diagram of the bond pad structure specified to the foundry.

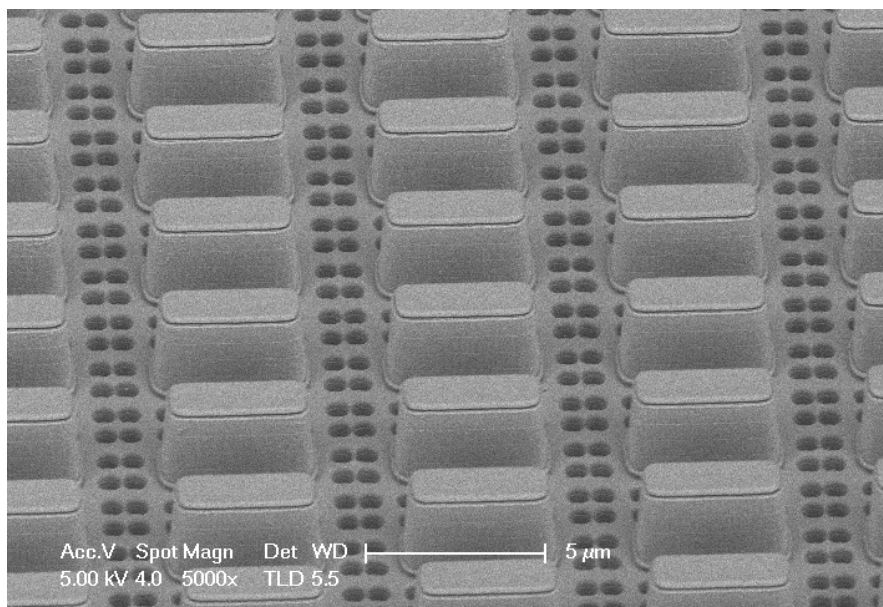


Figure 7.9 CMOS contact pad chemically etched down to passivation structures.

7.4 In Vitro Evaluation

The fabrication complete devices were evaluated in test PBS/Glucose solutions similar to as described in the previous 2 chapters. Probing is simplified since the device can communicate wirelessly through a glass beaker but required new RF interface software to be developed. The voltage was selected at +0.4V over a platinum reference as described in the prior chapters. Returned current values were evaluated for M-M behavior.

Glucose solutions in 1X PBS (0.1% sodium benzoate) of clinically relevant concentrations (0-50 mM) were prepared in separate vials of volume much larger than the device, and the device was transferred between vials left at room temperature for each measurement. Devices were iterated throughout the solution set in random order after 50-70seconds of measurement bias time, and 3-5 minutes of total immersion time. From the continuous readings, data points were selected at 2s, 8s, 32s, and a final under-bias value. Error on the measurement time is approximately 0.1 seconds due to occasional RF link loss. One or two concentration sweeps was performed per device, and uncertainty in the solution concentrations or instantaneous current measurement were much lower than the residual errors. Devices were stored in PBS when not being used for measurements.

Fitting parameters were again obtained via Matlab for the saturation behavior of each sensor. Michaelis-Menten analysis for the ‘apparent’ coefficients K_M and electrical current I_{\max} determined via the Lineweaver-Burk method are given below. Previously described exponential fit parameters from Chapter 3 are given as well to provide a comparison to the wafer devices. Three CMOS sensors were evaluated and given in Table 1, for brevity a plot of only 1 sensor is provided in Figure 7.10.

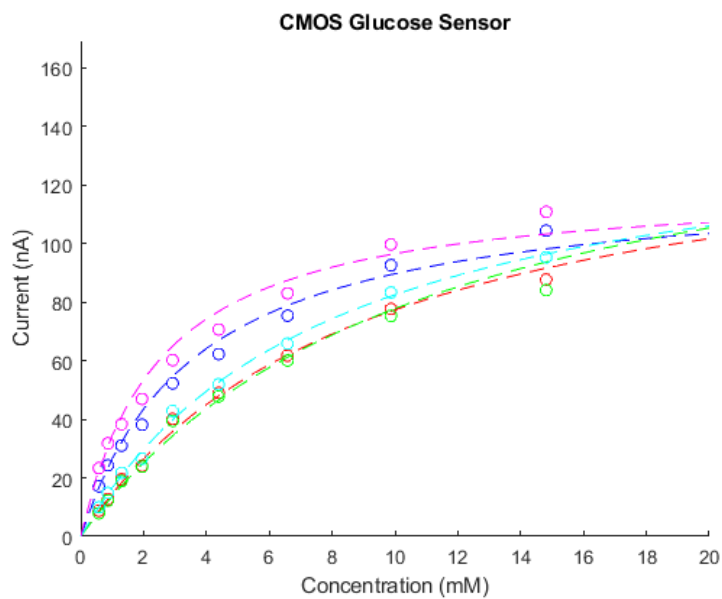


Figure 7.10 CMOS glucose measurement with K_M fit curves. (Magenta): Turn-on time, (Blue) 2 seconds, (Cyan): 8 seconds (Red): 30 seconds (Green): Final time.

	Time	Sensor 1		Sensor 2 Day 1	Sensor 2 Day 4
K_M (mM)	Turn-on	0.5 ± 0.3		1.8 ± 0.3	2.5 ± 0.3
	2s	1.1 ± 0.3		3.5 ± 0.7	3.6 ± 0.5
	8s	2.2 ± 0.5		7.1 ± 1.6	7.9 ± 1.4
	30s	2.7 ± 0.4		8.6 ± 1.3	9.1 ± 1.5
	Final	1.8 ± 0.4		8.1 ± 2.3	10.9 ± 3.3
I_{max} (nA)	Turn-on	65 ± 11		138 ± 16	120 ± 17
	2s	54 ± 9		131 ± 25	122 ± 18
	8s	52 ± 8		163 ± 21	148 ± 24
	30s	52 ± 6		163 ± 19	148 ± 36
	Final	45 ± 8		149 ± 33	163 ± 41
κ_p (mM)	Turn-on	1.1 ± 0.4		4.1 ± 0.7	5.6 ± 0.8
	2s	2.3 ± 0.7		5.9 ± 1.1	6.9 ± 1.1
	8s	4.0 ± 1.1		6.7 ± 0.9	8.7 ± 0.8
	30s	3.8 ± 1.3		6.2 ± 0.8	8.4 ± 0.7
	Final	3.9 ± 1.2		6.1 ± 0.8	8.2 ± 0.8
Sensitivity (mA)	Turn-on	57 ± 22		36.6 ± 5.5	23.4 ± 3.1
	2s	23 ± 9		22.3 ± 4.5	18.6 ± 4.2
	8s	13 ± 5		18.9 ± 4.2	14.3 ± 2.7
	30s	12 ± 4		17.9 ± 4.1	13.4 ± 2.2
	Final	12 ± 4		17.3 ± 2.2	13.2 ± 2.1

Table 7.1 CMOS in vitro measurement parameters

From the parameters evaluated in Table 7.1, we can observe some efficiency loss in comparison to the 100mm wafer process (See Table 7.2). An additional process step that may have introduced this degradation is the (1.2mm) dicing process as that does not occur with the 100mm wafers. A outside commercial service is utilized for this task and the device undergoes an additional photoresist coating, commercial transit, and water spraying from the dicing saw tool, before being returned and acetone soaked to remove the photoresist coating.

	K_M^{app} (mM)	I_{max} (nA)
Spincoat Wafer Process (Day 1 @60s)	5.14±0.26	256.0±34.1
CMOS Sensor 2 (Day 1 @50s-70s)	8.1±2.3	149±33

Table 7.2. Spincoat wafer to CMOS device comparison. A variance is given for the wafer over 7 electrodes.

These devices were built without any filtering topcoat such as the sputtered platinum described in Chapter 6 and as such will reach their glucose enzyme saturation level faster. The saturation level may have been lowered due to increased enzyme death prior to measurements caused by the aforementioned dicing process.

7.5 In Vivo Considerations and Future Work

The completed CMOS devices were implanted within mice by collaborators at Dartmouth University in preliminary feasibility evaluations. Tissue compatibility with the materials and geometry of the device is of primary concern before further efforts are made in developing sensor functionality. Biocompatibility failure that results in complete protein encapsulation of the device would negate the purpose of constructing long-lifetime analyte sensors.

Fig 7.11. Examines the tissue response of the liver to a bare silicon CMOS device without additional biocompatible coatings. The higher density edges created correspond to the insertion damage and immune response of the body. Although increased protein and cell density are visible there is little apparent necrosis and the affected region extends less than 50 μm , which is a positive sign that analyte diffusion is still possible.

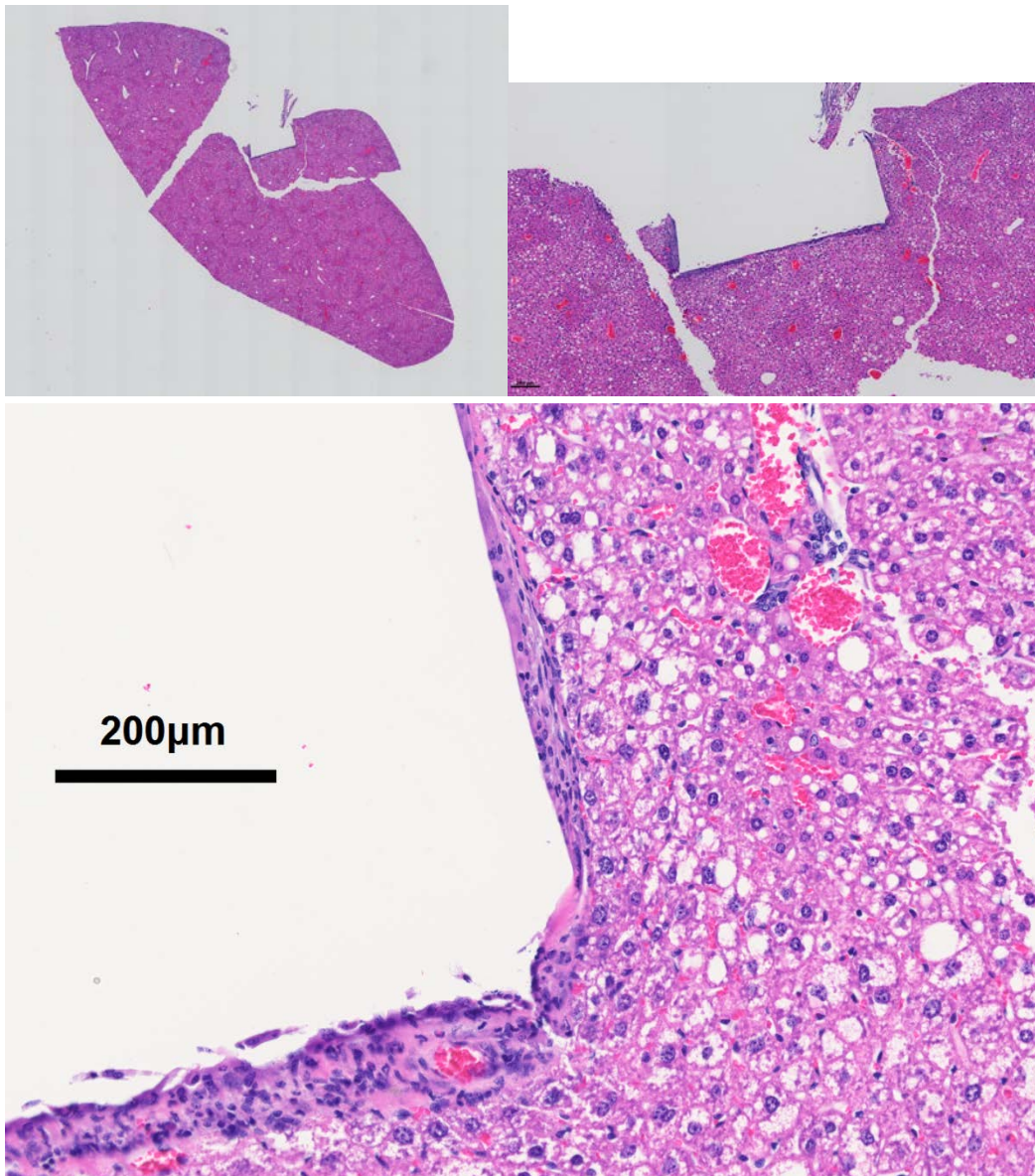


Figure 7.11 Examination of tissue response after 12-month CMOS device implantation.

Observed tissue response has looked positive for the functionality of the device following the considerations covered in Chapter 3. The RF communications components of the devices were verified to still be functional after 12 months of implantation indicating significant dissolution of the device did not occur. The methodology described in Chapter 6 could provide increased K_M and linearity due to diffusion impedance for the CMOS devices, but would suffer in vivo from

placing electroactive platinum at the outer boundary of the device which is wired to the electrodes. The platinum topcoat would need to be separated from the lower electrode by a non-conducting polymer or a separate interference screening layer would need to be placed on top. Further development of these polymers remains as a research extension to enable in vivo measurements. Iterations on the CMOS potentiostat may be made as well to improve the voltage range and control of the device. The final effect of encapsulation on analyte availability will have to be determined after temporary in vivo function is observed.

References

- [1] A. S. Y. Poon, S. O'Driscoll and T. H. Meng, "Optimal Frequency for Wireless Power Transmission Into Dispersive Tissue," in *IEEE Transactions on Antennas and Propagation*, vol. 58, no. 5, pp. 1739-1750, May 2010. doi: 10.1109/TAP.2010.2044310
- [2] C. Mc Caffrey, J. Doyle, V. Ogurtsov, K. Twomey and D. Arrigan, "Development and Evaluation of an On-Chip Potentiostat for Biomedical Applications", 2010, pp. 103-107.
- [3] M. H. Nazari, H. Mazhab-Jafari, L. Leng, A. Guenther and R. Genov, "CMOS Neurotransmitter Microarray: 96-Channel Integrated Potentiostat With On-Die Microsensors," in *IEEE Transactions on Biomedical Circuits and Systems*, vol. 7, no. 3, pp. 338-348, June 2013. doi: 10.1109/TBCAS.2012.2203597
- [4] A. Agarwal *et al.*, "A 4 μ W, ADPLL-based implantable amperometric biosensor in 65nm CMOS," *2017 Symposium on VLSI Circuits*, Kyoto, 2017, pp. C108-C109. doi: 10.23919/VLSIC.2017.8008566

Chapter 8 Concluding Remarks

Biosensor technology has progressed rapidly through many analytes, transduction mechanisms, and form-factors over the past decades. This work sought to extend these capabilities and contribute practical methods to biosensor research efforts to take increased advantage of microfabrication technologies [1]. Micro- and nanotechnology methods have enabled material fabrication at scales proportional to cells and even molecules and hence holds promise as an enabler of novel solutions for sensing our biological properties that operate at this scale. To further mesh technology with the human body we must be able to control all aspects our devices at these scales. Additional benefits beyond performance are gained with microfabrication since construction at these scales greatly reduces costs and physical impact of sensors in regards to analyte volume requirements and power consumption. Top down microfabrication utilizing spin-coating, photolithography, metal/insulator/polymer layer depositions have been developed over 70 years of semiconductor engineering and vast arrays of tooling are available both in the research laboratory and industrial settings. These may be taken advantage of to permit complete sensor construction at scales not previously considered since control electronics, communications, and the sensing elements can be reduced to sub-mm scales. The end goal for many health management concerns is to have consistent analyte monitoring and miniaturized sensors enables fully implantable end solutions. Current technology for glucose sensing causes chronic injury to patients which can hopefully be avoided in the future. By minizaturing this technology we would like to enable the long term meshing of the human body with observational electronic systems which may also one day provide feedback to active health maintenance devices such as those sought in artificial organ research.

After recipe development and numerous trials evaluating various properties of our enzyme sensors it is evident to us that consistent sensor fabrication between devices on single substrate and between substrates is possible, even though this goal was not always met due to the hands-on nature of research-scale microfabrication. Industrial tooling does not suffer from these same flaws. Spin-coat processing can be performed with much higher degrees of control in mechanized tooling than the manual handling required in the laboratory, so variances there can be further reduced. All of the devices in this work have focused on glucose oxidase enzyme as the main novel component of the microfabrication process and it is hoped that this can extend to other enzyme applications. The successful function of these thin coatings should prompt questions about the necessary amount of enzyme in all such sensors. The observations of compatibility of the enzyme with long term

acetone liftoff processing and vacuum sputter coating should also question the types of novel processing applicable to enzymes. And metal topcoat processing has created an unexpected form of enzyme product collection not achieved with existing methods. Comparative electron capture efficiencies requires unique enzyme binding chemistries that are nontrivial to develop, as in third generation glucose sensing devices [2]. Platinum has long served as a biocompatible electrode and stent material and it remains to be seen how it will fare as in vivo enzyme protection layer. Sputtering controls enable simplified selection of platinum layer thickness, grain size, and purity not typically available in topcoat construction. Further applications with different sputter depositable metals or insulators warrants exploration.

Biosensor construction and theory crosses such a variety of disciplines it can be difficult to analytically evaluate all sensor components and their interplay obscures which parameters are the weakest links. Building numerical simulations allowed greater intuition of the interplay of enzyme layer thickness and sensed currents but it is not possible to account for the variety of in vivo effects that will eventually be present in sensor application. Simulations cannot inform on the long term behavior of such sensors as they degrade, but increased understanding of in vitro results can result in improvements of the base device operation. Mathematical evaluations enable determinations of variables experimentally difficult to ascertain such as the functional enzyme fraction post fabrication.

Microfabricated CMOS-scale sensors would enable construction of low tissue-impact biosensors for implant purposes for diseases requiring continual analyte measures as with glucose for diabetes. We have demonstrated prototype operation of such sensors in vitro by translating our wafer-developed processes to CMOS devices. These enzyme layers allow rapid (sub-second) measurements which is critical to reducing total energy consumption of such sensors which must be minimized as the final devices are to be compact, wireless and function long term. Overall we have observed functional biosensor K_M and sensitivities with multi-month lifetimes for in vitro silicon wafer devices and demonstrated these capacities may translate to CMOS devices in parallel fabrication. Obstacles remain to the in vivo operation of such devices, which will be explored further by the research group. The biocompatibility of the sputtered topcoats will need to be observed and the function of them with or without additional polymer layers remains to be seen. The final effect of encapsulation on analyte availability will have to be determined after temporary in vivo function is observed.

The most fruitful observations from this work may be: novel glucose sensor structures are possible due to the compatibility of glucose oxidase to microfabrication

processes, microfabrication scale layers can have fine-tuned performance meeting or exceeding existing sensor designs, and complete biosensor construction from microfabrication methods may be possible. Biosensors hold great promise in both increasing our understanding of biological systems such as ourselves, and enabling health management for many ailments of our bodies. As such it is hoped this work has enabled further development of this beneficial technology.

References

- [1] A. Hierlemann, O. Brand, C. Hagleitner and H. Baltes, "Microfabrication techniques for chemical/biosensors", *Proceedings of the IEEE*, vol. 91, no. 6, pp. 839-863, 2003. Available: 10.1109/jproc.2003.813583.
- [2] E. Csoeregi et al., "Design, Characterization, and One-Point in vivo Calibration of a Subcutaneously Implanted Glucose Electrode", *Analytical Chemistry*, vol. 66, no. 19, pp. 3131-3138, 1994. Available: 10.1021/ac00091a022.

Appendix A: Fabrication Recipes

A. Resists:

AZ nLoF 2070:

1. Spin: 500rpm, 5 seconds, 2500rpm, 30 seconds
2. Hotplate Bake: 110°C, 90 seconds
1. Exposure: 12sec, Suss 1, Channel 1 (15mW/cm²)
3. Post-Exposure Bake: 110°C 90sec
4. Development: AZ 726, 2 minutes

AZ 5214-IR:

2. Dehydrate wafers: 150C, 5min
3. Spin: 500rpm, 5 seconds, 2000rpm, 30 seconds
4. Hotplate Bake: 110°C, 1min
5. Exposure: 12sec, Suss 2, Channel 2 (15mW/cm²)
6. Hotplate Reversal Bake: 110°C. 1min
7. Flood Exposure: 40sec, Suss 2 Channel 2 (15mW/cm²)
8. Development: MF 319, 90sec

AZ 9260:

1. Spin: 500rpm, 5 seconds, 3000rpm, 30 seconds
5. Hotplate Bake: 110°C, 2:45min
9. Exposure: 100sec, Suss 2, Channel 2 (15mW/cm²)
6. Development: MF 319, 12 minutes

PMMA 950 A4:

1. Spin: 500rpm, 5 seconds, 3000rpm, 30 seconds
2. Hotplate Bake: 180°C, 5min
3. Dose: 1100-1200uC/cm² for silicon
4. Development: MIBK:IPA 1:3, 60sec

ma-N 2403:

1. Spin: 500rpm, 5 seconds, 3000rpm, 30 seconds
2. Dose: 225-275uC/cm² for silicon
3. Development: MF 319, 70-80sec

B. Sputtering:

Custom Vacuum Chamber with 2" MeiVac Inc MAK Sputter sources

Titanium and Platinum Base Layers:

1. Base Pressure: 5×10^{-6} Torr
2. Operating Pressure: 5×10^{-3} Torr
3. Ti: 200W RF, 200nm, @11nm/min
4. Pt: 80W DC, 200nm @11nm/min

Platinum Topcoat:

1. Base Pressure: 5×10^{-5} Torr
2. Operating Pressure: 5×10^{-3} Torr
3. Pt: 80W DC 100nm @11nm/min

C. PECVD:

Oxford PlasmaPro 100 PECVD

Silicon Oxide Deposition:

1. Pressure: 1000mTorr
2. Temp: 350°C
3. Power RF Fwd: 20W
4. SCCM: N₂O/At5%SiH₄: 710/170
5. Dep Rate: 82nm/min

Silicon Nitride Deposition:

1. Pressure: 1000mTorr
2. Temp: 350°C
3. Power RF/LF Fwd: 20/20W
4. SCCM: NH₃/At5%SiH₄: 30/400
5. Dep Rate: 29nm/min

D. Plasma Etching:

Oxford ICP PlasmaPro 380 RIE

Silicon Nitride Etch:

6. Pressure: 10mTorr

7. Temp: 15°C
8. Power Fwd/ICP: 50/2000W
9. SCCM: SF₆: 45
10. Etch Rate: 120nm/min

Silicon Dioxide Etch:

1. Pressure: 7mTorr
2. Temp: 15°C
3. Power Fwd/ICP: 200/2100W
4. SCCM: C₄F₈/O₂: 37.5/5
5. Etch Rate: 330nm/min

Silicon Etch:

1. Pressure: 10mTorr
2. Temp: 15°C
3. Power Fwd/ICP: 50/1500W
4. SCCM: SF₆/C₄F₈: 26/35
5. Etch Rate: 300nm/min

E. Evaporation:

CHA Industries Mk40 Electron Beam Evaporator

Titanium and Platinum E-Beam Evaporation:

1. Base Pressure: 2×10^{-6} Torr
2. Ti: 10nm, 0.5Å/s
3. Pt: 100nm 1Å/s